National Library
of Canada

Bibliothèque nationale
du Canada

Canadian Theses Service

Services des thèses canadiennes

Ottawa, Canada
K1A 0N4

CANADIAN THESES

THÈSES CANADIENNES

NOTICE

The quality of this microfiche is heavily dependent upon the quality of the original thesis submitted for microfilming. Every effort has been made to ensure the highest quality of reproduction possible.

If pages are missing, contact the university which granted the degree.

Some pages may have indistinct print especially if the original pages were typed with a poor typewriter ribbon or if the university sent us an inferior photocopy.

Previously copyrighted materials (journal articles, published tests, etc.) are not filmed.

Reproduction in full or in part of this film is governed by the Canadian Copyright Act, R.S.C. 1970, c. C-30. Please read the authorization forms which accompany this thesis.

AVIS

La qualité de cette microfiche dépend grandement de la qualité de la thèse soumise au microfilmage. Nous avons tout fait pour assurer une qualité supérieure de reproduction.

S'il manque des pages, veuillez communiquer avec l'université qui a conféré le grade.

La qualité d'impression de certaines pages peut laisser à désirer, surtout si les pages originales ont été dactylographiées à l'aide d'un ruban usé ou si l'université nous a fait parvenir une photocopie de qualité inférieure.

Les documents qui font déjà l'objet d'un droit d'auteur (articles de revue, examens publiés, etc.) ne sont pas microfilmés.

La reproduction, même partielle, de ce microfilm est soumise à la Loi canadienne sur le droit d'auteur, SRC 1970, c. C-30. Veuillez prendre connaissance des formules d'autorisation qui accompagnent cette thèse.

THIS DISSERTATION
HAS BEEN MICROFILMED
EXACTLY AS RECEIVED

LA THÈSE A ÉTÉ
MICROFILMÉE TELLE QUE
NOUS L'AVONS REÇUE

NL 339 (r. 86/01)

Canada

National Library of Canada
Bibliothèque nationale du Canada

Ottawa, Canada
K1A 0N4

(16)

TC –

0-315-22882-2

CANADIAN THESES ON MICROFICHE SERVICE – SERVICE DES THÈSES CANADIENNES SUR MICROFICHE

PERMISION TO MICROFILM – AUTORISATION DE MICROFILMER

• Please print or type – Écrire en lettres moulées ou dactylographier

AUTHOR – AUTEUR

Full Name of Author – Nom complet de l'auteur: Yarub Sabri Al-Shiraida

Date of Birth – Date de naissance: July 1, 1950

Canadian Citizen – Citoyen canadien: ☐ Yes / Oui ☒ No / Non

Country of Birth – Lieu de naissance: Iraq

Permanent Address – Résidence fixe:
15335 - 121 St. Edmonton, Alta.
T5X 3B3

THESIS – THÈSE

Title of Thesis – Titre de la thèse: Ion Turbulence in a CO_2 Laser/Plasma Interaction

Degree for which thesis was presented / Grade pour lequel cette thèse fut présentée: Ph.D.

Year this degree conferred / Année d'obtention de ce grade: 1985

University – Université: University of Alberta

Name of Supervisor – Nom du directeur de thèse: A.A. Offenberger

AUTHORIZATION – AUTORISATION

Permission is hereby granted to the NATIONAL LIBRARY OF CANADA to **microfilm** this thesis and to **lend** or **sell copies of the film.**

The author reserves other publication rights, and neither the thesis nor extensive extracts from it may be printed or otherwise reproduced without the author's written permission.

L'autorisation est, par la présente, accordée à la BIBLIOTHÈQUE NATIONALE DU CANADA de **microfilmer** cette thèse et de **prêter** ou de **vendre des exemplaires du film.**

L'auteur se réserve les autres droits de publication; ni la thèse ni de longs extraits de celle-ci ne doivent être imprimés ou autrement reproduits sans l'autorisation écrite de l'auteur.

ATTACH FORM TO THESIS – VEUILLEZ JOINDRE CE FORMULAIRE À LA THÈSE

Signature: Al-Shiraida

Date: Aug. 22, 1985

NL-91 (r. 84/03)

Canada

THE UNIVERSITY OF ALBERTA

ION TURBULENCE IN A CO_2 LASER/PLASMA INTERACTION

by

©

YARUB S. AL-SHIRAIDA

A THESIS
SUBMITTED TO THE FACULTY OF GRADUATE STUDIES AND RESEARCH
IN PARTIAL FULFILMENT OF THE REQUIREMENTS FOR THE DEGREE
OF DOCTOR OF PHILOSOPHY

DEPARTMENT OF ELECTRICAL ENGINEERING

EDMONTON, ALBERTA

FALL 1985

THE UNIVERSITY OF ALBERTA

RELEASE FORM

NAME OF AUTHOR Yarub S. Al-Shiraida

TITLE OF THESIS Ion Turbulence in a CO_2 Laser/Plasma
Interaction

DEGREE FOR WHICH THESIS WAS PRESENTED Doctor of Philosophy

YEAR THIS DEGREE GRANTED Fall 1985

Permission is hereby granted to THE UNIVERSITY OF ALBERTA LIBRARY to reproduce single copies of this thesis and to lend or sell such copies for private, scholarly or scientific research purposes only.

The author reserves other publication rights, and neither the thesis nor extensive extracts from it may be printed or otherwise reproduced without the author's written permission.

(Signed) Al-Shiraida

PERMANENT ADDRESS:

15335 - 121 Street,
Edmonton, Alberta
T5X 3B3

DATED August 18, 1985

THE UNIVERSITY OF ALBERTA

FACULTY OF GRADUATE STUDIES AND RESEARCH

The undersigned certify that they have read, and recommend to the Faculty of Graduate Studies and Research, for acceptance, a thesis entitled ION TURBULENCE IN A CO_2 LASER/PLASMA INTERACTION submitted by Yarub S. Al-Shiraida in partial fulfilment of the requirements for the degree of Doctor of Philosophy in Electrical Engineering.

A Offenberger
Supervisor

Peter R Smy

C R James

[illegible] Rao

H Baldis
External Examiner

Date July 18, 1985

DEDICATION

To my parents for their love and support.

ABSTRACT

A comprehensive investigation of the ion turbulence generated in a laser/plasma interaction experiment has been carried out using the high power laser facility available in the Department of Electrical Engineering at the University of Alberta. A CO_2 laser beam with focused intensity of $5 \times 10^{12} w/cm^2$ was used to ionize and heat an oxygen gas target, thereby producing plasma with an electron temperature, T_e, of ~ 100 eV and density $n \lesssim 10^{19} cm^{-3}$.

Ruby laser Thomson scattering was utilized to study the non-equilibrium ion fluctuations generated in the plasma by the presence of a strong electromagnetic wave. Considerable enhancement of these ion fluctuations over the thermal level was observed for two plasma regimes (short and long density scale length regimes). In the long scale length regime the magnitude of density fluctuations along with temporal and spectral features of the scattered ruby light indicate that ion turbulence can account for the anomalous absorption of CO_2 laser energy observed in earlier experiments. In the long scale length regime a general measurement of the ion fluctuation wavenumber spectrum induced in the plane of the CO_2 laser electric field and high speed streak measurements of the Thomson scattered light were performed for the first time and are presented in this thesis.

The source of ion turbulence in laser produced plasmas is discussed, placing particular emphasis on ion waves generated by parametric instabilities. The general plasma dispersion equation is

solved numerically for the ion response in the presence of a strong pump to establish instability growth rates. Such analyses indicate that the Brillouin instability, filamentation and off-resonance parametric decay (PD) and oscillating two stream (OTS) instabilities can be easily excited and are believed to be the main source for the observed enhanced ion fluctuations in our experiment. In particular, for fluctuations induced parallel to the electric field of the incident CO_2 laser pump wave, PD and OTS are potential sources of turbulence leading to anomalous absorption effects observed experimentally.

ACKNOWLEDGEMENT

I would like to express my sincere gratitude to my supervisor, Dr. A.A. Offenberger, for his excellent guidance, ideas, encouragement and financial support which made this work possible. I feel very fortunate to have been able to work with Dr. Offenberger.

I would like to extend particular thanks to Dr. W. Rozmus who provided many important discussions and comments on the whole thesis in general and the second chapter in particular. Without his invaluable ideas this chapter would not have been accomplished.

Ideas and advices of Dr. A. Ng during the early stage of this work as well as his comments on the first draft of the thesis are greatly appreciated. Discussion and ideas of Dr. R. Fedosejevs and Dr. D. McKen are also acknowledged.

I am very grateful to my sincere friend Dr. F. Soliman for spending much of his valuable time in reading through the thesis. His friendship and encouragement are greatly acknowledged. In addition, I am extremely grateful to Mrs. Soliman for offering her tremendous effort in the preparing and typing of the thesis.

This work would not have been possible without the technical assistance of the machine shop staff, in particular H. Gans, K. Doerrbecker and G. Soligo, and the optics technologist, B. Arnold. I am also grateful to D. Way-Nee and M. Billing for their technical assistance and advice.

I must also thank my fellow graduate students, R. Giles, W. Tighe, S. Au, M. Abdel-Halim, D. Simeoni and G. Philip for their friendship and co-operation.

Finally, I would like to extend my sincere thanks and appreciation to my wife, children and parents for their patience, understanding and prayer.

TABLE OF CONTENTS

PAGE

CHAPTER 1 INTRODUCTION 1

CHAPTER 2 ION TURBULENCE IN LASER PLASMA INTERACTIONS 7

2.1 Ion Wave Instability 7

2.2 Ion Waves Induced by Parametric Processes 11

2.2.1 Introduction 11

2.2.2 Numerical solutions of the Drake dispersion relation. 14

2.2.3 Off-resonance oscillating two steam and parametric decay instabilities. 20

2.2.4 Saturation of ion waves. 28

2.3 Absorption Due to Ion Turbulence 34

CHAPTER 3 EXPERIMENTAL METHODS AND TECHNIQUES 40

3.1 Introduction 40

3.2 Laser Plasma Experiment 40

3.2.1 Carbon dioxide laser. 40

3.2.2 Gas jet and target chamber. 44

3.3 Measurements of Plasma Parameters 50

3.3.1 Infrared (IR) radiation detection. 50

3.3.2 Electron temperature (T_e). 52

3.3.3 Electron density (n) measurement. 54

3.4 Thomson Scattering Experiment 62

3.4.1 Outline of the experiment. 62

3.4.2 Scattering arrangements. 70

PAGE

CHAPTER 4 EXPERIMENTAL RESULTS AND DISCUSSION 79

4.1 Introduction 79

4.2 Ion Turbulence and Absorption 88

4.2.1 Laser light absorption in CO_2 laser plasma interaction. 88

4.2.2 Scattering parameters. 92

4.2.3 Temporal measurements of ion fluctuations. 93

4.2.4 Spectral measurements. 95

4.2.5 Ion fluctuation level. 104

4.3 Results of Case II 108

4.3.1 Introductory remarks. 108

4.3.2 $S(k)$ measurements. 109

4.3.3 Streak measurements. 112

4.3.4 Sources of ion turbulence. 114

CHAPTER 5 SUMMARY AND CONCLUSION 128

APPENDIX A SOLUTION OF THE DISPERSION EQUATION 136

APPENDIX B MODELING OF THE CO_2 LASER 147

B.1 Gas Kinetics of the CO_2-N_2-He Mixture 147

B.2 Numerical Solution of the Rate Equations 151

APPENDIX C ABEL INVERSION 155

APPENDIX D NUMERICAL SOLUTION OF THE $S(\omega,\overline{k})$ FUNCTION 160

APPENDIX E DECONVOLUTION OF SPECTRA 163

REFERENCES 131

LIST OF TABLES

TABLE		PAGE
3.1	Features of the CO_2 TEA Laser	42
3.2	Features of the Q-switched Ruby Laser	60

LIST OF FIGURES

PAGE

FIGURE

2.1 Electron and ion distribution functions in the presence of an electron heat flux $\bar{Q}$. 8

2.2 Growth rate and real frequency of ion wave for Brillouin scattering and filamentation versus k/k_D for oxygen plasma (z=6) with $T_i = T_e$ = 100 eV, n/n_c = 0.5 and v_0/v_e = 2. 15

2.3 Growth rate and real frequency of ion wave for Brillouin scattering and filamentation versus k/k_D for oxygen plasma (z=6) with $T_i = T_e$ = 100 eV, n/n_c = 0.75 and v_0/v_e = 2. 16

2.4 Growth rate and real frequency of ion wave for Brillouin scattering and filamentation versus k/k_D for oxygen plasma (z=6) with $T_i = T_e$ = 100 eV, n/n_c = 0.25 and v_0/v_e = 2. 17

2.5 Growth rate and real frequency of ion wave for Brillouin scattering and filamentation versus k/k_D for oxygen plasma (z=6) with $T_i = T_e$ = 100 eV, n/n_c = 0.5 and v_0/v_e = 1. 18

2.6 Growth rate of ion wave instability (PD off-resonance) versus k/k_D for oxygen plasma (z=6) with $T_i = T_e$ = 100 eV, n/n_c = 0.5 and v_0/v_e = 1. 22

2.7 Growth rate of ion wave instability (PD off-resonance) versus k/k_D for oxygen plasma (z=6) with $T_i = T_e$ = 100 eV, n/n_c = 0.6 and v_0/v_e = 1. 23

2.8 Growth rate of ion wave instability (PD and OTS off-resonance) versus k/k_D for oxygen plasma (z=6) with $T_i = T_e$ = 100 eV, n/n_c = 0.7 and v_0/v_e = 1. 24

FIGURE PAGE

2.9 Growth rate of ion wave instability (PD and OTS off-resonance) versus k/k_D for oxygen plasma (z=6) with $T_i = T_e = 100$ eV, $n/n_c = 0.8$ and $v_0/v_e = 1$. 25

2.10 Growth rate of ion wave instability (PD and OTS off-resonance) versus k/k_D for oxygen plasma (z=6) with $T_i = T_e = 100$ eV, $n/n_c = 0.9$ and $v_0/v_e = 1$. 26

2.11 Thresholds of the most easily excited modes of PD and OTS off-resonance instabilities as a function of density for oxygen plasma (z=6) with $T_i = T_e = 100$ eV. 27

2.12 Growth rate of PD and OTS off-resonance instabilities versus k/k_D for oxygen plasma (z=6) with $T_i = T_e = 100$ eV, $n/n_c = 0.8$ and $v_0/v_e = 1$, 2, 3 and 4. 29

2.13 The growth rate (of PD and OTS off-resonance) and the real frequency (of PD off-resonance) of the most easily excited ion modes in an oxygen plasma (z=6) with $T_i = T_e = 100$ eV, $n/n_c = 0.7$ and $v_0/v_e = 1$. 30

2.14 Real frequency of the ion waves of PD off-resonance instability as a function of k/k_D for an oxygen plasma (z=6) with $T_i = T_e = 100$ eV, $v_0/v_e = 1$ and $n/n_c = 0.5$, 0.6, 0.7, 0.8 and 0.9. 31

2.15 The growth rate (of PD and OTS off-resonance) and the ratio γ/ω (of PD off-resonance) of the most easily excited ion modes versus T_i/T_e for an oxygen plasma (z=6) with $v_0/v_e = 1$ and $n/n_c = 0.7$. 33

2.16 Im $\frac{1}{\varepsilon(\overline{k}_i,\omega_0)}$ averaged over a uniform spectrum of ion fluctuations as a function of density for a Maxwellian oxygen plasma with $T_i = T_e = 100$ eV. 38

3.1 Gain switched CO_2 laser output. 43

3.2 Output of the CO_2 laser model. 45

FIGURE PAGE

3.3 Schematic diagram of the CO_2 laser plasma interaction experiment and various diagnostics. 46

3.4 Gas target design. 48

3.5 Firing sequences of the CO_2 laser. 49

3.6 Normalized x-ray intensity as a function of aluminum foil thickness. The circles are experimental data from the CO_2 laser plasma experiment. 53

3.7 a) X-ray detector b) Typical x-ray signal for $T_e << 1$ keV. 55

3.8 Optical system for Fresnel's bimirror interferometer. 58

3.9 Subnanosecond switching of the ruby laser. 61

3.10 Typical fringe pattern with 25 micron fringe spacing. 63

3.11 Schematic diagram of the scattering geometry. 65

3.12 Thomson scattering experiment for $S(\omega,\overline{k})$ measurements. 73

3.13 Thomson scattering experiment for streak measurements. 75

3.14 Thomson scattering experiment for $S(\overline{k})$ measurements. 77

4.1 General behaviour of the CO_2 laser plasma interaction: a) Transmitted CO_2 laser signal, b) SBS signal, c) Thomson scattering signal. 80

4.2 Schematic diagram of the Thomson scattering experiment; a) Wave vectors at the incident, scattered and ion waves, b) Intersection of the CO_2 laser beam, ruby laser beam and the collected light. 83

4.3 Unfolded interferogram of the plasma density of Case I at ∿ 3 ns after the start of SBS. 85

4.4 Variation of the peak density (r=0) with the axial distance Z at ∿ 3 ns after the start of SBS for Case I. 86

4.5 Unfolded interferogram of the plasma density of Case I at ∿ 10 ns after the start of SBS. 87

FIGURE PAGE

4.6 Unfolded interferogram of the plasma density of Case II at ∿ 3 ns after the start of SBS. 89

4.7 Variation of the peak density (r=0) with the axial distance Z at ∿ 3 ns after the start of SBS for Case II. 90

4.8 Calculated ruby Thomson scattering spectrum for a thermal oxygen plasma with $T_i = T_e = 100$ eV, $n = 0.8\ n_c$, $z = 6$ and $\theta = 60^\circ$ showing the ion component (solid) and the electron component (dashed). 96

4.9 Calculated ruby Thomson scattering spectrum for a thermal oxygen plasma with $T_i = T_e = 100$ eV, $n = 0.4\ n_c$, $z = 6$ and $\theta = 60^\circ$ showing the ion component (solid) and the electron component (dashed). 97

4.10 Variation of the ion component (of the ruby Thomson scattering spectrum) with ion temperature and degree of ionization for a thermal oxygen plasma with $T_e = 100$ eV, $n = 0.8\ n_c$ and $\theta = 60^\circ$. 99

4.11 Spectra of scattered ruby laser light for $\theta = 60^\circ$ showing a) and b) unshifted typical spectra (for scattering in the X-Y plane), c) shifted spectrum for scattering in the Z-Y plane. 100

4.12 Spectrum of the scattered ruby laser light for $\theta = 22^\circ$ in the X-Y plane. 102

4.13 Ion turbulence spectrum $S(k)$ as a function of $k\lambda_D$ assuming an average density $n = 0.8\ n_c$ and T_e = 100 eV (Case I). The Kadomtsev type spectrum is also shown (dashed). 107

4.14 Ion turbulence spectrum $S(k)$ as a function of $k\lambda_D$ assuming an average density $n = 0.7\ n_c$ at T_e = 100 eV (Case II). The error bars indicate the standard diviations for thirty shots at average focused CO_2 laser intensity of 5×10^{12}w/cm^2. 111

FIGURE PAGE

4.15 Schematic diagram of the Thomson scattering experiment to probe ion fluctuations induced by stimulated Brillouin backscattering. 113

4.16 Temporal behaviour of the Thomson scattered light (bottom) and the incident ruby light (top) in each plate showing different features: a) long lived fluctuations (∿ 3 ns), b) short lived fluctuations (250 ps) with no structure, c) ∿ 0.7 ns long fluctuations with fine structure. 115

4.17 Streak photograph of ∿ 1.2 ns duration enhanced scattering event from ion turbulence occupying ∿ 170 μm region. 117

4.18 Time evolution of the spatial distribution of turbulence for a 3 ns duration ($\theta = 16^\circ$ in the X-Y plane). 119

4.19 Time evolution of the spatial distribution of turbulence for a 0.8 ns duration ($\theta = 16^\circ$ in the X-Y plane). 120

4.20 Time evolution of the spatial distribution of turbulence showing a motion of the fluctuation region in the direction of the propagation of the CO_2 laser beam ($\theta = 16^\circ$ in the X-Y plane). 121

4.21 Numerical values of $S(k)$ versus k/k_D for oxygen plasma with $z = 6$ and $T_i = T_e = 100$ eV. Dashed curves correspond to $v_0/v_e = 0$. a) $v_0/v_e = 0.6$, $n/n_c = 0.6$, b) $v_0/v_e = 0.05$, $n/n_c = 0.8$. 125

A.1 Roots found using the bisection method. 137

B.2 Some of the low lying levels of the CO_2 and N_2 molecules. 148

C.1 Cross sectional view of a cylindrically symmetric plasma. 156

E.1 Effect of a finite slit on a spectrum. a) The spectrum as observed through a Gaussian slit of FWHM = 13 channels. b) The true spectrum. c) The recovery of the true spectrum from the observed one using the deconvolution technique. 166

CHAPTER 1

INTRODUCTION

A problem of crucial importance to laser fusion programs is how a laser light is absorbed by the plasma. It is believed that radiation can be absorbed in laser produced plasmas by different mechanisms depending on the laser parameters (intensity, wavelength and pulse duration) as well as the target material and configuration. These mechanisms may be classified into two types: (a) collisional absorbtion or inverse bremsstrahlung, (b) absorption due to collective effects in the plasma. In the inverse bremsstrahlung absorption (sometimes called classical absorption) an electron absorbs a photon as it moves from one free energy state to a more energetic state in the field of an ion. Absorption of the laser beam by a plasma will take place only in those regions were the density is lower than the critical density (at which the plasma frequency and the frequency of the incident radiation are the same). The absorbed fraction, A, calculated for the case of normal incidence of light on a plasma, the density of which varies linearly between $n = 0$ to a critical density n_c within a distance L, is given by |1|

$$A = 1 - \exp\left(- \frac{32}{15} \frac{L}{c} \nu_{ei}^{c}\right) ,$$

in which the electron-ion collisional frequency at the critical density may be written as

$$\nu_{ei}^{c} = 3 \times 10^{-6} z n_c \ln N T_e^{3/2} .$$

where $\ln \Lambda$ is the usual coulomb logarithm ($\ln \Lambda = 5 - 10$), z is the average ionic charge and T_e is the electron temperature in eV. According to the above equations classical absorption is more significant for high values of z, low temperature plasma and short wavelength laser light (large n_c). For long wavelength lasers, such as CO_2 , and plasmas at temperatures of interest to laser-fusion, inverse bremsstrahlung mechanism is of less significance. It should also be pointed out that the absorption due to this mechanism decreases with profile steepening of the plasma near the critical density [2]. In addition, nonlinear effects and the disturbance in the plasma distribution function induced at higher laser intensities greatly reduce its effect [2,3].

Collective absorption, on the other hand, takes place as a result of various physical processes in the plasma. The most important of these processes are resonance absorption and parametric instabilities of the plasma. Resonance absorption occurs when the laser light is obliquely incident on a non-uniform plasma with the electric field of the incident wave being polarized in the plane of incidence (P-polarization). In this way the electric field perpendicular to the plane of the target can tunnel through from the point of reflection to the critical density, thus exciting an electron plasma wave. This wave, being electrostatic, cannot propagate outward and the energy is ultimately dissipated as heat in the plasma. The actual amount of resonance absorption of P-polarized light will depend on the angle of incidence θ and the density scale length. Contrary to inverse bremsstrahlung, resonance absorption is more significant at high plasma temperatures (high laser intensities), longer laser wavelengths and shorter plasma scale lengths.

The second type of collective absorption is that associated with parametric instabilities. The most important of these instabilities are: the oscillating two-stream instability, OTS; the parametric decay instability, PD (both occurring near the critical density); and the two-plasmon decay occurring near $n_c/4$. In these instabilities, called absorptive instabilities (to be distinguished from the scattering instabilities like stimulated Brillouin and Raman instabilities), the pump wave decays into two electrostatic waves. The electron plasma wave, which is one of the products, continues to grow at the expense of the pump wave until it saturates by pump depletion or any other non-linear mechanism. These high frequency oscillations, in turn, accelerate and heat the electrons. The effective collision frequency ν^* or the so-called anomalous collisionality (defined as the rate of transferring wave energy to particles) can be estimated quantitatively according to the following energy balance scheme:

Pump wave ⟶ Electron plasma waves ⟶ Plasma particles .

At saturation the effective collision frequency for OTS and PD instabilities is given by |4|

$$\nu^* \simeq 4\gamma\left(\frac{\omega_{pe}}{\omega_0}\right)^2 = 4\gamma\,\frac{n}{n_c} \simeq 4\gamma$$

where γ is the growth rate of the instability, ω_0 is the laser light frequency and ω_{pe} and n are the electron plasma frequency and density respectively. The parametric instabilities are intrinsically non-linear processes and will not be induced below a threshold light intensity (unlike resonance absorption which may occur at any laser light intensity). The threshold values depend on density scale length, plasma temperature, laser wavelength and substantially increase with the inhomogeniety in the plasma. Although this mechanism is less important than resonance absorption it can still compete with inverse bremsstrahlung at higher intensities and longer laser wavelength. One of the disadvantages of this mechanism, as well as the resonance absorption mechanism, is the production of very energetic electrons which carry a portion of the absorbed energy, resulting in a very weak coupling with the background thermal plasma and thus an energy loss. In addition, these fast electrons may penetrate into and preheat the pellet core in laser-fusion pellets and raise its entropy which makes high compression difficult to achieve. For this reason, inverse bremsstrahlung is still considered the most favourable absorption mechanism in laser fusion.

It was pointed out by Dawson and Oberman |5| that absorption of radiation by a plasma can be enhanced in the presence of coherent short wavelength ion fluctuations. Recently |6-8| the interest in this subject has tremendously increased. Faehl and Kruer |6| derived an expression relating the damping rate of laser energy to the ion fluctuation level in a plasma (Chapter 2). According to this relation the damping rate could be of the same order or even higher than the classical collision frequency, ν_{ei} , in the presence of high level coherent ion fluctuations. Manheimer and Colombant |9| continued their investigations in an attempt to correlate experimental results on absorption of high intensity laser light by plasma with previous theories. These investigations clearly indicated that there is a discrepancy between theory and experiment. This led them to believe that ion turbulence is a possible candidate as an absorption mechanism that causes such a discrepancy.

The actual source and magnitude of ion fluctuations in laser plasma interactions remains somewhat hypothetical. Manheimer and his colleagues |7-10| have postulated that the turbulence is produced by heat flow driven ion acoustic instabilities. Faehl and Kruer |6| and Forslund |11| have suggested that ion-ion streaming instabilities could create a high level of ion fluctuations. Moreover, there is only limited theoretical knowledge of the ion fluctuation spectra which may be generated by instabilities other than the current driven ion wave instability.

On the experimental side, ion turbulence has been measured directly in several CO_2 laser plasma experiments. Gray and Kilkenny |12| investigated the possible influence of ion turbulence in reducing thermal conductivity in a Z-pinch plasma heated by moderate intensity CO_2 laser radiation. Walsh and Baldis |13| and Giles and Offenberger |14| studied ion fluctuations associated with Brillouin scattering in high intensity CO_2 laser plasma interactions. Although substantial enhancements in the fluctuation level over thermal noise have been seen in these experiments no general measurement of the fluctuation level and spectrum has been made for high intensity laser produced plasmas and, in particular, for wave vector $\overline{k}$ parallel to the direction of the incident electric field which is of importance for absorption (Chapter 2).

The previous survey clearly indicated that ion turbulence, if understood may provide an explanation for some of the physical processes that occur during laser/plasma interactions. This being the case, it appeared to us that ion turbulence in general, and its role in absorption of laser radiation in laser heated plasma experiments in particular, are two interesting topics for research. The main objective of this research is two fold; one is to study the cause as well as the characteristics of ion fluctuations in high intensity laser produced plasmas; the other is to confirm the existence of ion turbulence as an absorption mechanism using temporal and spectral analysis.

In Chapter 2 a summary of ion wave instabilities, placing particular emphasis on parametric instabilities is first given. Numerical solutions of the plasma dispersion equation in the presence of a high intensity laser beam is carried out and the results are given. Curves illustrating the dependence of the growth rate of ion wave related parametric instabilities on different plasma parameters are presented. Finally the theory of light absorption by an ion turbulence mechanism is also highlighted.

Chapter 3 provides a detailed description of the laser plasma experimental setup and the various diagnostic techniques utilized for studying ion fluctuations.

In Chapter 4 the results of our experimental investigations as well as interpretation of these results are given. The measurements of the plasma parameters and basic characteristics are first presented. Results of temporal and spectral measurements and turbulence levels of the ion fluctuations (from Thomson scattering measurements) are provided with an estimation of the laser light being absorbed via ion turbulence. Measurements of the spectral form factor $S(k)$ and streak camera measurements of the ion fluctuations are also presented. Finally a discussion of the possible source of ion fluctuations in the present experiment is given.

Conclusions and suggestions for further investigations are given in Chapter 5.

CHAPTER 2

ION TURBULENCE IN LASER PLASMA INTERACTIONS

2.1 Ion Wave Instability

It has been shown theoretically that ion turbulence may explain the nonclassical plasma behaviour in absorption of laser radiation |1-3|, heat transport of absorbed energy |4,5| and generation of energetic particles in laser plasma interactions |6|. The magnitude of these effects depends significantly on both turbulence level and spectrum. Although high fluctuation levels ($\delta n/n \sim 0.1$) have been measured in laser plasma experiments |7-12|, the actual source of ion turbulence is not well understood. Manheimer and his colleagues |4| suggested that ion turbulence may be produced by heat flow driven acoustic instabilities; a mechanism that is similar to the well known current driven ion acoustic instability mechanism |13|. For high electron to ion temperature ratio ($zT_e/T_i \gg 1$), ion acoustic waves become weakly Landau damped and their phase velocity becomes much greater than the ion thermal velocity v_i . This means that any distortion in the electron distribution function will easily drive these ion waves unstable. Such a distortion may occur in the presence of a strong electromagnetic wave. Figure 2.1 shows the electron and ion distribution functions for $T_e/T_i \gg 1$ in which the laser beam is propagating in the negative x direction. The laser energy flux absorbed by electrons will be converted into thermal energy flux (heat flux) $\overline{Q}$. As can be seen in the figure the electron distribution is distorted for $v_x < 0$ because

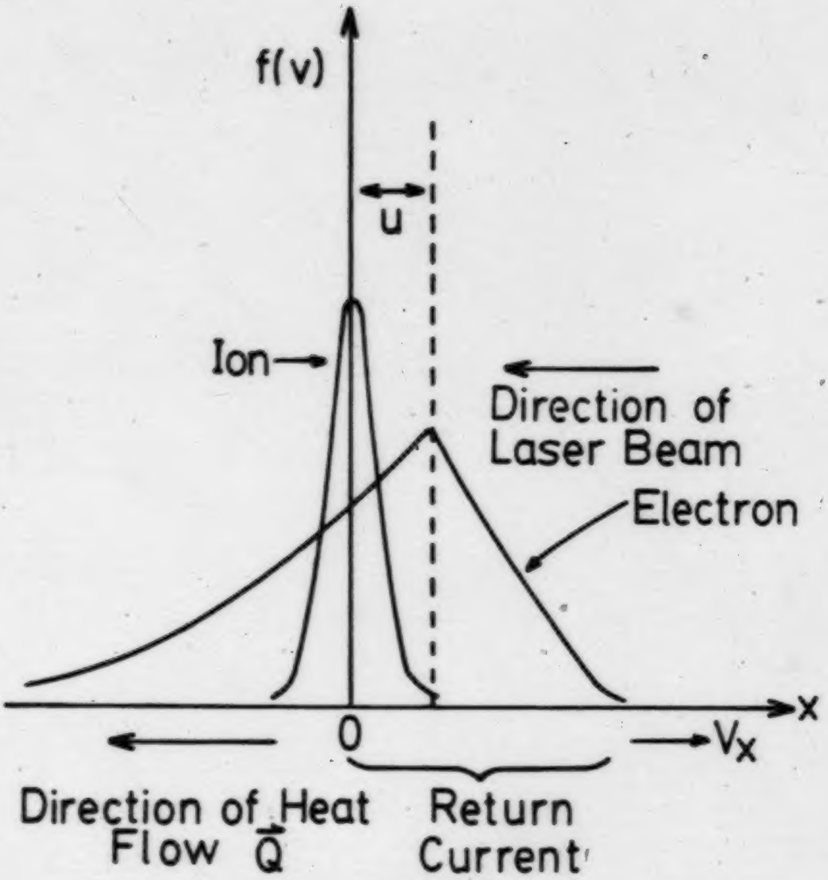
f(v)
u
Ion
Direction of
Laser Beam
Electron
x
0
V_x
Direction of Heat
Flow $\vec{Q}$
Return
Current

Fig. 2.1 Electron and ion distribution functions in the presence of an electron heat flux $\vec{Q}$.

heat is being carried in the $-X$ direction by electrons with speed $|u_x| > v_e$. In order to maintain charge neutrality a return current of colder electrons must flow in a direction opposite to the direction of the laser light propagation (i.e., $+X$ direction). Thus the electron distribution function for $v_x > 0$ is skewed to the right. In addition, the peak of the electron distribution function occurs at $v_x = +u$ rather than at $v_x = 0$. The ion waves will therefore be driven unstable if $u > c_s$ and $c_s > v_i$ (i.e., $zT_e > T_i$), where c_s is the sound speed and v_i is the ion thermal speed. The wave vector $\overline{k}$ of the ion acoustic waves is antiparallel to the heat flux $\overline{Q}$. It is worth mentioning that the fluctuation level associated with this mechanism was found to saturate by ion trapping in the range $0.1 < \delta n/n < 0.2$ within a time of order $t \sim 10^3/\omega_{pe}$ ($\sim$ 5 p sec for CO_2 laser), where ω_{pe} is the electron plasma frequency |6|. Moreover, these fluctuations seem to be nearly uniformly distributed within a wide cone of an angle $\theta \sim 50 - 60^\circ$ around the direction of the return current. It is therefore expected that no significant fluctuations will be generated in the directions perpendicular to the direction of the laser beam.

Another mechanism that could be responsible for generating ion turbulence in laser produced plasmas is the ion-ion streaming instability proposed by Faehl and Kruer |3|. Such an instability occurs when different ion species are available (ions of different masses or different ionization degrees). The physics of this mechanism is easy to understand. When a plasma is heated a large ambipolar potential develops to prevent the hot electrons from leaving the target. Ions are then accelerated by this potential and also by the large ponderomative potentials near the critical density. At low densities, where ion-ion collisions are weak, separation of the different ion species takes place (due to the different expansion velocities). A simple estimate shows that this separation is obtained when $\nu_{ii} < v_i/L$, where ν_{ii} is the ion-ion collision frequency, v_i is the ion speed which the ions obtain by falling through the large potential, and L is the distance over which it occurs. Results of a simple simulation code |3| and others of a two-dimensional simulation code |14| show that a fluctuation level of ∿ 10% could be reached in a plasma of two ion species such as H and D_2 . In real plasmas this instability may be severely restricted, especially in the hot region where almost all the ions are ionized to the highest possible level and ions of identical masses are used.

The third possible mechanism for generating ion turbulence in laser produced plasmas is the ion wave instability induced by different parametric processes. It is well established that ion waves can be excited via stimulated Brillouin instability in the underdense plasma and the e-i decay and oscillating two stream instabilities near the critical density. Because of the small value of k for ion fluctuations induced by the Brillouin instability, the enhancement in classical absorption is of no importance. This will be explained in a later section. On the other hand, very little attention has been paid to other parametric instabilities which can excite ion waves in underdense plasmas and, particularly, for $k\lambda_D \sim O(1)$ (where λ_D is the Debye length). In the next section the importance of parametric instabilities in generating ion turbulence will be studied in more detail.

2.2 Ion Waves Induced by Parametric Processes

2.2.1 Introduction.

Parametric processes refer to the nonlinear couplings of the electromagnetic wave with the natural wave modes in the plasma. These modes subsequently grow at the expense of the driving electromagnetic field which is called the pump. Such processes can only occur when the pump intensity exceeds a threshold value. To simply explain how the parametric instability takes place, assume the plasma is driven by a field (of a finite amplitude) which oscillates at a frequency ω_0 . If the plasma has an oscillating mode at a frequency ω (the initial amplitude of which may be as low as the noise level) which can couple to the pump at ω_0 then these two oscillations will beat together to produce sideband modes at frequencies $\omega_\pm = \omega_0 \pm \omega$. If the difference frequency ω_- happens to be another lightly damped mode of the plasma, it will beat with ω_0 at $\omega = \omega_0 - \omega_-$ and $\omega' = \omega_0 + \omega_-$. Thus the mode at ω is enhanced and will beat more strongly with ω_0 to give a stronger ω_- mode. It should be born in mind that for conservation of both energy and momentum (assuming the pump as a quantum being converted into quanta of other modes) it is required that the following conditions must be satisfied

$$\omega_0 = \omega + \omega_- \ , \ \bar{k}_0 = \bar{k} + \bar{k}_- \ . \qquad (2.1)$$

In laser plasma interactions the laser light acts as a transverse electromagnetic wave pump (t). The excited mode in this case may be another transverse mode (t'), a longitudinal Langmuir electron wave (ℓ) or an ion sound wave (s). The possible mode couplings are:

$t \rightarrow \ell + s$ "Parametric" Instability

$t \rightarrow t' + s$ Stimulated Brillouin Scattering

$t \rightarrow t' + \ell$ Stimulated Raman Scattering

$t \rightarrow \ell + \ell$ Two Plasmon Instability .

In parametric and two-plasmon instabilities laser light energy can be absorbed efficiently under certain conditions. On the other hand, in stimulated Raman and Brillouin scattering part of the laser energy will be lost in the form of sideband electromagnetic waves (t'). The loss is more pronounced in Brillouin scattering simply because the ion wave mode involved in this process takes up only a small fraction of the laser energy.

Since we are merely concerned with parametric processes which can excite low frequency ion modes, it will be assumed that the high frequency electromagnetic pump ($\bar{k}_0$,ω_0) decays into a low frequency ion mode ($\bar{k}$,ω) and two high frequency waves ($\bar{k}_\pm = \bar{k} \pm \bar{k}_0$, $\omega_\pm = \omega \pm \omega_0$). The sideband modes ($\bar{k}_\pm$,$\omega_\pm$), which are generated through a nonlinear coupling between the low frequency perturbation ($\bar{k}$,ω) and the pump wave, will interact in turn with the pump wave and therefore create a ponderomotive force which reacts back with the ($\bar{k}$,ω) mode. According to Drake, *et al.* |15|, the ponderomotive force is given by

$$\bar{F}_p = \frac{e^2}{m\omega_0^2} (\bar{E}_{0+} \cdot \bar{E}_- + \bar{E}_{0-} \cdot \bar{E}_+) , \qquad (2.2)$$

where $\bar{E}_{0\pm} = \bar{E}_0(\pm\omega_0 , \pm\bar{k}_0)$ refer to the components of the pump electric field and $\bar{E}_\pm$ refer to the sideband waves' electric field.

The derivation of the generalized dispersion relation is based on the insertion of Eqn.(2.2) into the Maxwell-Vlasov equations of the plasma |16,17|. This dispersion relation for $(\omega_0/\omega_{pe}) \gg 1$ and $k\lambda_0 \ll 1$ is given by

$$\frac{1}{\chi_e(\bar{k},\omega)} + \frac{1}{\chi_i(\bar{k},\omega)+1} = k^2\left(\frac{|\bar{k}_- \times \bar{v}_0|^2}{k_-^2 D_-} - \frac{(\bar{k}_- \cdot \bar{v}_0)^2}{k_-^2\omega_-^2\varepsilon_-}\right.$$

$$\left. + \frac{|\bar{k}_+ \times \bar{v}_0|^2}{k_+^2 D_+} - \frac{(\bar{k}_+ \cdot \bar{v}_0)^2}{k_+^2\omega_+^2\varepsilon_+}\right), \tag{2.3}$$

where χ_e and χ_i are the usual electron and ion susceptibilities defined for a Maxwellian plasma by

$$\chi_{e,i}(\bar{k},\omega) = \frac{T_e}{T_{e,i}} \frac{1}{k^2\lambda_D^2} \left|1 + \frac{\omega}{kv_{e,i}} Z\left(\frac{\omega}{kv_{e,i}}\right)\right|,$$

$$Z(y) = \frac{1}{\sqrt{\pi}} \int_{-\infty}^{\infty} \frac{dx \exp(-x^2)}{x-y} , \tag{2.4}$$

where $v_{e,i}$ are electron and ion thermal speeds, λ_D is the Debye length, $v_0 = eE_0/m\omega_0$, $\varepsilon_\pm = 1 - \frac{\omega_{pe}^2}{\omega_\pm^2}$ and $D_\pm = c^2k^2 \pm 2\bar{k}\cdot\bar{k}_0c^2 \mp 2\omega_0\omega - \omega^2$.

The $\bar{k} \times \bar{v}_0$ terms in Eqn. (2.3) arise from the electromagnetic components of the sideband modes and the $\bar{k}_0 \cdot \bar{v}_0$ terms from the electrostatic components. Inspection of Eqn. (2.3) reveals the following:

i) The $\bar{k}_0 \cdot \bar{v}_0$ terms will be predominant only near the critical plasma density region ($\varepsilon_\pm \simeq 0$ or $\omega_{pe} \simeq \omega_0$) which is of no interest in this study.

ii) For $D_\pm \simeq 0$, the permittivity $\varepsilon_\pm \neq 0$ and the $\bar{k}_0 \cdot \bar{v}_0$ terms (the electrostatic terms) in the equation are nonresonant and therefore negligible. In this case, the high frequency sidebands are predominantly electromagnetic and the problem is essentially that of stimulated scattering where the pump wave excites an electrostatic wave and an electromagnetic wave at a shifted frequency. If we limit ourselves to the case where the electrostatic mode is an ion mode ($\omega \ll \omega_0$) then $\omega_{\pm} \simeq \omega_0$ and $\bar{k}_{t} \cdot \bar{E}_0 \sim 0$ and Eqn. (2.3) can be reduced to the form

$$\varepsilon(\bar{k},\omega)D_{+}(\bar{k},\omega)D_{-}(\bar{k},\omega) = \frac{k^2 v_0^2}{4}\chi_e(\bar{k},\omega)|1+\chi_i(\bar{k},\omega)| \times$$

$$|D_{+}(\bar{k},\omega) + D_{-}(\bar{k},\omega)| \,, \qquad (2.5)$$

where ε is the plasma dielectric constant ($= 1+\chi_e+\chi_i$).

Equation (2.5) describes stimulated Brillouin scattering (SBS) and filamentation (a purely growing mode, i.e., Real $\omega = 0$, occurs when D_{+} and D_{-} are comparable).

2.2.1 Numerical solutions of the Drake dispersion relation.

The numerical technique used for the solution of the Drake dispersion relation as given by Eqn. (2.5) is discussed in Appendix A. Results showing the dependence of both the growth rate γ and the real frequency component ω_R (where $\omega_0 = \omega_R + i\gamma$) of the ion wave instability in an oxygen plasma ($z = 6$, $T_i = T_e = 100$ eV) on k/k_D, with n/n_c and v_0/v_e taken as parameters are given in Figs.2.2-2.5(where $k_D = 1/\lambda_D$). As shown in the figures results are plotted for three different angles θ, where θ is the angle between $\bar{k}$ and $\bar{E}_0$ (where $\theta = 0$, 45 and 90° correspond respectively to Brillouin backscattering, Brillouin side-scattering and filamentation).

According to Fig. 2.2 ($n/n_c = 0.5$, $v_0/v_e = 2$) for $\theta < 90°$ there are narrow regions of k/k_D where γ and ω_R are approximately of the same order and within which the maximum growth rates are located. For

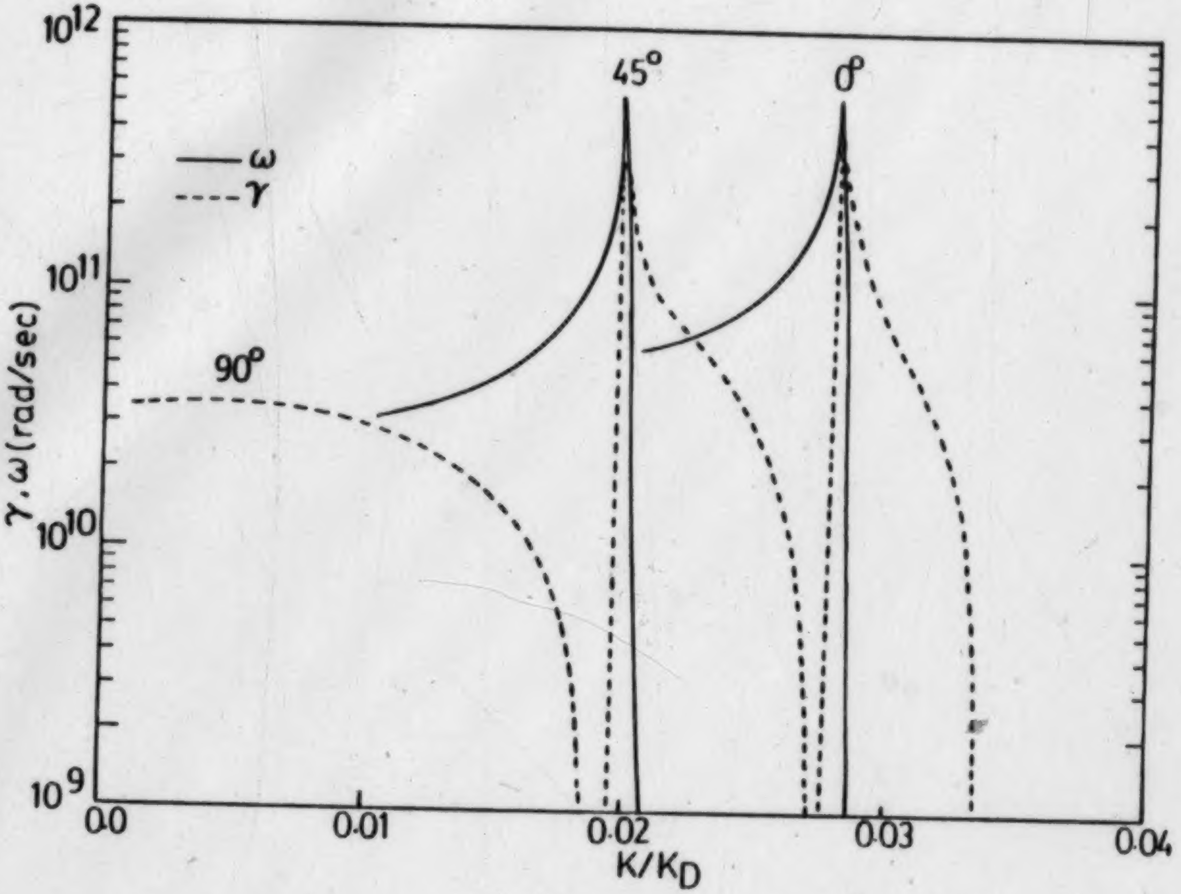

Fig. 2.2 Growth rate and real frequency of ion wave for Brillouin scattering and filamentation versus k/k_D for oxygen plasma (z=6) with $T_i = T_e$ = 100 eV, n/n_c = 0.5 and v_0/v_e = 2.

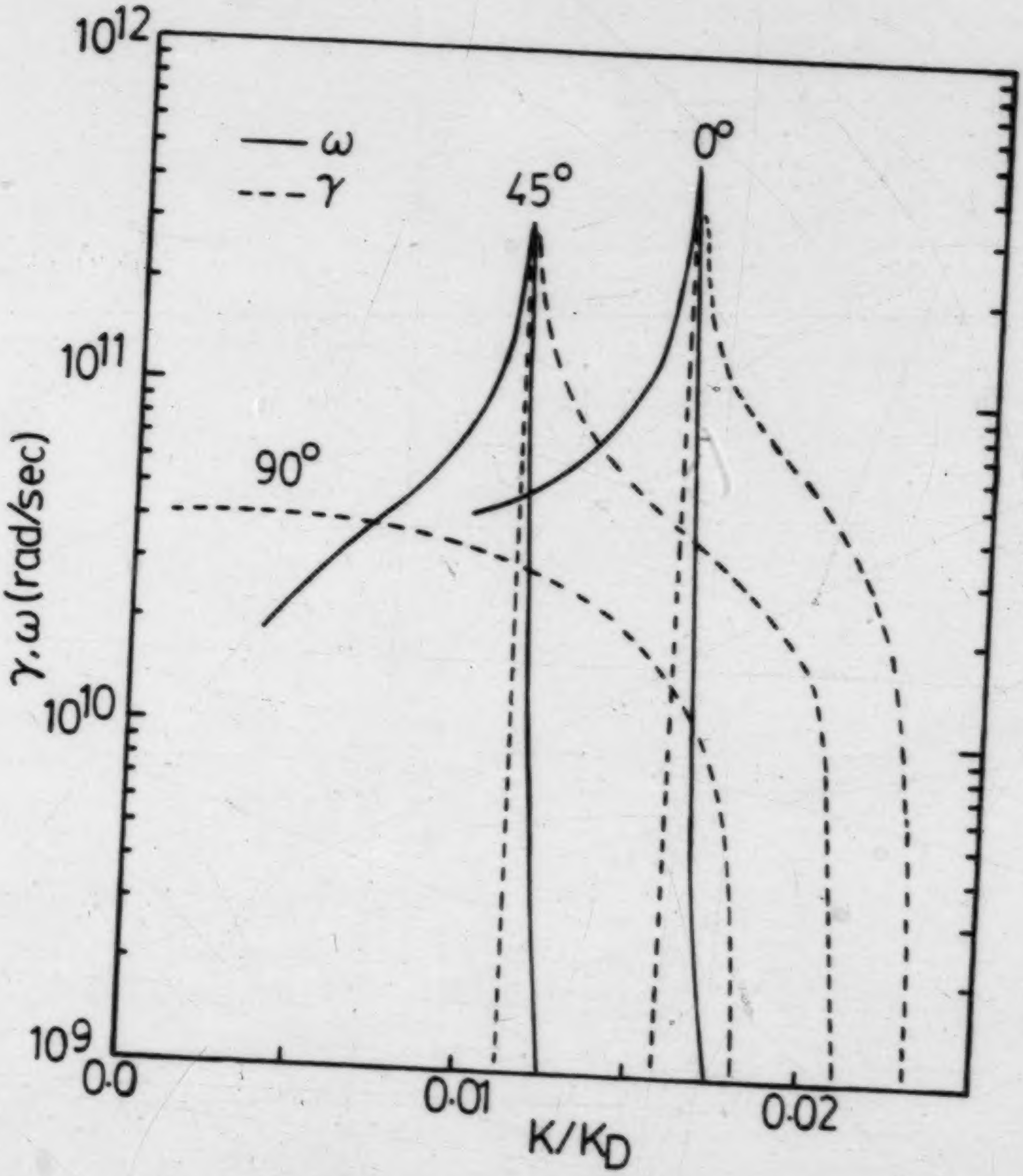

Fig. 2.3 Growth rate and real frequency of ion wave for Brillouin scattering and filamentation versus k/k_D for oxygen plasma (z=6) with $T_i = T_e$ = 100 eV, n/n_c = 0.75 and v_0/v_e = 2.

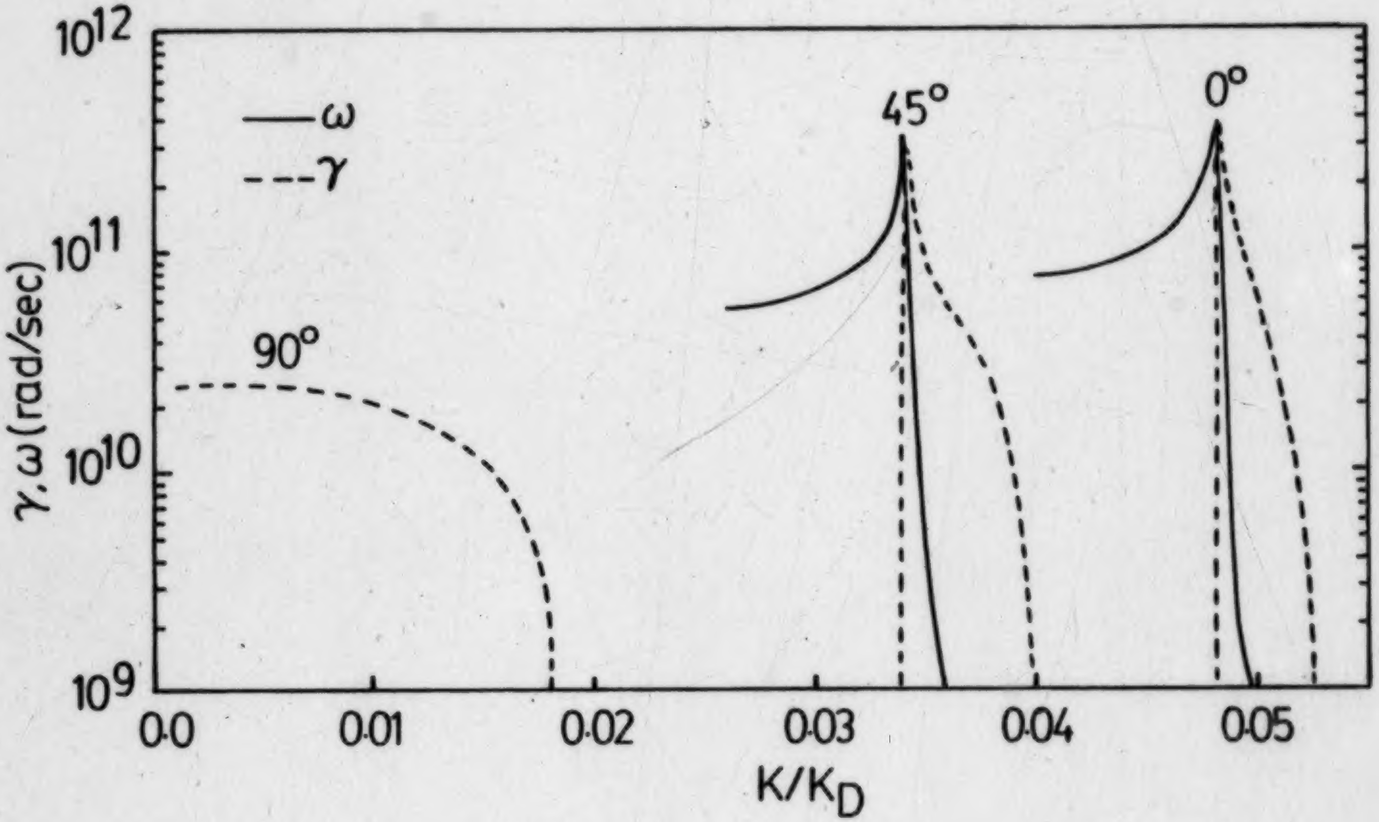

Fig. 2.4 Growth rate and real frequency of ion wave for Brillouin scattering and filamentation versus k/k_D for oxygen plasma (z=6) with $T_i = T_e$ = 100 eV, n/n_c = 0.25 and v_0/v_e = 2.

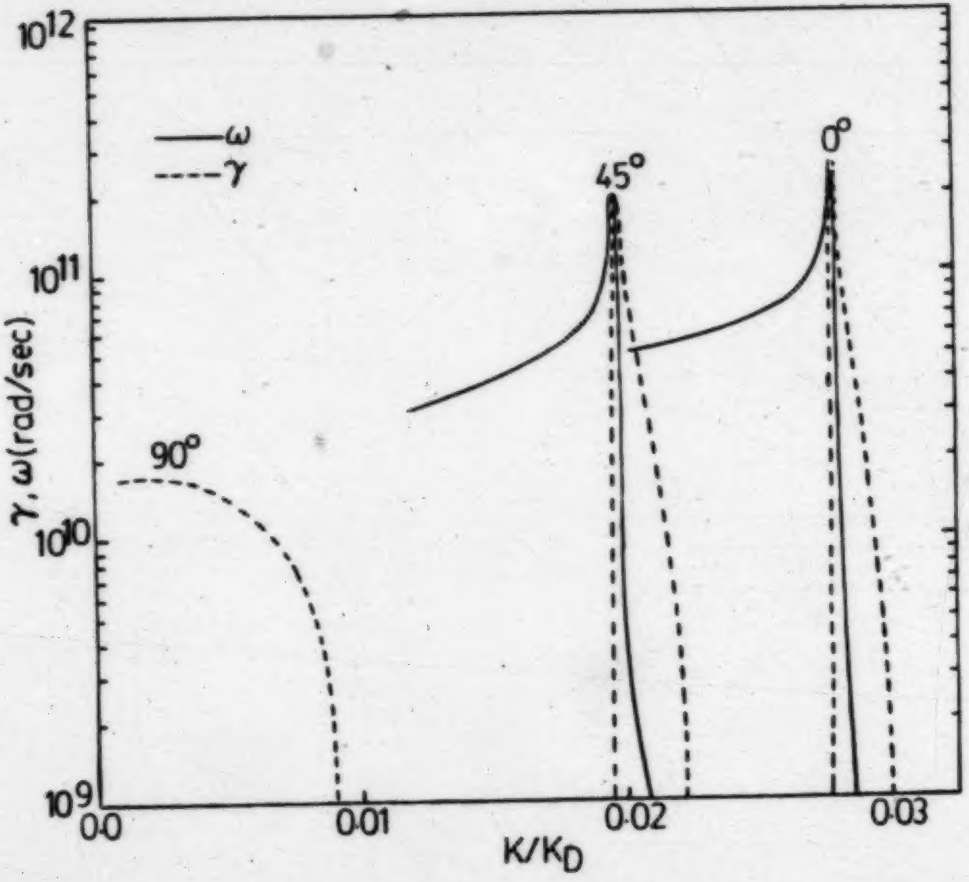

Fig. 2.5 Growth rate and real frequency of ion wave for Brillouin scattering and filamentation versus k/k_D for oxygen plasma (z=6) with $T_i = T_e$ = 100 eV, n/n_c = 0.5 and v_0/v_e = 1.

smaller values of k, i.e., to the left of these maxima γ drops to zero rapidly while ω_R decreases slowly before it approaches a constant value. To the right of the maxima ω_R drops faster than γ and the mode grows almost purely ($\omega_R = 0$) for certain ranges of k/k_D. The growth rate decreases slowly over an order of magnitude range as θ increases from 0° to 90°. The instability covers a small range of k/k_D (~ 0 to 0.03) whereas the filamentation alone covers the range $0 \lesssim k/k_D \lesssim 0.02$. This range of k/k_D has no significant role in enhancing absorption.

Figures 2.3 and 2.4 are similar to Fig. 2.2 but with $n/n_c = 0.75$ and 0.25 respectively. It is clear from these figures that the k/k_D range of the ion fluctuations induced by SBS increases with density, while the k/k_D range of the ion fluctuations induced by filamentation stays constant. In addition, the growth rate of the most highly excited mode of Brillouin scattering remains fairly constant in the range $0.2 \leq n/n_c \leq 0.75$, while for filamentation the growth rate increases slowly with density.

Figure 2.5 is similar to Fig. 2.2 except v_0/v_e was reduced to 1. This figure shows, in addition to the reduction in the growth rate, shorter ranges of k/k_D for each individual angle with the most highly excited modes remaining at the same k/k_D.

It was also found from the solution of Eqn. (2.5) that both the Brillouin scattering and filamentation were insensitive to the temperature ratio, at least in the range $0.25 \leq T_i/T_e \leq 4$. Furthermore, these instabilities have v_0/v_e thresholds of order 0.1 for the lowest threshold excited modes for $n/n_c = 0.5$. This threshold value is quite low and is equivalent to a CO_2 laser intensity of $\sim 2.4 \times 10^{10}$ W/cm^2.

As was pointed out earlier and noticed in Figs. 2.2 to 2.5, the above instabilities (SBS and filamentation) occur in the $k\lambda_D << 1$ region which is of no interest for absorption. However, these instabilities may be important in explaining the general ion fluctuation k-spectrum.

2.2.2 Off-resonance oscillating two stream and parametric decay instabilities.

Other parametric instabilities, which involve ion modes and may occur in the subcritical density region, are the oscillating two stream (OTS) and the parametric (electron-ion) decay (PD) off-resonance instabilities. In these instabilities, similar to the usual OTS and PD instabilities, the pump decays into ion wave (with $\omega_R = 0$ in the case of OTS) and electron wave. Unfortunately, for the parameters $\omega_{pe} \lesssim \omega_0$, $k\lambda_D \simeq 0(1)$ and a pump strength $v_0/v_e \simeq 0(1)$, the general dispersion relation of Drake *et al.* (2.3) is not valid. However, another approach to the problem of the instability induced by a strong pump field has been carried out by Silin |17| and Sanmartin |18|. Although the solution is limited to electrostatic sidebands, it is quite general for an arbitrary pump strength and a wide range of k/k_D. The general dispersion relation for a uniform high frequency field and a homogeneous and an unmagnetized plasma, derived from Vlasov-Poisson equations using Fourier and Laplace transformations, is given by |18|

$$1 + \chi_i^0 \left| \frac{J_0^2}{D_e^0} + \sum_{j=1}^{\infty} J_j^2 \left(\frac{1}{D_e^j} + \frac{1}{D_e^{-j}} \right) \right| = 0 \; , \qquad (2.6)$$

where $D_\alpha^j = 1 + \chi_\alpha^j$ (α stands for i or e),

$$\chi_\alpha^j = \frac{\omega_{p\alpha}^2}{k^2} \int \frac{\bar{k} \cdot (\partial F_{\alpha 0}/\partial \bar{u}_\alpha) d\bar{u}_\alpha}{\omega - j\omega_0 - \bar{k}_0 \cdot \bar{u}_\alpha} , \qquad (2.7)$$

where $F_{\alpha 0}$ is the zero order velocity distribution function of the particle α, $\omega_{p\alpha}^2 = (4\pi q_\alpha^2 n_\alpha / m_\alpha)$ and q_α and n_α are the α particle charge and density respectively. In Eqn. (2.7) the particle velocity $\bar{v}$ in the distribution function has been transformed to $\bar{u} = \bar{v} + \omega_0 \bar{\varepsilon}_\alpha \cos \omega_0 t$ with $\bar{\varepsilon}_\alpha = q_\alpha \bar{E}_0 / m_\alpha \omega_0^2$. The argument of the Bessel function J in (2.6) is $\bar{k} \cdot \bar{\varepsilon}_e = k \dfrac{eE_0}{m_e \omega_0^2} \cos \theta$ where θ is the angle defined before.

Equation (2.6) was previously analyzed by many authors |17-19| and its solution for unstable ion modes in the underdense plasma was obtained for certain conditions. For a more general case and for conditions of relevance to our experiment, Eqn. (2.6) has been solved numerically (Appendix A) for different values of the parameters (k/k_D), (n/n_c), (v_0/v_e), (T_i/T_e) and $\cos \theta$.

The solution of Eqn. (2.6) as illustrated in Figs. 2.6-2.10 indicates that an unstable ion wave can be excited for $n/n_c \gtrsim 0.5$ and $k/k_D \lesssim 0.5$. These figures also reveal the existence of two types of ion waves, the off-resonance PD and OTS. As can be seen in these figures, at low densities $(0.5 \lesssim n/n_c < 0.7)$ only PD off-resonance can be excited. However, at $n/n_c \sim 0.7$ the OTS off-resonance starts to take place and then dominates at higher densities (Fig. 2.10). The thresholds of the most easily excited modes of these instabilities vary between $v_0/v_e \sim 0.02$ to ~ 1.1, depending on the density region (Fig. 2.11). These thresholds are considered low and could be easily achieved in our experiment. Figure 2.11 also shows that the off-resonance PD instability has a lower threshold than the OTS instability.

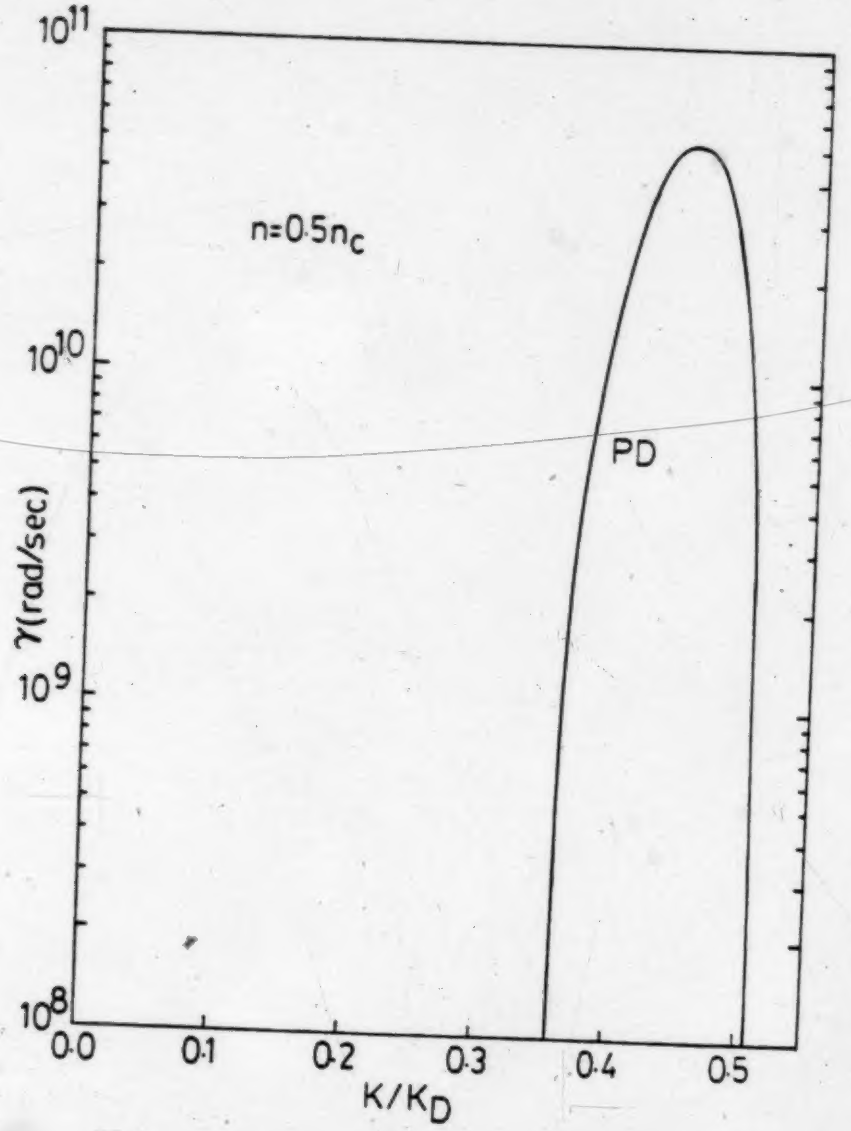

Fig. 2.6 Growth rate of ion wave instability (PD off-resonance) versus k/k_D for oxygen plasma (z=6) with $T_i = T_e$ = 100 eV, n/n_c = 0.5 and v_0/v_e = 1.

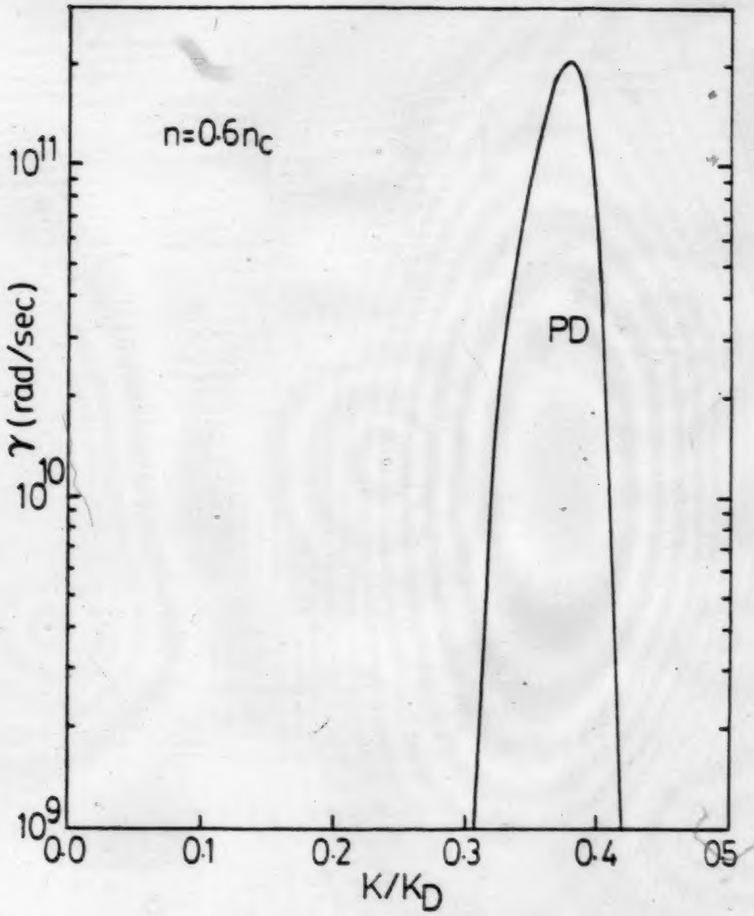

Fig. 2.7 Growth rate of ion wave instability (PD off-resonance) versus k/k_D for oxygen plasma (z=6) with $T_i = T_e$ = 100 eV, n/n_c = 0.6 and v_0/v_e = 1.

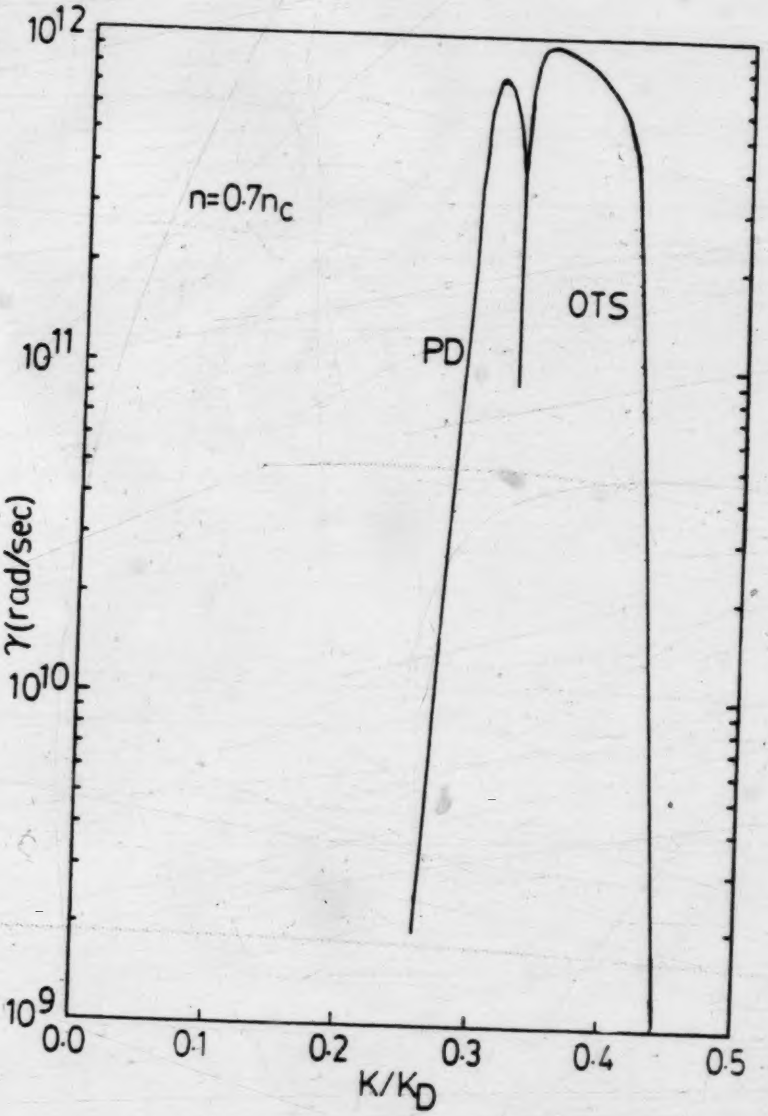

Fig. 2.8 Growth rate of ion wave instability (PD and OTS off-resonance) versus k/k_D for oxygen plasma (z=6) with $T_i = T_e = 100$ eV, $n/n_c = 0.7$ and $v_0/v_e = 1$.

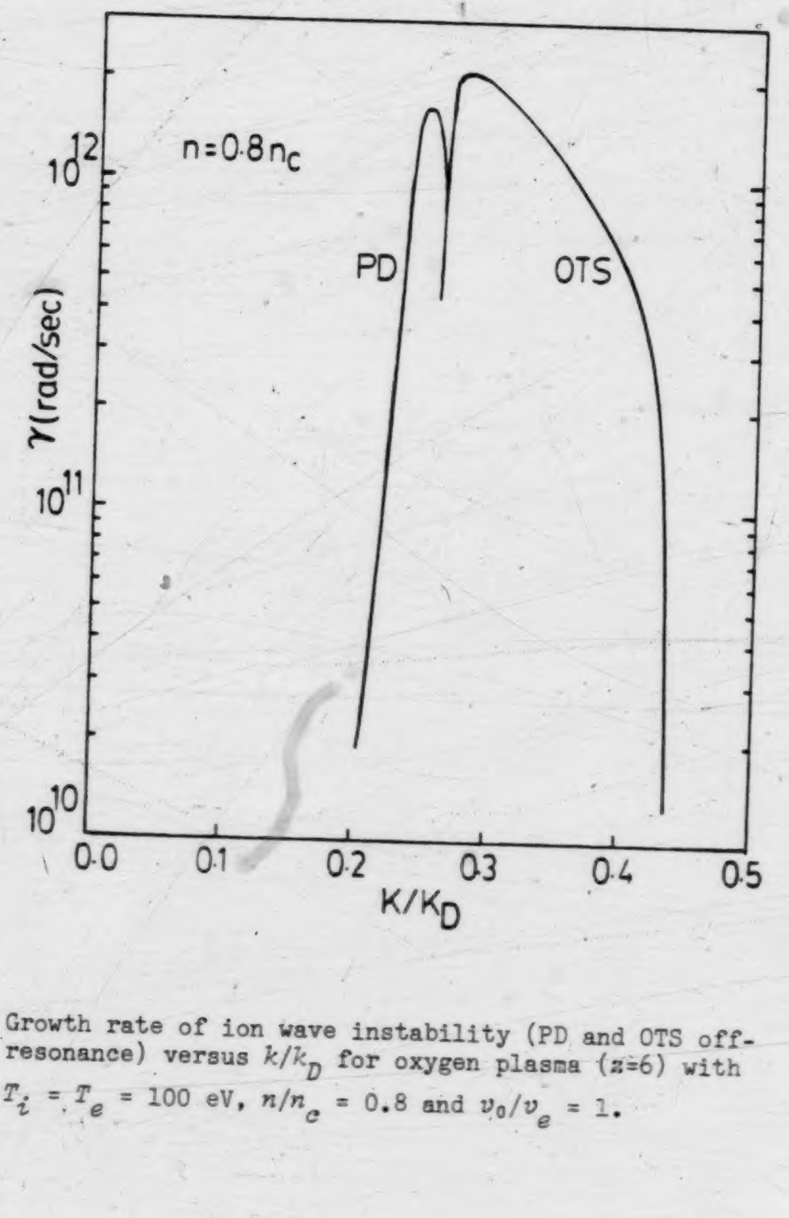

Fig. 2.9 Growth rate of ion wave instability (PD and OTS off-resonance) versus k/k_D for oxygen plasma (z=6) with $T_i = T_e$ = 100 eV, n/n_c = 0.8 and v_0/v_e = 1.

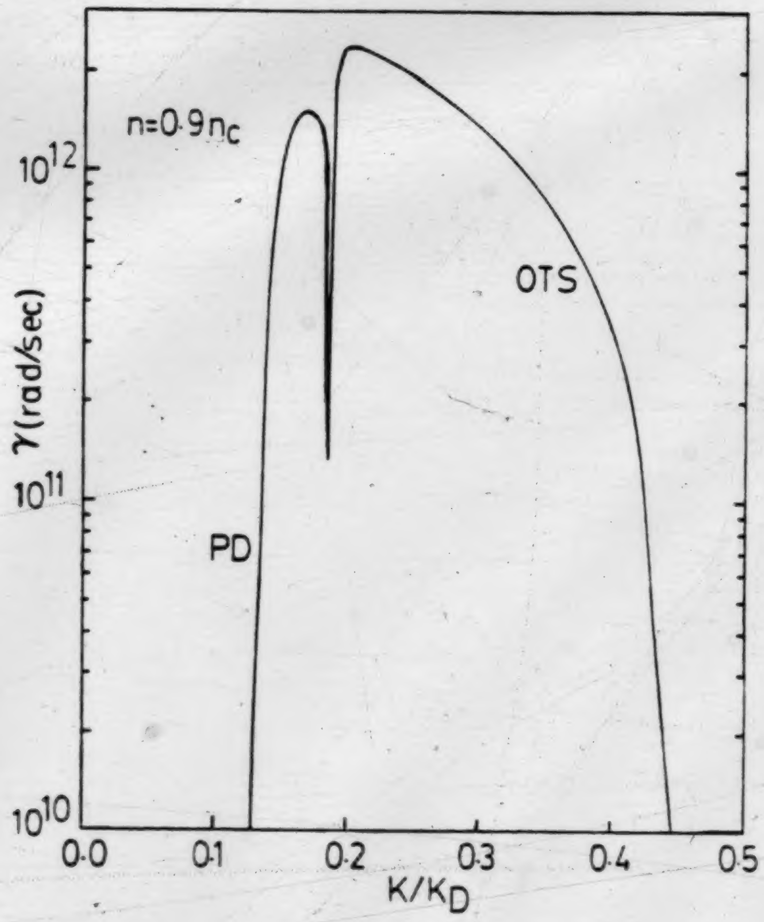

Fig. 2.10 Growth rate of ion wave instability (PD and OTS off-resonance) versus k/k_D for oxygen plasma (z=6) with $T_i = T_e$ = 100 eV, n/n_c = 0.9 and v_0/v_e = 1.

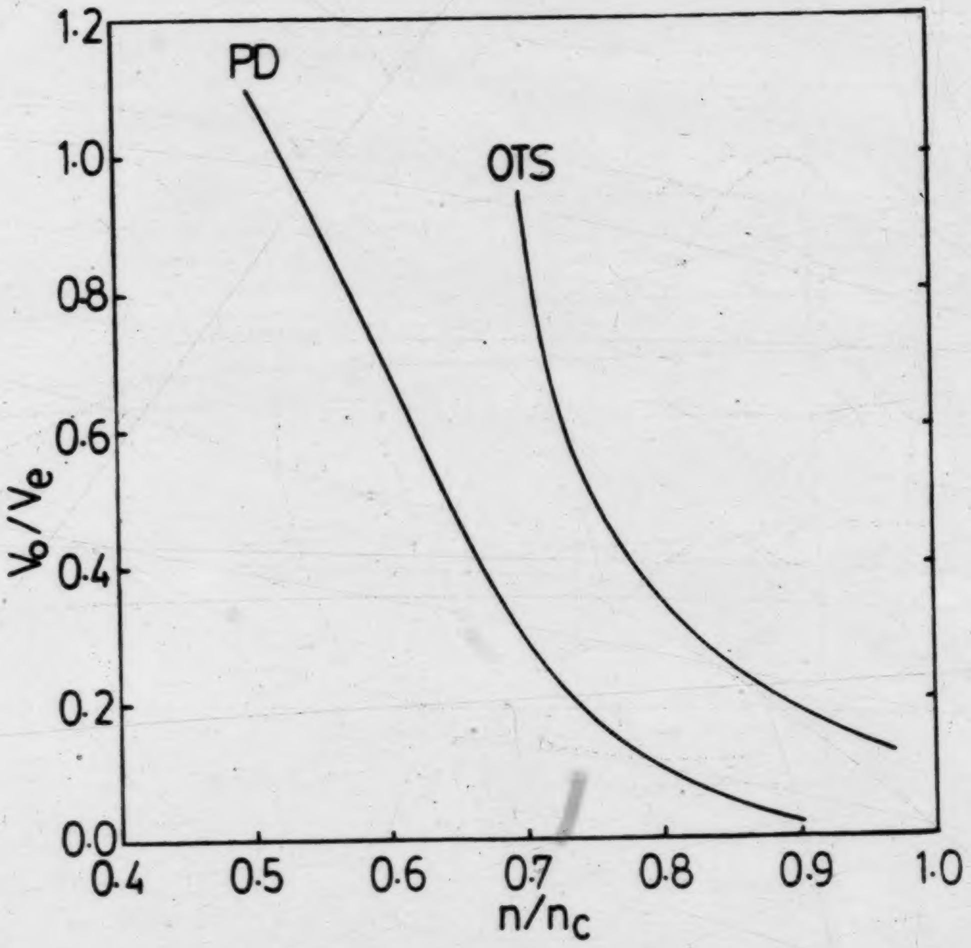

Fig. 2.11 Thresholds of the most easily excited modes of PD and OTS off-resonance instabilities as a function of density for oxygen plasma (z=6) with $T_i = T_e$ = 100 eV.

The range of k for which these instabilities can be excited varies with the pump strength v_0/v_e as indicated in Fig. 2.12 for $n/n_c = 0.8$. The growth rates of the PD and OTS off-resonance as well as the frequency of the ion acoustic mode (in the PD) as a function of the angle θ are shown in Fig. 2.13. Similar dependence is expected with respect to v_0/v_e since both $\cos\theta$ and v_0/v_e enter Eqn. (2.6) through the argument of the Bessel function only. The angular frequency of the ion waves generated from the PD instability varies quite significantly with k/k_D (Fig. 2.14). The peak of the frequency occurs very close to the most unstable k mode.

It is clear from Figs. 2.6 to 2.10 that the growth rates of the PD and OTS off-resonance instabilities are quite high for $v_0/v_e \sim 0(1)$, particularly for densities close to n_c , which makes one wonder about the possible mechanisms for saturating these instabilities. However, before discussing possible saturation mechanisms, it should be emphasized here that the above discussion is only valid for homogeneous plasmas. Inhomogeneity of the plasma could severely increase the thresholds and reduce the growth rates.

2.2.3 Saturation of ion waves.

Numerical simulations and theory indicate that the ion wave instability may be stabilized by ion trapping |20-22|. According to this nonlinear mechanism an ion will be trapped in the electrostatic potential ϕ of the ion wave as the wave grows and stabilization only occurs when a large number of ions are trapped. The ion trapping velocity v_{tr} is given (assuming a waterbag distribution function for the ions) by |23|

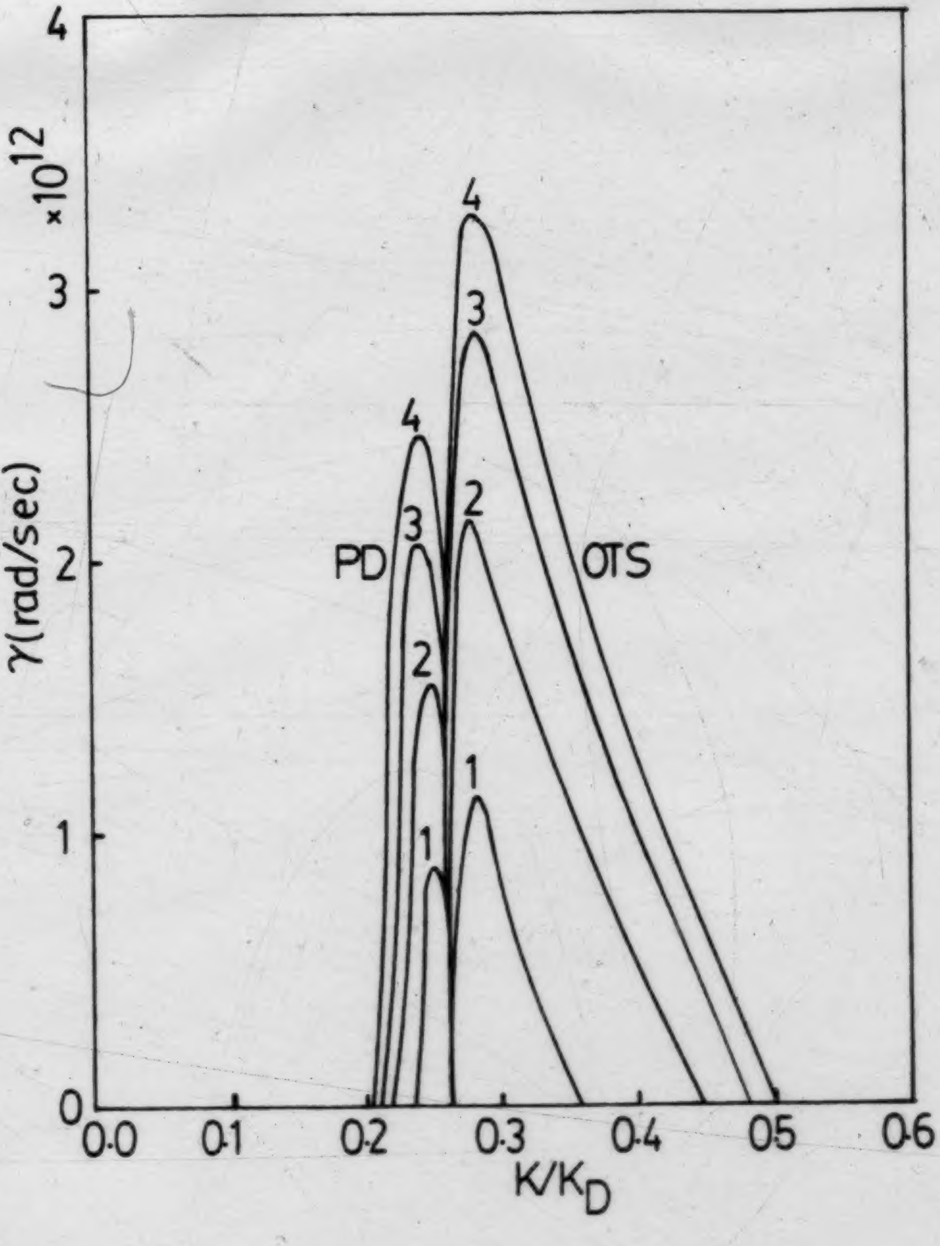

Fig. 2.12 Growth rate of PD and OTS off-resonance instabilities versus k/k_D for oxygen plasma (z=6) with $T_i = T_e$ = 100 eV, n/n_c = 0.8 and v_0/v_e = 1, 2, 3 and 4.

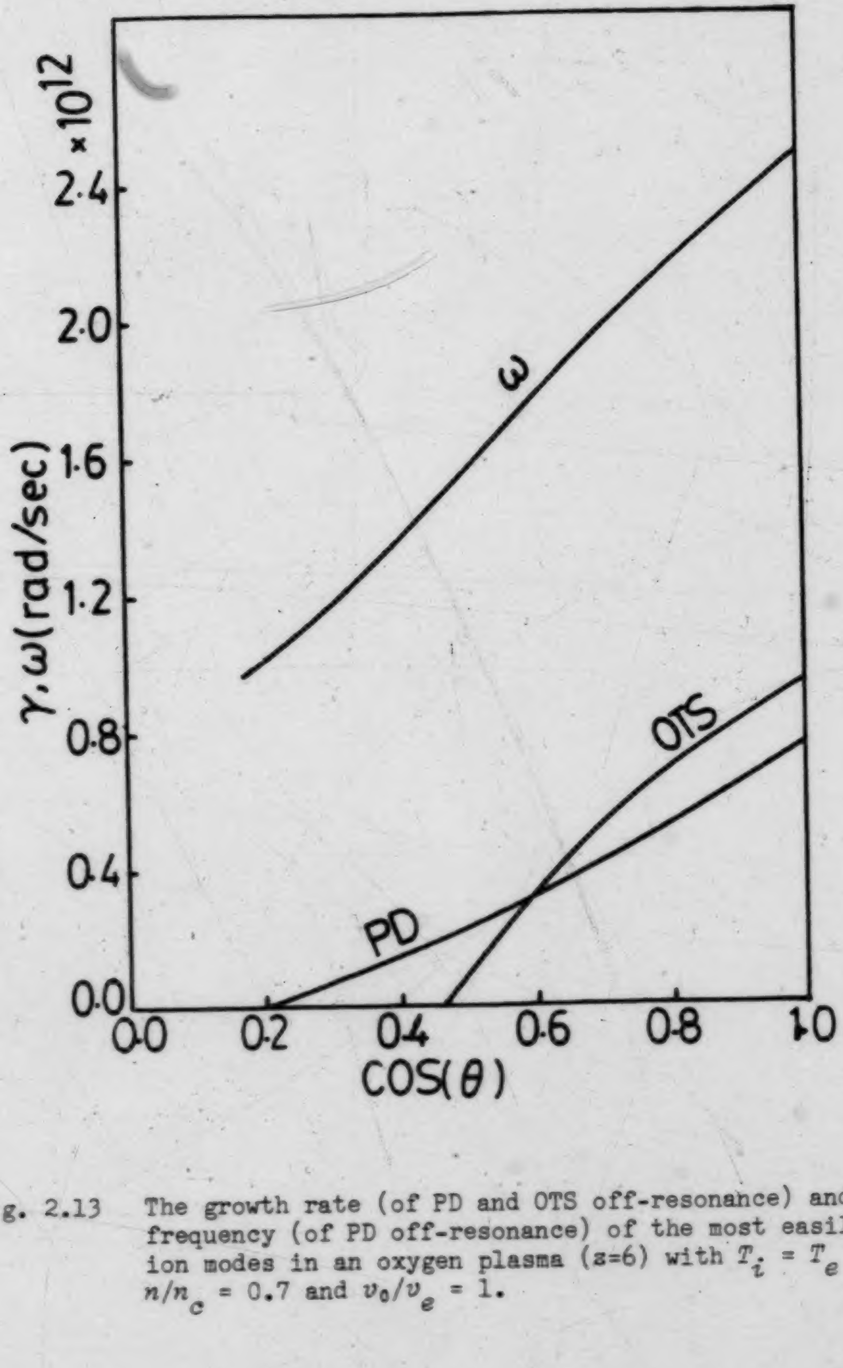

Fig. 2.13 The growth rate (of PD and OTS off-resonance) and the real frequency (of PD off-resonance) of the most easily excited ion modes in an oxygen plasma (z=6) with $T_i = T_e$ = 100 eV, n/n_c = 0.7 and v_0/v_e = 1.

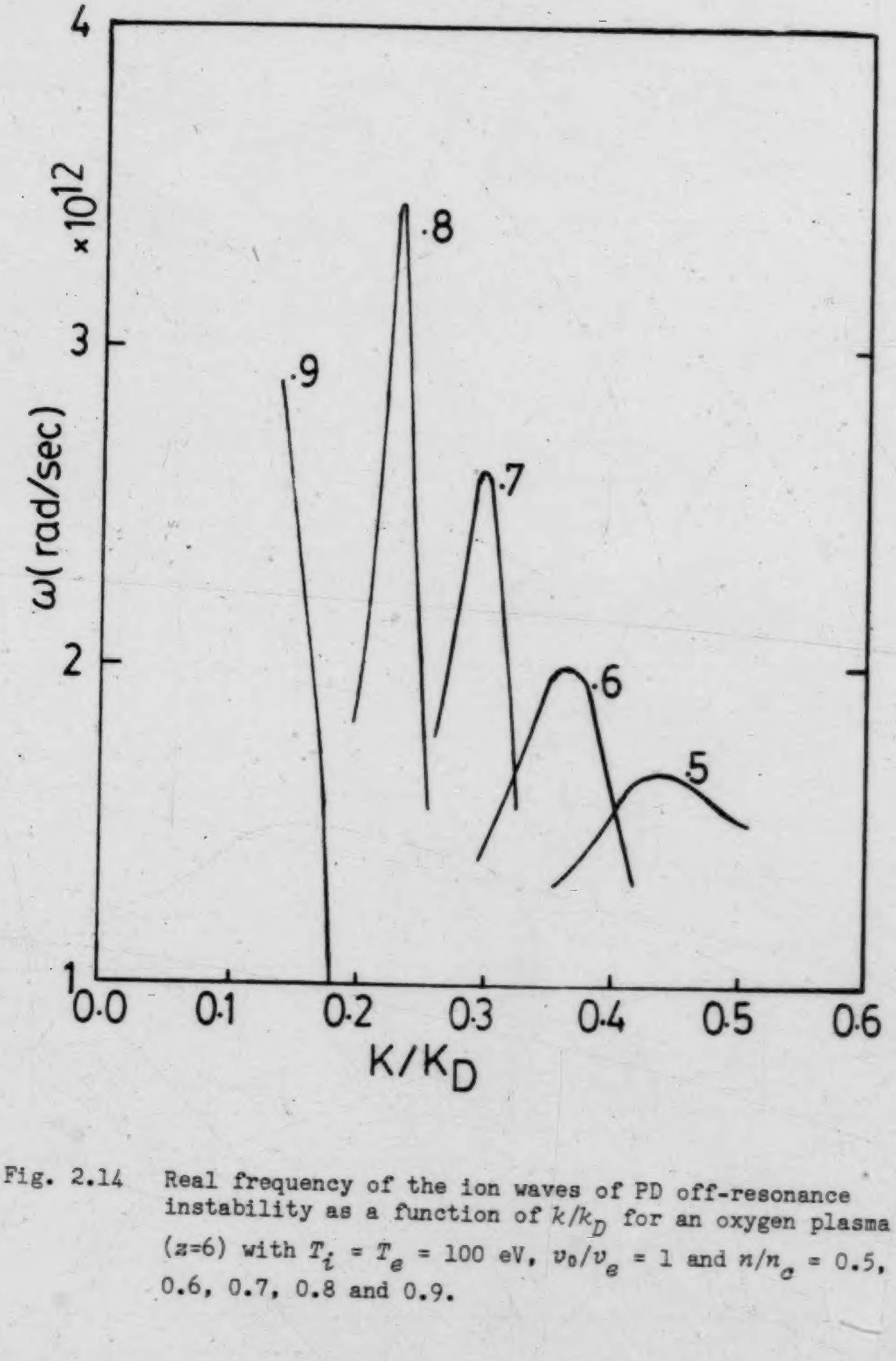

Fig. 2.14 Real frequency of the ion waves of PD off-resonance instability as a function of k/k_D for an oxygen plasma (z=6) with $T_i = T_e$ = 100 eV, v_0/v_e = 1 and n/n_c = 0.5, 0.6, 0.7, 0.8 and 0.9.

$$v_{tr} \simeq v_p - \sqrt{3}v_i \ , \tag{2.8}$$

where v_p is the phase velocity of the wave and v_i is the ion thermal velocity. The energy that the wave loses to the trapped particle is then given by

$$e\phi = \tfrac{1}{2}\,Mv_{tr}^2 = \tfrac{1}{2}\,M|v_p - \sqrt{3}v_i|^2 \ . \tag{2.9}$$

Substituting for v_p (using the ion dispersion relation), v_i and $e\phi(\simeq T_e\delta n/n)$ Eqn. (2.9) takes the following form

$$\frac{\delta n}{n} \leq \tfrac{1}{2}\left|\left(\frac{z + T_i/T_e}{1 + k^2\lambda_D^2}\right)^{\frac{1}{2}} - (3T_i/T_e)^{\frac{1}{2}}\right|^2 \ . \tag{2.10}$$

Equation (2.10) sets the upper limit for the density fluctuation when saturation occurs. For $T_i = T_e$, $k\lambda_D = 0.5$ and $z = 6$ (for oxygen plasma), $\delta n/n \sim 0.2$.

Numerical simulations |21,22| show that saturation takes place in a very short time ($\omega_{pe}t \simeq 2200$) while ion heating is still occurring. For a plasma with $n = 0.5n_c$ (where $n_c = 10^{19}\text{cm}^{-3}$) the saturation time is only $\sim$ 20 ps.

Electron heating could be another mechanism for saturating the PD and OTS off-resonance instabilities. Although the temperature ratio T_i/T_e has a very limited effect on the growth rates of these instabilities as illustrated in Fig. 2.15, heating of electrons to high temperatures, on the other hand, will decrease v_0/v_e , possibly below the instability threshold.

The PD off-resonance may also be stabilized by harmonic generation where coupling of the form

$$\omega_1 \pm \omega_2 = \omega_3 \ , \ \overline{k}_1 \pm \overline{k}_2 = \overline{k}_3 \ ,$$

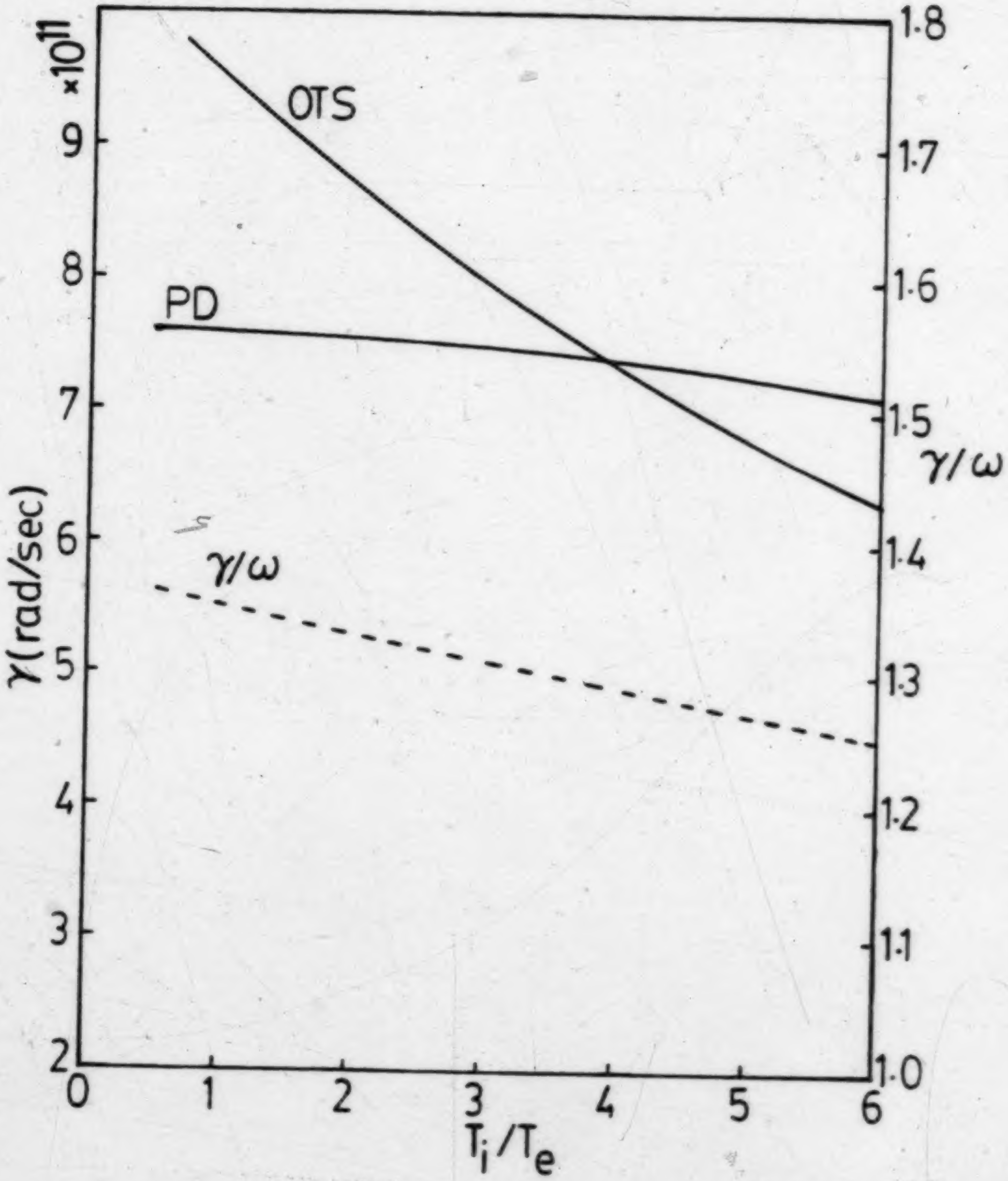

Fig. 2.15 The growth rate (of PD and OTS off-resonance) and the ratio γ/ω (of PD off-resonance) of the most easily excited ion modes versus T_i/T_e for an oxygen plasma (z=6) with v_0/v_e = 1 and n/n_c = 0.7.

may take place (where 1 and 2 refer to two unstable ion modes and 3 to a new ion wave). Saturation occurs in this process when the new wave is heavily damped. It should be pointed out that the general dispersion relation of Sanmartin predicts the existence of stable ion modes with a wide range of k and ω (Fig. 2.14). These stable modes could be a product of wave couplings described above. Recently, the importance of harmonic generation as a saturation mechanism for PD off-resonance instability has been confirmed theoretically and by simulation |24|.

2.3 Absorption Due to Ion Turbulence

Central to the problem of heating plasmas to **temperatures of interest for** fusion by means of lasers is the absorption of radiation. The simplest absorption process is that of inverse bremsstrahlung or resistive absorption due to electron-ion collisions (discussed in Chapter 1). For the case of a linear density profile of scale length L and $n \leq n_c$ the absorbed fraction of light is given by |25|

$$A = 1 - \exp\left| - \frac{32}{15}(\nu_{ei}^{c}\, L/c) \right| , \qquad (2.11)$$

where ν_{ei}^{c} is the electron-ion collision frequency at critical density. Equation (2.11) indicates that in order to have strong absorption, a short wavelength laser is preferred (simply because $\nu_{ei}^{c} \propto n_c \propto 1/\lambda^2$) and the plasma conditions must be such that both L and ν_{ei}^{c} are sufficiently large. The latter assumption, however, means low temperature plasmas are needed (since ν_{ei}^{c} varies with $T_e^{-3/2}$). It is therefore expected that the inverse bremsstrahlung absorption is very inefficient in hot plasmas where a high temperature is required for fusion. The situation is even worse when a long wavelength laser is used, such as the CO_2 laser.

In addition to inverse bremsstrahlung absorption, light can also be absorbed via wave-particle interactions. Such a process may occur when high intensity radiation excites plasma waves, which, in turn, transfer their energy to the particles by damping. In this case Eqn. (2.11) will be approximately valid but with ν_{ei}^{c} replaced by the effective damping rate of the effective collision frequency ν_{eff}. An example of this process, which is of relevence to us and will be discussed here, is the absorption due to ion turbulence.

The effect of ion turbulence on absorption was first discussed by Dawson and Oberman |26| and subsequently by Faehl and Kruer |3|. It is necessary, in order to understand absorption via ion turbulence, to briefly review the theory that was given by Faehl and Kruer |3|.

A simple interpretation can be obtained by considering the pump field of the form $E_0 \cos w_0 t$ propagating in a plasma whose density is

$$n = n_0 + \Sigma\, \delta n_{ki} \cos \overline{k}_i \cdot \overline{x} \,. \qquad (2.12)$$

As the electrons oscillate with velocity $\overline{v} = \dfrac{e\overline{E}_0 \sin w_0 t}{m w_0}$ between low and high density regions a source term of high frequency density fluctuations $n_s(\overline{x},t)$ is produced

$$n_s(\overline{x},t) = n(\overline{x}+\overline{r}_0) - n(\overline{x}) = \overline{r}_0 \cdot \nabla n \,, \qquad (2.13)$$

where $\overline{r}_0 = \dfrac{e\overline{E}_0 \cos w_0 t}{m w_0^2}$. The self-consistent field resulting from this source term is given by Poissons' equation whose Fourier transform is

$$i\varepsilon(\overline{k}\cdot w)\overline{k} \cdot \overline{E}(\overline{k},w) = -4\pi e n_s(\overline{k},w) \,, \qquad (2.14)$$

where $\varepsilon(\overline{k},w)$ is the plasma dielectric function.

The energy transferred to the plasma via this field is

$$W = -\int \overline{J}\cdot\overline{E}\,dt\,d\overline{x}\;, \tag{2.15}$$

in which the current density $\overline{J}$ is given by the continuity equation $\nabla\cdot\overline{J} - e\partial n_s(\overline{x},t)/\partial t = 0$. By taking the Fourier transform of Eqn. (2.15) and substituting Eqn. (2.14) for $\overline{E}(\overline{k},\omega)$ we obtain

$$W = \frac{4e^2}{(2\pi)^3}\int d\overline{k}\,d\omega\,\frac{\omega}{k^2}\,\mathrm{Im}\left(\frac{1}{\varepsilon(\overline{k},\omega)}\right)\left|n_s(\overline{k},\omega)\right|^2\;, \tag{2.16}$$

where the imaginary term is used for a real energy. The time averaged power per unit volume transferred to the plasma can be obtained by substituting $n_s(\overline{k},\omega)$ (by Fourier transforming Eqn. (2.13)) into Eqn. (2.16), then integrating with respect to $\overline{k}$ and taking the derivative with respect to ω. This gives

$$P = \frac{\omega_0}{2}\,\frac{E_0^2}{8\pi}\sum_{ki}\left(\frac{\delta n_{ki}}{n_c}\right)^2\mathrm{Im}\left(\frac{1}{\varepsilon(\overline{k},\omega)}\right)\cos^2\theta_i\;, \tag{2.17}$$

where n_c is the critical density and θ_i is the angle between $\overline{k}_i$ and $\overline{E}_0$.

The effective collision frequency is then calculated from the energy balance equation $P = \nu_{eff}(E_0^2/8\pi)$, yielding

$$\nu_{eff} = \frac{\omega_0}{2}\sum_{ki}\left(\frac{\delta n_{ki}}{n_c}\right)^2\mathrm{Im}\left(\frac{1}{\varepsilon(k,\omega)}\right)\cos^2\theta_i\;. \tag{2.18}$$

If we assume an ion turbulence which is broad in angle and extends over a region of wavenumbers, then the average effective collision frequency can be written in the form

$$\nu_{eff} = \frac{\omega_0}{4}\left|\frac{\Delta n}{n_c}\right|^2 \left< \mathrm{Im}\,\frac{1}{\varepsilon(\overline{k}_i,\omega_0)} \right>, \tag{2.19}$$

where Δn is the mean density fluctuation and the brackets denote an average over the range of wavenumbers. In order to estimate ν_{eff} the function $< \mathrm{Im} \frac{1}{\varepsilon(\bar{k}_i, \omega_0)} >$ averaged over a uniform spectrum of ion fluctuations between $k/k_D = 0.1$ and $k/k_D = 1$ was plotted and is shown in Fig. 2.16 as a function of density for a Maxwellian oxygen plasma. As shown in Fig. 2.16, the function $< \mathrm{Im} \frac{1}{\varepsilon(\bar{k}_i, \omega_0)} >$ is significant near $n/n_c = 0.8$. At this density and for plasma conditions $T_e = 100$ eV, $z = 6$ and $\Delta n/n_c = 0.1$, the effective collision frequency $\nu_{eff} \simeq \nu_{cl}$ (where ν_{cl} is the classical inverse bremsstrahlung collision frequency). For higher temperatures and low z, $\nu_{eff}/\nu_{cl} >> 1$.

Evidently, the above analysis assumed a given ion fluctuation level regardless of the source or the cause of the fluctuations. As we have discussed earlier ion fluctuations can be generated by parametric processes in the presence of a strong electromagnetic pump. The presence of such a pump could by itself modify the plasma dispersion function and thus the collision frequency. The effect of a high frequency electromagnetic field on electron collisionality was considered recently by Rozmus *et al.* [27] for a stable plasma. An approximate expression for ν_{eff} is given by

$$\nu_{eff}/\omega_0 \simeq -\left(\frac{n_e}{n_c}\right)\frac{8\pi z e}{E_0^2} \int \frac{d\bar{k}}{(2\pi)^3}(\bar{k}\cdot\bar{E}_0) \int d\bar{u}_i \, \frac{F_i(\bar{u}_i)}{|\Gamma(\bar{k}, \bar{k}\cdot\bar{u}_i)|^2} \cdot$$

$$\sum_j J_j J_{j-1} \, \mathrm{Im} \frac{\chi_e^{-j}(\bar{k}, \bar{k}\cdot\bar{u}_i)}{D_e^{-j}(\bar{k}, \bar{k}\cdot\bar{u}_i) D_e^{-j+1}(\bar{k}, \bar{k}\cdot\bar{u}_i)} \, , \qquad (2.20)$$

where $\Gamma(\bar{k}, \bar{k}\cdot\bar{u}_i)$ is the general dispersion function given by Eqn. (2.6) and the remaining terms are as defined previously.

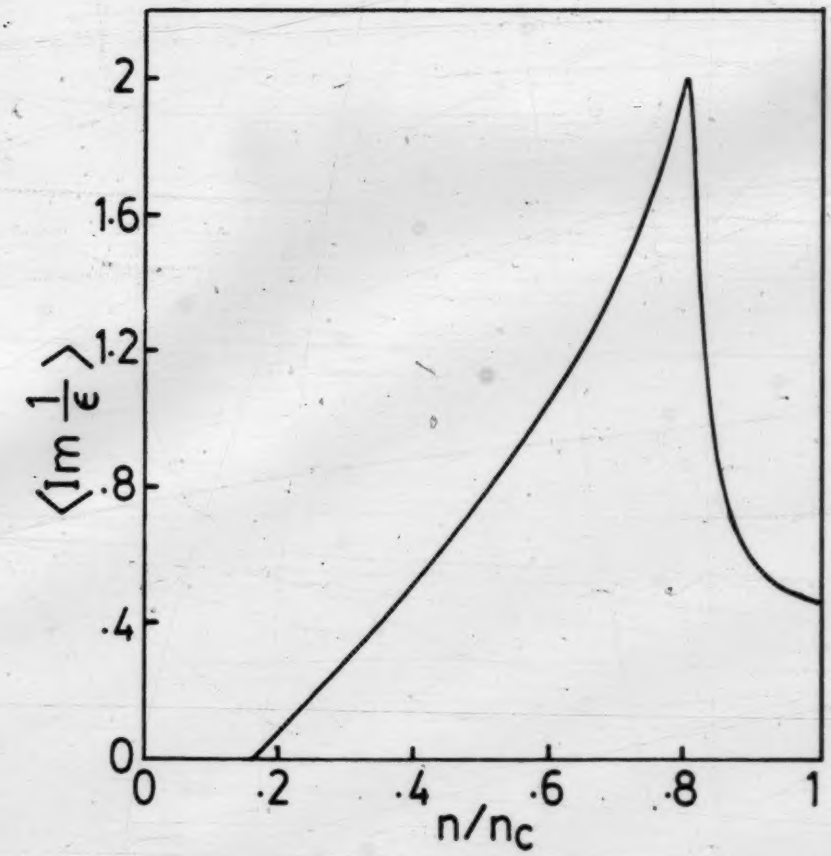

Fig. 2.16 Im $\frac{1}{\varepsilon(\bar{k}_i, \omega_0)}$ averaged over a uniform spectrum of ion fluctuations as a function of density for a Maxwellian oxygen plasma with $T_i = T_e = 100$ eV.

The factor under summation can be reduced to $\mathrm{Im}\,\dfrac{1}{D_e(\overline{k},\overline{k}\cdot\overline{u}_i)}$ for the small pump limit which is similar to the factor appearing in the Faehl-Kruer expression (2.19). In addition, enhancement can occur when $\Gamma(\overline{k},\overline{k}\cdot\overline{u}_i)$ is at or near resonance. It is important to note that even for sub-threshold pump, significant enhancement of collision frequency is possible. For example, for an oxygen target ($z=6$, $A=16$), $T_i = T_e = 100$ eV and $n = 0.8n_c$, expression (2.20) gives $\nu_{eff} = 3\nu_{cl}$, for the $\overline{k}$ vector along the direction of $\overline{E}_0$, corresponding to the least damped mode and v_0/v_e below the threshold for the PD off-resonance instability. For lower densities where the threshold is relatively high, even larger enhancements over classical are obtained. However, Eqn.(2.20) is only valid for stable plasma and represents the lowest enhancement limit. With a pump strength above the threshold for PD and OTS off-resonance the enhancement can be substantially larger. Consequently, plasma absorption may be expected to be enhanced over classical when large ion fluctuations are induced. This may occur even for pump waves below threshold for parametric instabilities, though clearly significant effects may be anticipated for above-threshold pump waves.

CHAPTER 3

EXPERIMENTAL METHODS AND TECHNIQUES

3.1 Introduction

A number of experimental methods and techniques were applied in the course of studying ion turbulence in laser plasma interactions. It is in this chapter of the thesis that these methods and techniques will be outlined in some detail. The experimental setup consists mainly of two sections. First, the part in which the plasma was formed and heated using an intense pulsed CO_2 laser and a gas jet target is presented. The second section is concerned with the diagnostic techniques which in turn is divided into two; one for measuring the different plasma parameters such as density and temperature and the other for studying ion turbulence by means of a ruby laser Thomson scattering technique. In the forthcoming sections the laser plasma experiment, its diagnostic techniques and related topics will be discussed in this order.

3.2 Laser Plasma Experiment

3.2.1 Carbon dioxide laser.

A transverse **excited** atmospheric (TEA) type pulsed CO_2 laser was used for studying laser plasma interactions. This laser was designed and built at the University of Alberta |1| and a full description will be given here.

The laser consisted of six pairs of opposing aluminum and graphite electrodes. Each electrode was 50 cm long with a Rogowski cross sectional profile modified by a 3.7 cm wide flat area in the centre. The electrodes were connected to a two stage Marx circuit using 0.1 uF capacitors. UV preionization was provided by means of a series of 570 pf capacitors driving pin discharges. These pins were situated 6 cm apart along both sides of the main discharge volume and were electrically connected in parallel with the main discharge electrodes. The total gain length of the laser was 3 m and the unstable optical cavity resonator was formed using two mirrors 4 m apart.

An unstable resonator has many advantages over a stable one. Some of these advantages are the high energy extraction for having larger mode volume, the discrimination against high order transverse modes and the most important of all is the low output beam divergence. The cavity mirrors for this laser were designed to give a positive type unstable resonator with ∿ 85% output coupling. The system was operated at a charge voltage of ∿ 55 kV and a gas mixture of approximately 70% He, 22% CO_2 and 8% N_2. It should be noted that the system was designed for a more favorable gas ratio (43% He, 43% CO_2 and 14% N_2), however, because of deterioration in the electrodes and electrical components the He concentration in the gas mix was increased to eliminate arcs between the electrodes.

Table 3.1 lists the main features of this laser. The output laser pulse consisted of a multi-transverse mode structure, approximately 4 × 4 cm in cross section, with an initial gain switched spike peak of approximately 700 MW in a pulse duration of ∿ 50 ns. Figure 3.1 shows a typical pulse shape of the existing CO_2 laser as recorded by a Ge:Au detector. Similar results were obtained theoretically by

Wavelength	10.6 μm
Storage Capacitance	1.2 μf
Preionization	50 discharge pins each side
Active Volume	3.7 cm × 3.7 cm × 300 cm
Electrical Efficiency	∿ 2.7%
Cavity Length	4 meter unstable resonator
Rear Mirror	12.8 m radius of curvature, 5 cm diameter
Front Mirror	-5 m radius of curvature, 1 cm diameter
Gas Mixture (CO_2:N_2:He)	22:8:70
Output Energy	∿ 40 Joules
Peak Power	∿ 700 MW gain switched
Pulse Duration	∿ 50 ns
Beam Divergence	∿ 0.5 mrad

Table 3.1 Features of the CO_2 TEA Laser

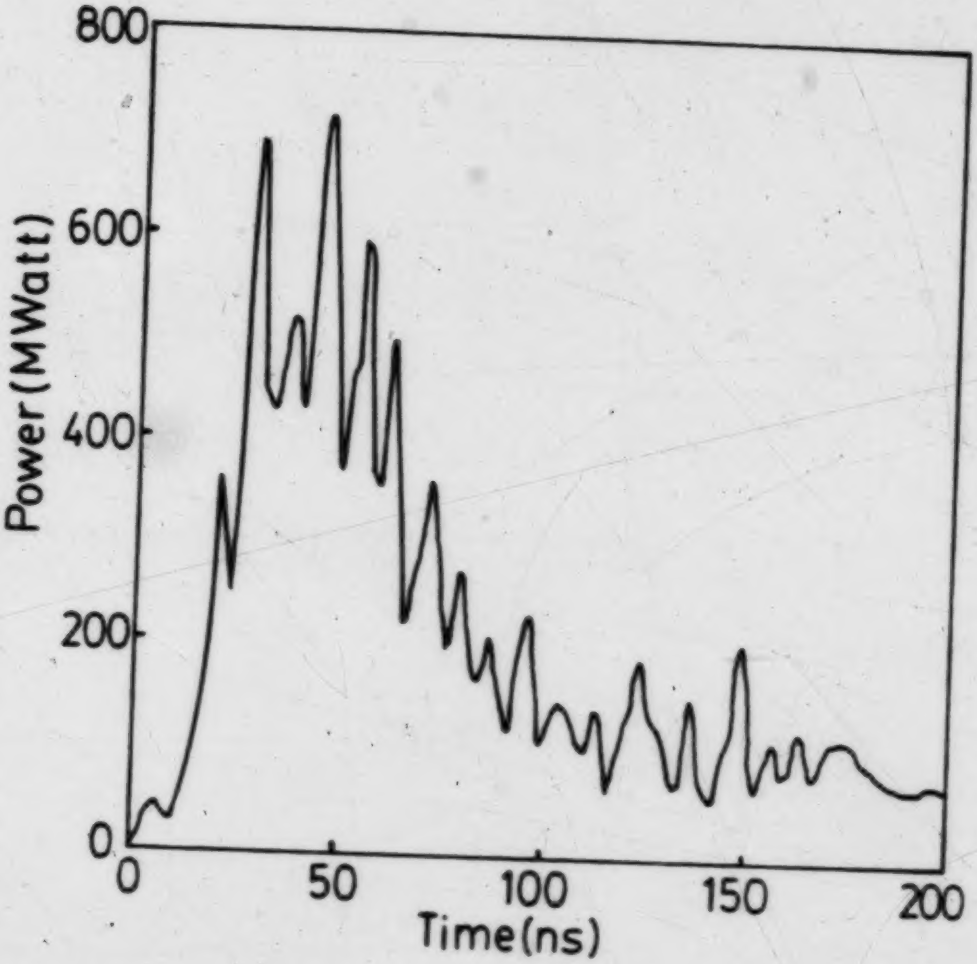

Fig. 3.1 Gain switched CO_2 laser output.

numerically solving the kinetic rate equations (Appendix B). These results are shown in Fig. 3.2. It should be noted, however, that the calculations do not predict the temporal fine structure shown in Fig. 3.1. This structure is usually observed due to the presence of several modes in the cavity.

3.2.2 Gas jet and target chamber.

A cylindrical aluminum target chamber 75 cm in diameter and 30 cm in height with a 4 cm thick plexiglass top was used throughout the course of these investigations. A base pressure of ∿ 10^{-3} torr inside the chamber was readily achieved using a 15 cfm rotary pump. A NaCl window was fitted onto the chamber in such a way that normal incidence of the CO_2 laser beam could be avoided. In addition, the chamber was provided with seven large ports which could be used for windows in order to attain optical access for different diagnostics (Fig. 3.3). The chamber pressure was maintained at ∿ 10 torr of He pressure during the experiment and was evacuated and back-filled with fresh He every time the laser was focused on the gas target.

A gas jet assembly, developed by Burnett *et al.* |1|, was used to provide the gas target. Near laminar flow was obtained by pulsing high pressure (∿ 2000 torr) oxygen gas through a convergent-divergent (supersonic) nozzle into the 10 torr He background. Equilibrium between O_2 and He was reached in ∿ 2 ms, forming a ∿ 1.5 mm thick and a 1 cm wide target. The optimal oxygen to helium pressure ratio (2000:10) was necessary in order to produce a stable laminar O_2 flow with a minimum He background. The oxygen flow was measured utilizing ruby laser shadowgraphy. The neutral O_2 density of the jet was not uniform but rather varied as a function of both height and thickness.

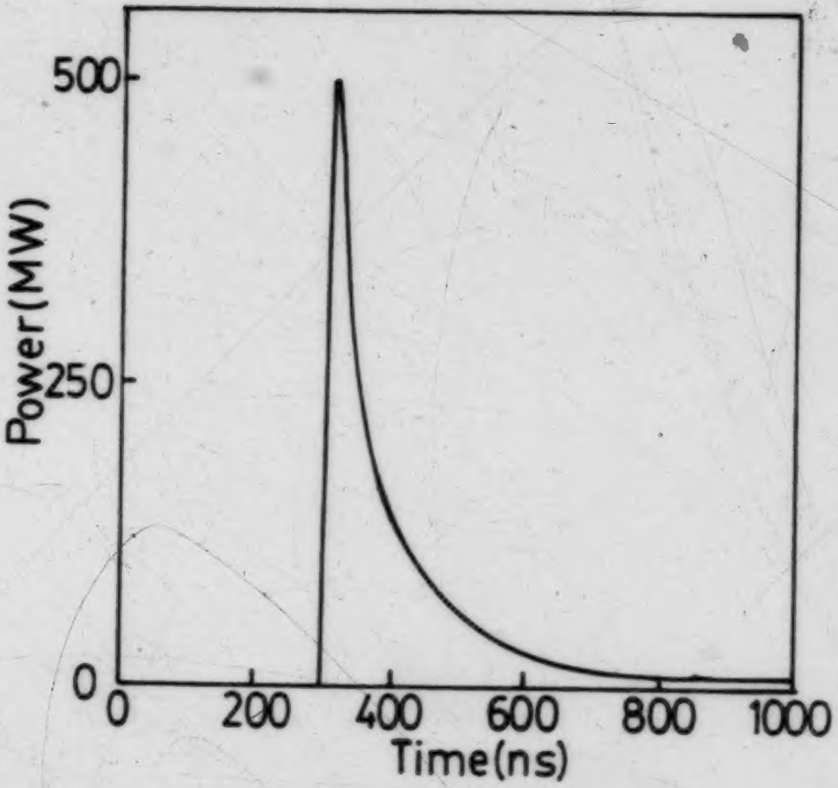

Fig. 3.2 Output of the CO_2 laser model.

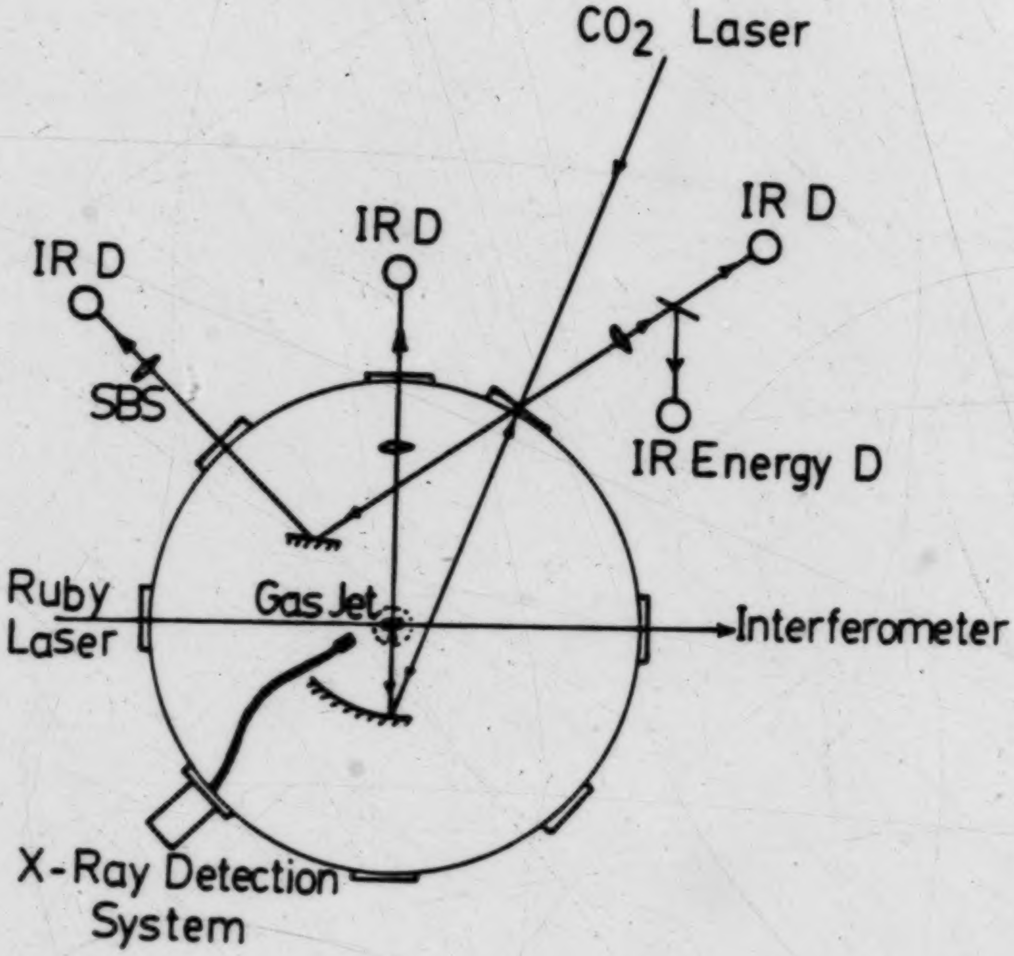
CO_2 Laser
IR D
IR D
IR D
SBS
IR Energy D
Ruby Laser
Gas Jet
Interferometer
X-Ray Detection System

Fig. 3.3 Schematic diagram of the CO_2 laser plasma interaction experiment and various diagnostics.

The hydrodynamic calculations of Giles |2| showed that at 4 mm above the nozzle (where the laser beam was focused) the jet consisted of a high density region ($\sim 1.5\times10^{18}$ molecule/cm^3) located between an inner low density region ($\sim 2.2\times10^{17}$ molecule/cm^3) and an outer low density region ($\sim 6.5\times10^{17}$ molecule/cm^3). If it is assumed that all the oxygen atoms in these regions were ionized to the degree $z = 6$ then this will lead to the formation of a nonuniform electron density distribution (between 1.75 n_c and 0.29 n_c). This nonuniformity, however, is very transient because of heating and subsequent hydrodynamic expansion.

Many unique features of the gas target make it preferable to a solid target. These features include: (a) variable density n from above critical to below critical; (b) nondestructive target which can be pulsed just prior to the firing of the laser; (c) good diagnostic access for measurements.

In brief, the laser firing operation can be explained with the help of Figs. 3.4 and 3.5 as follows:

(a) The high pressure oxygen gas is admitted into reservoir B and to the chamber upon triggering the solenoid valve between reservoirs A and B.

(b) A delayed signal from a piezoelectric pressure transducer B is used to trigger an EG&G high voltage pulse generator which in turn triggers the main laser spark gaps. The delay time is adjusted so that the laser is fired at the peak of the pressure transducer. Typical time jitter in the laser system was 10-20 ns.

The only remaining component in the target chamber to be described here is the parabolic mirror used for focusing the CO_2 laser beam. This mirror was made of an aluminum substrate (13 cm in diameter and 10 cm

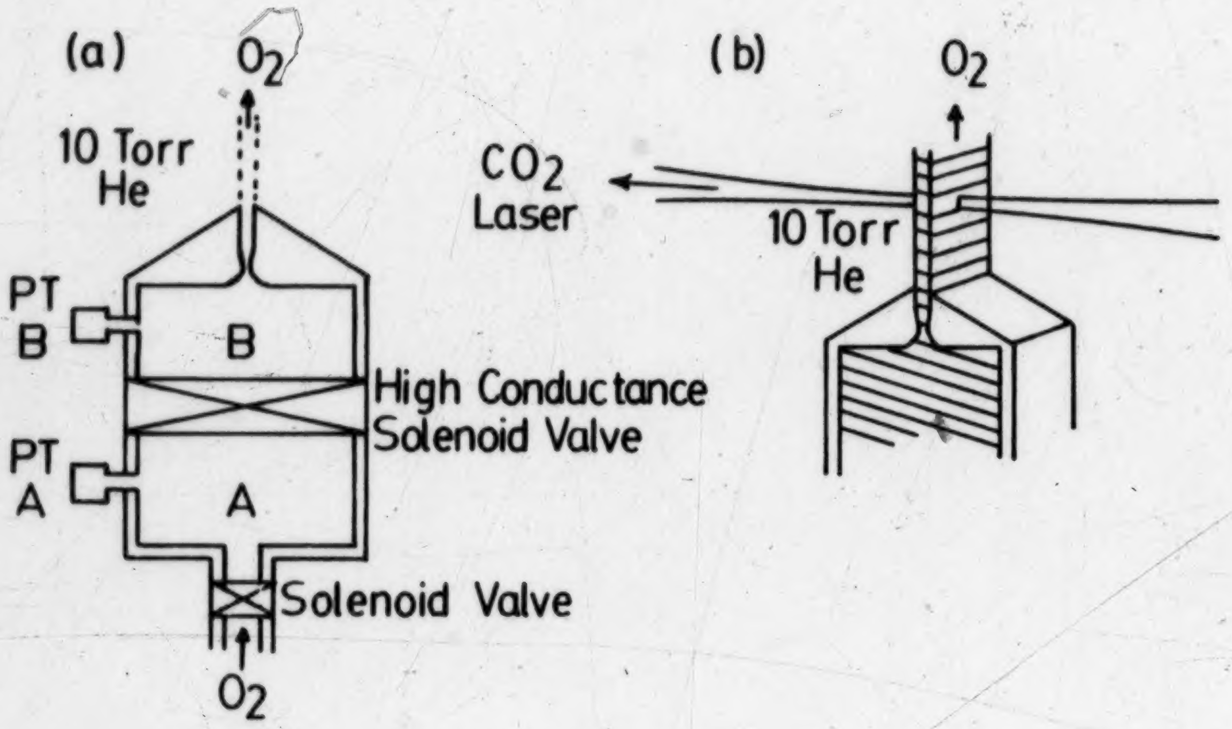
(a)
O2
10 Torr He
PT B
B
High Conductance Solenoid Valve
PT A
A
Solenoid Valve
O2
(b)
O2
CO2 Laser
10 Torr He

Fig. 3.4 Gas target design.

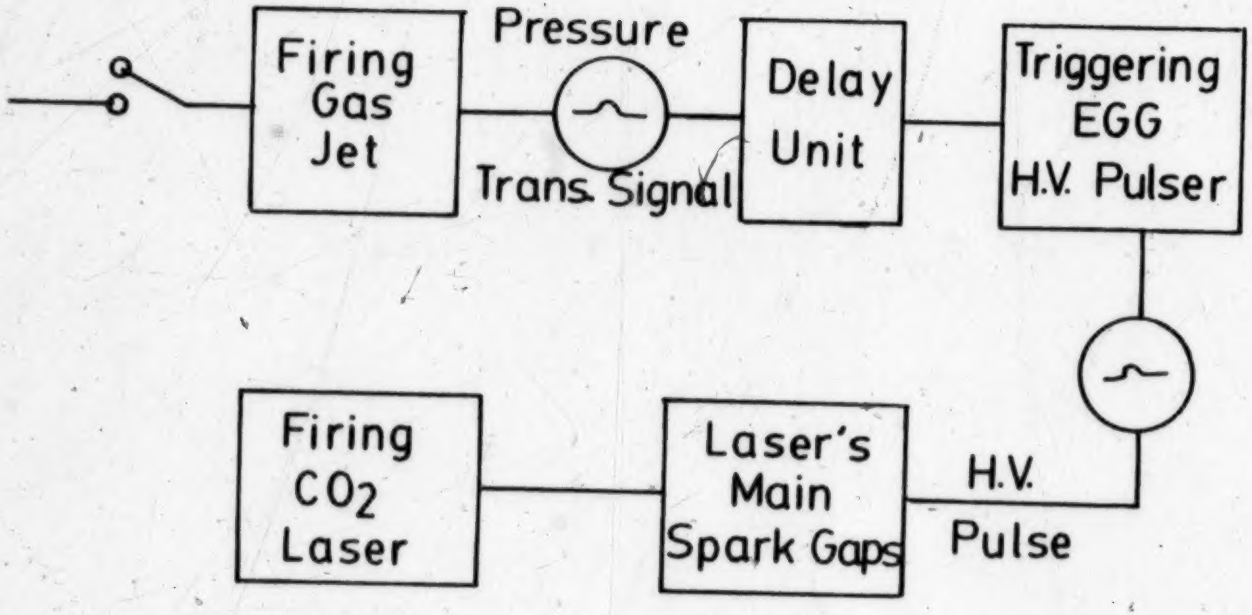
Firing Gas Jet
Pressure
Trans. Signal
Delay Unit
Triggering EGG H.V. Pulser
H.V. Pulse
Laser's Main Spark Gaps
Firing CO_2 Laser

Fig. 3.5 Firing sequences of the CO_2 laser.

focal length), coated with copper and then overcoated with gold for high reflectivity and high damage threshold |3|. A mirror holder that could be moved or tilted in order to focus the laser beam anywhere within the gas target was used. The approximate focal point size was determined by measuring accurately the laser beam divergence and mirror focal length. The beam divergence was determined from a focal beam waist calculation for the half power point using a long focal length mirror. For a 10 cm mirror focal length and a 0.5 mrad beam divergence the minimum focal spot size is 50 μm. However, this is only true for an ideal, aberration free mirror. More accurate calculations were done by Giles |2| for the mirror used in these studies using a ray tracing technique and a direct measurement of the mirror radius of curvature. These calculations showed that 60 to 70 percent of the incident laser power was within a 100 μm diameter spot (this corresponds to a focal point laser beam intensity of $\leq 5 \times 10^{12}$ w/cm^2). The approximate focal depth of the system was 800 μm. At the axial position of peak intensity, the beam FWHM was 60 μm. It should be noted, however, that according to Giles' calculations, a significant fraction of the incident power could be off-axis by 150 microns.

3.3 Measurements of Plasma Parameters

3.3.1 Infrared (IR) radiation detection.

Different types of IR power detectors were used during the course of these investigations. For relatively strong signals such as the incident and transmitted laser radiation, simple photovoltaic or photo-conductive type detectors were adequate. Examples of these types of detectors are the Rofin photon drag model 7400 ($\sim$ 1 ns risetime and responsivity of 0.5 μV/W into 50 Ω resistor) or its duplicate homemade detector. For weaker signals such as the $2\omega_0$ and $3/2\omega_0$ harmonics and stimulated Bruillouin scattering (SBS), a liquid nitrogen cooled, gold doped germanium (Ge:Au) photodetector ($\sim$ 1 ns risetime and responsivity of $\sim$ 0.2 V/W into 50 Ω at $\lambda \sim 10$ μ) was used. In both cases the output was amplified by Avantek preamplifiers (0.9 ns risetime and 30-40 dB gain). For even faster response detection a pyroelectric detector ($\sim$ 100 ps risetime and responsivity of $\sim$ 5 μV/W into 50 Ω) directly coupled to a Tektonix 7104 oscilloscope (1 GHz) was used.

The laser output energy was measured with a pyroelectric thermal detector (Gen-Tec ED-200) which has a time response of 5 ms and a known responsivity of 5 volts per joule into a 1 megohm resistance. The power was then determined from $\int P(t)dt = E$, where $P(t)$ is the instantaneous power and E is the total energy. This allowed many power detectors to be calibrated by simultaneously monitoring the power and energy using NaCl etalons of known reflectivity and Mylar of different thickness for attenuation.

As was mentioned before, an NaCl window was mounted to the chamber in such a way that normal incidence of the laser beam was avoided. This arrangement not only prevented damaging the laser optics but it also made the simultaneous measurements of both the SBS backscattering and the incident radiation possible (Fig. 3.3).

The SBS, transmitted and incident radiation signals were accurately synchronized by carefully measuring the optical paths and adjusting the cable lengths so that any of these signals could be used as a reference for timing other signals.

3.3.2 Electron temperature (T_e).

The electron temperature was measured using the x-ray foil absorption method. To apply this technique the x-ray spectrum was assumed to be dominated by free-free bremsstrahlung radiation (the recombination and line radiation must be very small). This is true for a single species plasma with no impurities present and for temperature in the range $T_e \geq 100$ eV |4|. The above assumption was checked and was found valid for our O_2 target using a computer code developed by Salzmann |5|.

For bremsstrahlung radiation, the intensity (I_λ) at a particular wavelength λ (and energy $E = hc/\lambda$) transmitted through an absorbing foil of thickness x with an absorption coefficient μ, is given by |6|

$$I_\lambda \propto \lambda^{-2}(kT_e)^{-\frac{1}{2}}\exp(-E/kT_e-\mu x) \; . \qquad (3.4)$$

In practice, Eqn. (3.4) must be integrated over a wide range of wavelengths to give the total intensity I. The simplest way of determining the electron temperature is to plot the ratio of two x-ray intensities I_1/I_2 for two different foil thicknesses (according to Eqn. (3.4) after being integrated) versus temperature. The intensity ratio I_1/I_2 is then measured experimentally for the two foil thickness. The corresponding electron temperature is finally obtained from I_1/I_2 versus temperature curve. Since the error in using only one pair of foils can be large, a more reliable method - a multifoil technique - was used and is explained in Fig. 3.6. Equation (3.4) was first integrated numerically over a photon range (up to 1000 eV) with a fine mesh near the absorption edges for different foil thicknesses and different electron temperatures. Secondly, the resultant intensities were normalized to the intensity at a foil thickness $x = 3$ µm (the

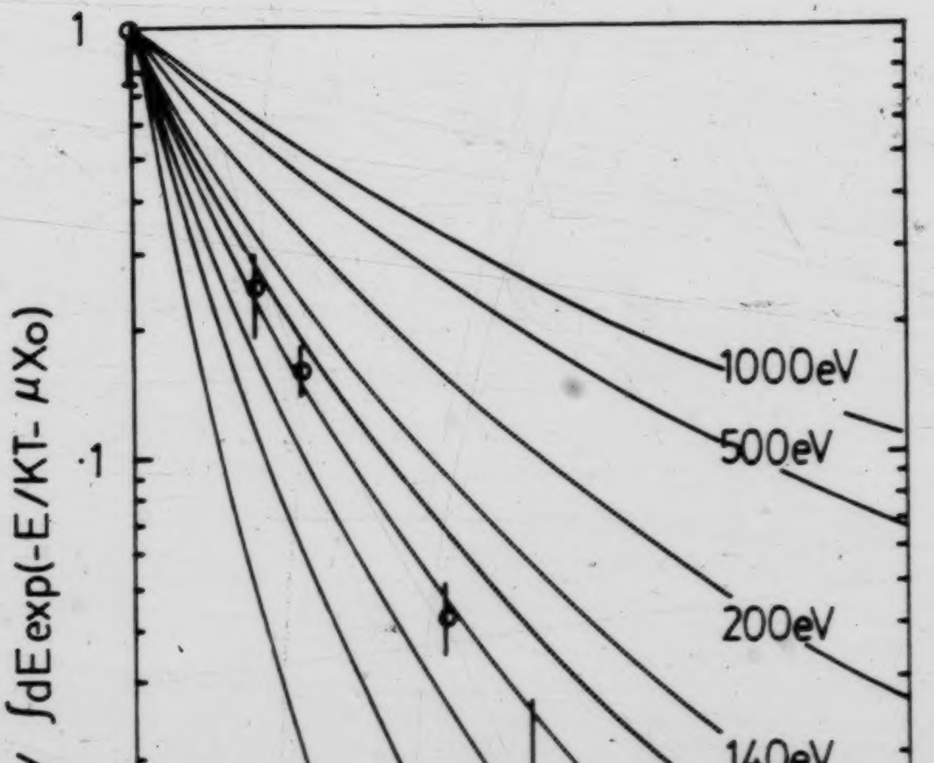

Fig. 3.6 Normalized x-ray intensity as a function of aluminum foil thickness. The circles are experimental data from the CO_2 laser plasma experiment.

thinest foil used experimentally). To determine the electron temperature the x-ray intensity was measured for different foil thicknesses, normalized to the measured intensity at $x = 3\mu m$ and plotted in the same figure. Comparison with the experimental data shows that an electron temperature of $\sim$ 100 eV provides a best fit. The total uncertainty in temperature measurement using this technique is $\leq 20\%$ (limited by the shot to shot variation in the x-ray signal) including the uncertainty due to variation in the plasma condition.

To utilize the above method a simple x-ray detector was designed (Fig. 3.7a). It consisted of an aluminum cylinder ($\sim$ 1.5 cm long and 1.5 cm diameter) arranged to accommodate one end of a low loss fiber optic bundle and to hold a plastic scintillator type NE102A ($\sim$ 1 cm in diameter and 2 mm thick). Aluminum foils ($\geq 3\mu m$ thick) were used to filter the x-rays reaching the scintillator. These filters were held adjacent to the detector body by a plastic ring and a screw mounted, thick aluminum cap. The other end of the fiber optic bundle was connected to an RCA-8645 photomultiplier tube. The scintillator, fiber optic bundle and photomultiplier tube were all sealed against any light leakage from outside. The photomultiplier signal was amplified by an Avantek preamplifier and recorded on a Tektronix 7834 storage oscilloscope with 7A19 vertical amplifiers (400 MHz bandwidth). A typical x-ray signal ($T_e << 1$ keV emission) is shown in Fig. 3.7b. For higher energy x-rays, the pulse width is considerably shorter (characteristic of a nonthermal electron distribution).

3.3.3 Electron density (n) measurement.

A reliable method for measuring electron density in high temperature and high density plasmas is laser interferometry. This technique

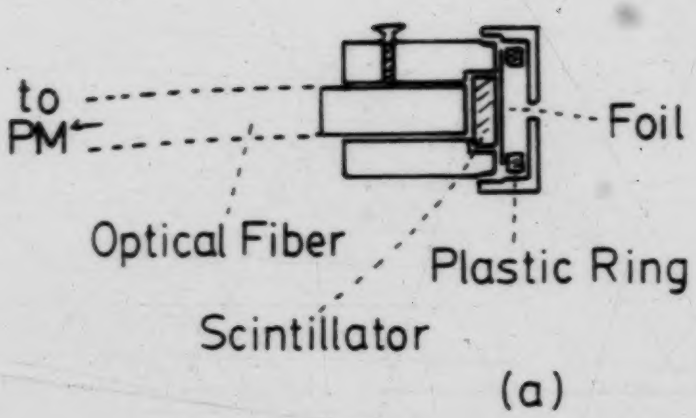
to
PM
Foil
Optical Fiber
Plastic Ring
Scintillator
(a)

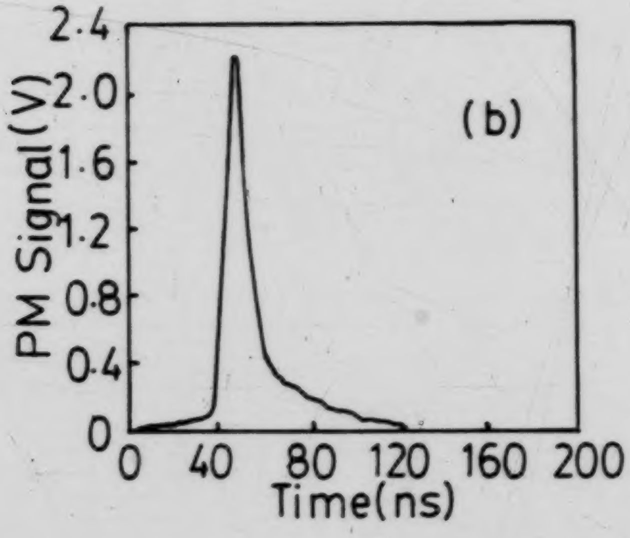

Fig. 3.7 a) X-ray detector b) Typical x-ray signal for $T_e << 1$ keV.

is based on measuring the density from the phase shift of an electromagnetic wave as it propagates along two paths of equal length, one through the plasma and the second through a vacuum. In a fully ionized plasma with zero external magnetic field and collisionless electrons the plasma refractive index μ, defined as the ratio of phase velocity in vacuum to phase velocity in the plasma, for light frequency $\omega_0 >> \omega_{pe}$, is given by |7|

$$\mu = \left(1 - \frac{\omega_{pe}^2}{\omega_0^2}\right)^{\frac{1}{2}} \simeq 1 - \frac{e^2 \lambda_0^2 n}{2\pi m c^2} , \tag{3.5}$$

where λ_0 is the probing laser light wavelength. The phase difference $\Delta\phi$ between the two paths of equal length L as the electromagnetic wave propagates through is given by

$$\Delta\phi = \int_L |1 - \mu(y)| \frac{2\pi}{\lambda_0} dy = \frac{e^2 \lambda_0}{mc^2} \int_L n(y) dy , \tag{3.6}$$

where y is the abscissa along the path L. The shift in units of fringes (N) is then given by

$$N = \frac{\Delta\phi}{2\pi} = \frac{e^2 \lambda_0}{2\pi m c^2} \int_L n(y) dy . \tag{3.7}$$

If the plasma is assumed to be cylindrically symmetric, it is possible to deduce, from the value of N as given by Eqn. (3.7), the electron density along the path L using an Abel inversion algorithim (Appendix C).

For our experiment, different interferometers were tried to measure the electron density. Both Mach-Zehnder and folded wavefront interferometers were found to be inadequate because of the low ruby laser intensity resulting from the sub-nanosecond pulse, expanded beam and the 50% reduction in the light intensity arising from the wavefront division. Best results were obtained by using the Fresnel's bimirror interferometer. This interferometer has two advantages over the above interferometers: (a) minimum optical components (simple to adjust) and, (b) minimum reduction in light intensity (only due to the mirrors' reflectivities).

The optical system for Fresnel's bimirror interferometer is shown in Fig. 3.8. The expanded and collimated ruby laser light passes through the plasma at s_1. Only half the beam is used as the test beam while the other half is the reference beam. The two lenses L_1 and L_2, separated by $f_1 + f_2$ (f_1 and f_2 are focal lengths of L_1 and L_2 respectively), were used for magnifying and localizing the fringes at the plasma. The Fresnel's mirrors were placed close to L_2 with the contact edges at the centre of the beam and were incident at an angle θ to each other. The two halves of the beam were overlapped at s_2' and viewed by a camera of a magnification Mc. From the thin lens equation

$$\frac{1}{s_1'} = \frac{1}{f_1} - \frac{1}{s_1} \quad \text{and}$$
$$\frac{1}{s_2'} = \frac{1}{f_2} - \frac{1}{s_2} \,. \tag{3.8}$$

The imaginary image of L_1 is a real object to L_2 with $s_2 = s_1' + f_1 + f_2$. Thus, Eqns. (3.8) can be reduced to

$$s_2' = \left(1 + \frac{f_2}{f_1} - \frac{f_2}{f_1^2} s_1\right) f_2 \,. \tag{3.9}$$

The telescope magnification is

$$M = \frac{s_2'}{s_1} \,. \tag{3.10}$$

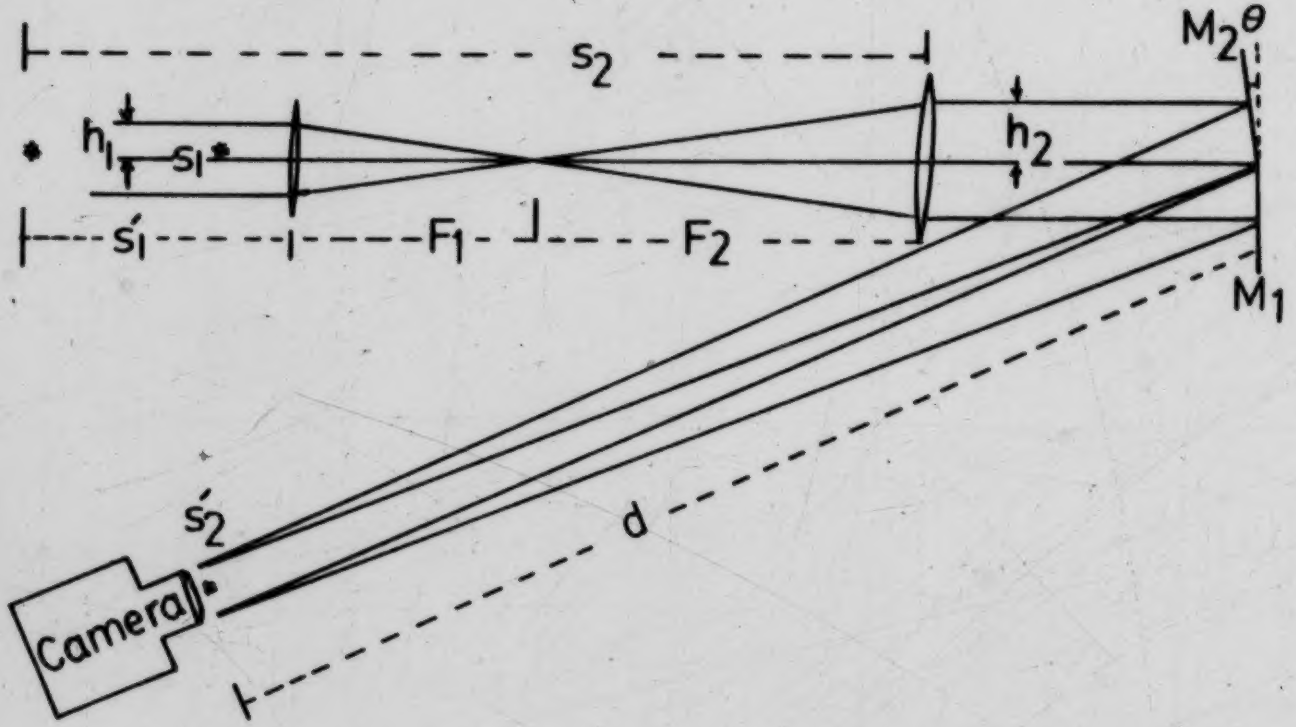
s_2
M_2
θ
h_1
s_1
h_2
s_1'
F_1
F_2
M_1
s_2'
d
Camera

Fig. 3.8 Optical system for Fresnel's bimirror interferometer.

From the interference theory of Fresnel's bimirror, the fringe spacing at s' is |8|

$$\delta = \lambda_0 d/h_2 , \tag{3.11}$$

where λ_0 is the ruby laser wavelength and $h_2 (= h_1 \frac{f_2}{f_1})$ is the width of the overlapping area. The corresponding fringe spacing in the plasma (resolution) is

$$\delta_p = \delta/M . \tag{3.12}$$

With $f_1 = 30$ cm, $f_2 = 67$ cm, $h_1 = 3$ mm, $s_1 = 26.5$ cm and $d \simeq s_2'$, Eqns. (3.9) to (3.12) give $\delta_p = 27$ μm . This value agreed very well with the resolution measured by counting the number of fringes across the field of a 200 micron diameter microsphere positioned at the CO_2 laser focus. The total magnification of the telescope and the camera was $M_T = M \times M_c \simeq 50$.

The main light source used in this interferometer was a Q-switched Korad K1 ruby laser whose features are given in Table 3.2. An optical shutter was used to slice a 300 ps pulse from the 20 ns FWHM ruby laser pulse. The shutter consisted of three major components: the Lasermetric KD*P Pockels cell, the crossed Glan-Thomson polarizers and the laser triggered spark gap (LTS).

In order to achieve the fastest switching, a solid dielectric laser triggered spark gap was employed. This permitted the shortest avalanche breakdown. The solid dielectric material used in the LTS was a piece of mylar. The switching procedure was done as follows (Fig. 3.9). The Pockels cell was aligned so that the x crystallographic axis was parallel to the polarization axis of the laser light (shown vertical). Further, the Glan-Thomson polarizer was

Wavelength	6943 Å
Polarziation	Plane polarized by intercavity Brewster stack polarizer.
Pumping	With helical Xe flash lamp.
Output Energy	∿ 2 Joule with full beam size, 0.3 J with 0.5 cm diameter inside cavity iris.
Pulse Duration	∿ 20 ns FWHM with Q-switching alone.
Beam Divergence	1.5 mrad.
Further Switching	With Pockels cell, Glan-Thomson polarizers and laser triggered spark gap.
Sliced Pulse Width	∿ 300 ps FWHM.

Table 3.2 Features of the Q-switched Ruby Laser

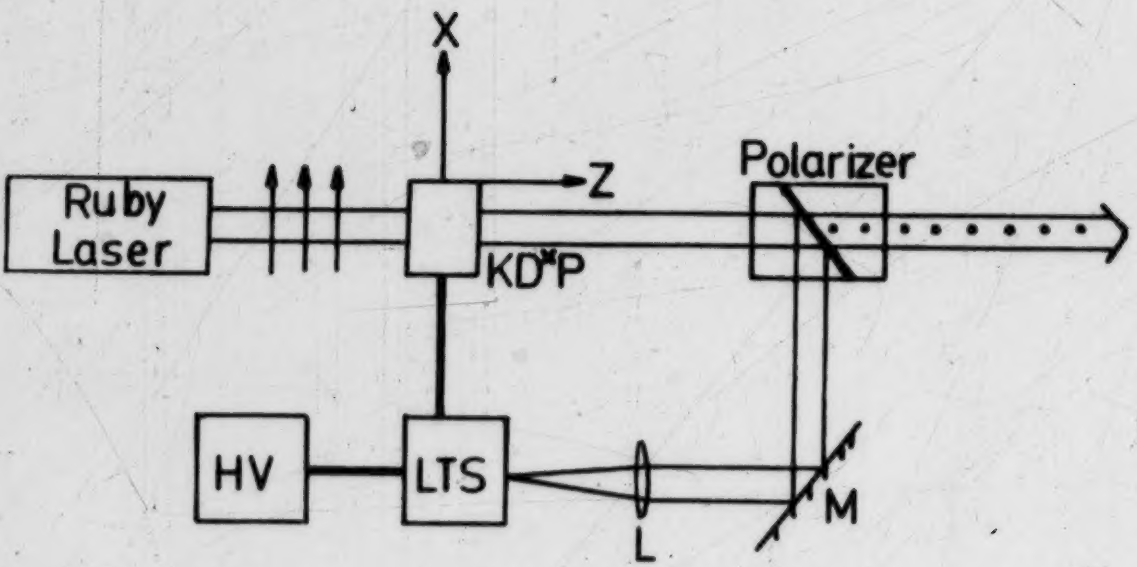
X
Z
Ruby Laser
KD*P
Polarizer
HV
LTS
L
M

Fig. 3.9 Subnanosecond switching of the ruby laser.

carefully oriented with its polarization axis perpendicular to that of the laser. The spark gap was charged to approximately twice the half-wave retardation voltage of the Pockels cell and aligned carefully so that the laser beam, reflected from the Glan polarizer, was directed to and focused onto the mylar surface of the spark gap. On firing the ruby laser, breakdown would take place in the mylar causing a fast rising voltage step across the Pockels cell, and consequently a 90° change in the high polarization orientation, which permitted the light to pass through the polarizer. The fast switching occurred during the voltage risetime from zero to full-wave value. The measured output pulse was of ∿ 300 ps duration.

The ruby laser was synchronized to the CO_2 laser with ∿ 20 ns jitter and the timing of the ruby pulse and the plasma formation was determined by monitoring the switched ruby pulse on a high speed Optic Technology photodiode and SBS radiation on a Ge:Au detector. A typical pattern is shown in Fig. 3.10.

3.4 Thomson Scattering Experiment

3.4.1 Outline of the experiment.

One of the most powerful and versatile plasma diagnostic techniques is the scattering of laser light by plasma electrons (Thomson scattering). Plasma parameters such as T_e , T_i and n as well as collective electron and ion fluctuations can be probed by this method. The main objective of using this technique in the present work was to study some features of ion turbulence and, in particular, to determine the temporal and spectral behaviour as well as the

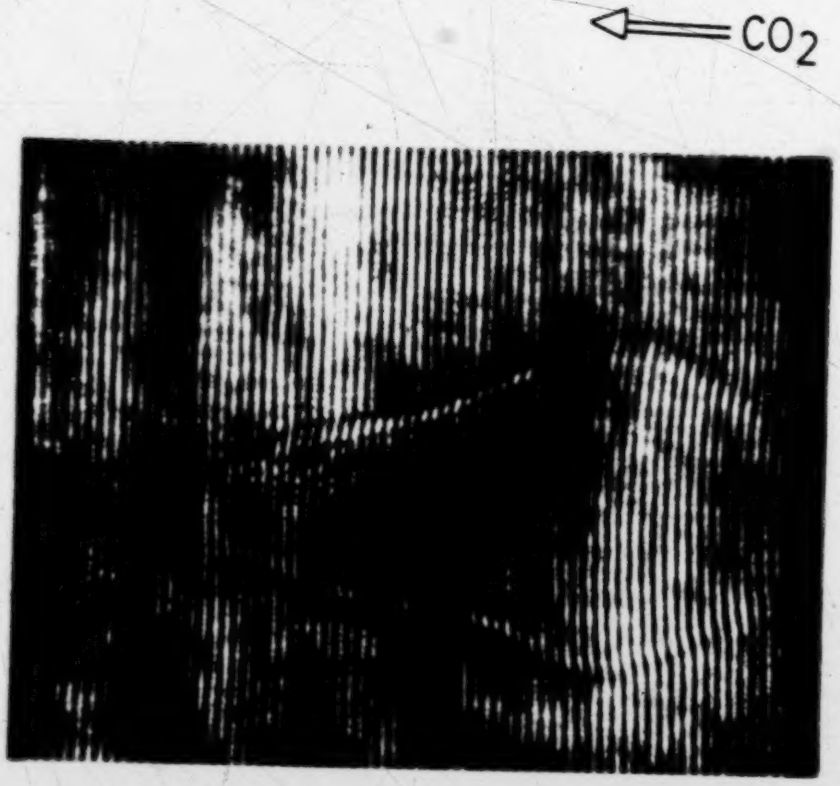

Fig. 3.10 Typical fringe pattern with 25 μm fringe spacing.

turbulence level of the ion fluctuations. Only general remarks will be given here; details of the theory can be found in the review papers of Evans and Katzenstein |9| and De Silva and Goldenbaum |10|.

It is well known that uniformly distributed charged particles scatter electromagnetic waves only in the forward direction. It is the irregularities in the density distribution (fluctuations) which give rise to net scattering in other directions. The scattering cross section is inversely proportional to the square of the particle mass and therefore light scattering is mainly due to the plasma electrons. Random density fluctuations give rise to incoherent scattering from individual electrons where the scattered power is simply the sum of the individual contributions. If the inhomogeneity is due to large scale correlated effects such as plasma waves or nonthermal fluctuations, the scattering will be coherent or cooperative and substantially enhanced over that caused by thermal fluctuations. For a plasma in thermal equilibrium these two regimes can be investigated experimentally by matching the fluctuation wave vector $\overline{k}$ to the typical shielding distance (coherence length) or the Debye length λ_D . When $k\lambda_D >> 1$ the probe's scale length will be much smaller than λ_D , hence we deal with individual electron motions. If, on the other hand, $k\lambda_D << 1$ collective effects caused by coherent electron and ion motions will be observed. In the following discussion, the parameter $\alpha = 1/k\lambda_D$ will be introduced, for convenience, to classify the two regimes.

Figure 3.11 shows a schematic diagram of the scattering geometry. A plane polarized electromagnetic wave $(\overline{k}_0, \omega_0)$ is incident on a plasma and a scattered wave $(\overline{k}_s, \omega_s)$ is observed at an angle θ. If the density fluctuation's velocity is $\overline{v}$ the observed signal will be Doppler shifted

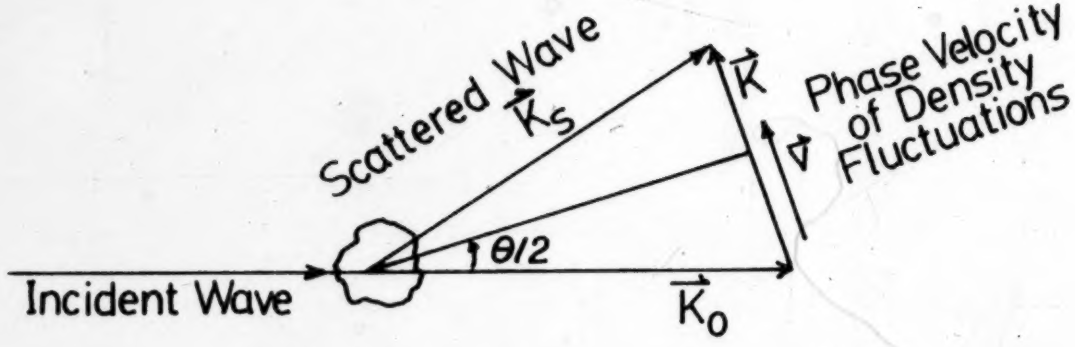
Scattered Wave
$\vec{K}_S$
$\vec{K}$
Phase Velocity of Density Fluctuations
v
$\theta/2$
Incident Wave
$\vec{K}_0$

$$\vec{K} = \vec{K}_S - \vec{K}_0$$

$$K^2 = K_S^2 + K_0^2 - 2K_S K_0 \cos\theta$$

$$\simeq 2K_0^2(1 - \cos\theta)$$

$$K = 2K_0 \sin\frac{\theta}{2}$$

Fig. 3.11 Schematic diagram of the scattering geometry.

in frequency by ω where

$$\omega = \omega_0 - \omega_s = \bar{k} \cdot \bar{v} ,$$

and (3.13)

$$\bar{k} = \bar{k}_s - \bar{k}_0 .$$

For small frequency shifts, $k_0 \simeq k_s$ and the wave number k can be approximated by

$$k = 2k_0 \sin \frac{\theta}{2} . \qquad (3.14)$$

Hence, Eqn. 3.13 can be rewritten as

$$\omega = 2k_0 v \sin \frac{\theta}{2} , \qquad (3.15)$$

and in this case the shift in wavelength $\Delta\lambda$ will be given by

$$\Delta\lambda = \frac{2\lambda_0}{c} v \sin \frac{\theta}{2} . \qquad (3.16)$$

where λ_0 is the wavelength of the incident wave.

In the individual scattering regime, $\alpha << 1$, v represents the phase velocity of the electron fluctuations while in the collective scattering regime, $\alpha >> 1$, v can be related to the phase velocity of both the ion and electron fluctuations. The role of the ions in this case (although they do not scatter) arises from the collective interaction between electrons and ions -- the ions impose fluctuations on the electrons and these fluctuations move with the characteristic ion velocity. Thus the Doppler shift observed corresponds to the ion rather than the electron velocity. Since the velocity depends on the particle temperature, the $\alpha << 1$ regime gives information about electron temperature while the ion temperature can be determined in the $\alpha \gtrsim 1$ regime.

Experimentally, the choice of the scattering angle and the laser beam wavelength determines the parameter α which, according to Eqn. (3.14), is given by

$$\alpha = \frac{\lambda_0}{4\pi\lambda_D \sin\theta/2} . \tag{3.17}$$

The scattered power as a function of frequency, $P_s(\omega)$, in a given solid angle $\Delta\Omega$ is explicitly related to the incident light intensity I_0 and the electron density through the relation

$$P_s(\omega) = I_0 n V \sigma_e S(\omega,\overline{k})\Delta\Omega , \tag{3.18}$$

where V is the scattering volume, σ_e ($\approx 8\times10^{-26}\,\mathrm{cm}^2$) is the Thomson scattering cross section and $S(\omega,\overline{k})$ is the dynamic form factor or the density spectrum defined by

$$S(\omega,\overline{k}) = \frac{3}{8\pi\sigma_e}\frac{d^2\sigma}{d\omega d\Omega} , \tag{3.19}$$

where σ is the scattering cross section.

The density spectrum $S(\omega,\overline{k})$ is a very important function in scattering, from which the full spectrum of the scattered light can be determined and consequently plasma parameters such as T_e , T_i and fluctuation level can be inferred. With Maxwellian velocity distributions for both ions and electrons in a collisionless plasma, the density spectrum is given by |9|

$$S(\omega,\overline{k}) = \frac{N}{k}\left\{\left|\frac{1-G_i}{1-G_e-G_i}\right|^2 F_e\left(\frac{-\omega}{k}\right) + z\left|\frac{G_e}{1-G_e-G_i}\right|^2 F_i\left(\frac{-\omega}{k}\right)\right\} , \tag{3.20}$$

where F_e and F_i are the Maxwell-Boltzmann velocity distribution functions for the electrons and ions respectively, z is the ionization degree, N is the total number of electrons in the scattering volume and

$$G_e(\omega) = -\alpha^2 |1 - f(x) + i\pi^{\frac{1}{2}} \cdot x \cdot \exp(-x^2) \quad ,$$

$$G_i(\omega) = -z(T_e/T_i)\alpha^2 |1 - f(y) + i\pi^{\frac{1}{2}} \cdot y \cdot \exp(-y^2)| \quad , \qquad (3.21)$$

$$x = \frac{\omega}{\omega_e} \; , \; y = \frac{\omega}{\omega_i} \; , \; \omega_e = \left(\frac{2k^2 T_e}{m_e}\right)^{\frac{1}{2}} , \; \omega_i = \left(\frac{2k^2 T_i}{m_i}\right)^{\frac{1}{2}} \; ,$$

$$f(x) = 2x \exp(-x^2) \int_0^x \exp(t^2) dt \; .$$

The first and second terms of Eqn. (3.20) are called the electron density spectrum, $S_e(\omega,\overline{k})$, and the ion density spectrum, $S_i(\omega,\overline{k})$, respectively. Examining Eqn. (3.20) shows that:

a) for $\alpha << 1$ the electron component is the predominant feature and the scattered radiation has a Gaussian form (characteristic of the random thermal motion of the electrons) where the shape is a function of electron temperature which can be deduced from its width.

b) for $\alpha >> 1$ the spectrum consists of a central narrow peak (the ion component) whose shape is a function of ion and electron temperatures (which can be determined from its width) and two minor peaks (the electron component) symmetrically displaced to either side of the central peak by a frequency $\omega = (\omega_{pe}^2 + 3k^2 v_e^2)^{\frac{1}{2}}$.

A computer program was written to determine the full spectrum $S(\omega,\overline{k})$ as given by Eqn. (3.2) (Appendix D) in order to be compared with that obtained experimentally.

Another important, measurable quantity in a scattering experiment is the total scattering spectrum $S(\overline{k})$ defined as the integral of $S(\omega,\overline{k})$ over all frequencies. $S(\overline{k})$ can be given approximately (for

$T_e > T_i$) in a thermal plasma by Salpeter |11|

$$S_e(\overline{k}) = \frac{1}{1+\alpha^2}$$

$$S_i(\overline{k}) = \frac{z\alpha^4}{(1+\alpha^2)\,|1+\alpha^2+z\alpha^2(T_e/T_i)|}\,, \tag{3.22}$$

$$S(\overline{k}) = S_e(\overline{k}) + S_i(\overline{k})\ .$$

For other conditions where the Salpeter approximation is not valid, Eqn. (3.20) must be integrated numerically.

The total scattering power, as obtained by integrating Eqn. (3.18) over all frequencies, is directly related to the total scattering spectrum $S(\overline{k})$,

$$P_s = I_0 n V \sigma_e S(\overline{k}) \Delta\Omega\ . \tag{3.23}$$

The importance of the total scattering spectrum $S(\overline{k})$ arises from its relation to the plasma density fluctuations. By definition, the spectral density $S(\omega,\overline{k})$ and the total scattering spectrum are given |12|

$$S(\omega,\overline{k}) = \lim_{V,t\to\infty} \frac{1}{Vt}\,\frac{|\delta n(\omega,\overline{k})|^2}{n_c}$$

$$S(\overline{k}) = \lim_{V,t\to\infty} \frac{1}{Vt}\,\frac{|\delta n(k)|^2}{n_c}\,, \tag{3.24}$$

where t is the time and δn is the Fourier transformed density fluctuation. According to this definition the total spectral density fluctuation averaged over all frequencies and wave numbers can be written in the form |13|

$$\left(\frac{\delta n}{n}\right)^2_{e,i} = \left(\frac{1}{2\pi}\right)^3 \frac{2}{n_e} \int_0^\infty S_{e,i}(\bar{k}) k^2 d\bar{k} \,, \qquad (3.25)$$

where e and i stand for electron and ion respectively.

It should be pointed out that the expression for $S(\omega,\bar{k})$ as given in Eqn. (3.20) or its integral is only true for a thermal plasma. For a nonequilibrium plasma the spectral density $S(\omega,\bar{k})$ and the total density spectrum $S(\bar{k})$ can be very different from that calculated for a thermal one. For the case of a plasma, in which the electrons have a net drift velocity $\bar{v}_d$ relative to the ions, the entire spectrum, $S(\omega,\bar{k})$, will be displaced in frequency by $\Delta\omega \doteq \bar{k} \cdot \bar{v}_d$ for $\alpha < 1$, while for $\alpha > 1$, the presence of drifts leads to an asymmetric and enhanced ion spectrum with the asymmetry increasing as the ratio of the electron drift velocity to the electron thermal velocity increases. The presence of turbulence or unstable modes in a plasma can also modify the scattering spectrum. The main effect is that the unstable modes grow to a large amplitude, and for these modes the spectral density function is enhanced to well above the thermal level. Consequently, this will increase the scattering level as indicated in Eqn. (3.24). The modification will depend on the type of instability generated in the plasma. As an example, the current driven ion instability gives a total spectrum of the ion feature $S_i(\bar{k})$ of the form $k^{-3}\ln(1/k\lambda_0)$ |14|.

3.4.2 Scattering arrangements.

The Q-switched ruby laser, described previously, with full pulse of ∿ 20 ns FWHM was used for Thomson scattering measurements of ion fluctuations. Further slicing of the ruby pulse was avoided to minimize jittering and to save ∿ 50% of the output power which may be lost in switching. In addition, the ruby beam was focused into the target using either an 8 or 15 cm (high quality) focal length lens to obtain a reasonable compromise between the incident intensity and stray light, particularly for small scattering angles.

The scattered light was collected by an f/5-f/6 lens (10-15 cm focal length) set at an angle $0^\circ < \theta < 180^\circ$ with respect to the incident beam either in a horizontal plane, defined by the ruby laser beam and the CO_2 laser beam, or in a vertical plane, defined by the ruby laser beam and the direction of the gas jet flow. The collected and collimated scattered light was subsequently directed by a set of mirrors towards the optical detectors. The required precision alignment was achieved by placing a microsphere ($\sim 200\,\mu m$ diameter) at the CO_2 laser focal point and illuminating it with the ruby laser alignment He-Ne laser beam. The He-Ne light scattered from the microsphere and collimated by the collecting lens was easily seen by the eye and could be traced through the optical system up to the detectors.

The stray light was severely reduced by using a variety of techniques including spatial filtering, proper dumping of the ruby laser probe beam, blackening and covering of surfaces and using Brewster windows instead of normal incidence windows. For time integrated spectral measurements and, in particular, when the full scattered spectrum was under investigation, a Kerr shutter with 5 ns gating was used to reduce detection of the relatively long-lived bremsstrahlung radiation. In addition, approximately 50% of the unpolarized bremsstrahlung radiation was always eliminated by inserting an optical polarizer in the path of the scattered light.

The timing between scattering and plasma formation was determined by simultaneously monitoring the incident ruby laser beam and either the SBS or the transmitted CO_2 laser signal with ∿ 2 ns effective resolution.

Spectral measurements of $S(\omega,\overline{k})$ were made by focusing the scattered light into a 100 μm wide entrance slit of an 0.58 m Perkin-Elmer E-1 monochromator (Fig. 3.12). The spectrally dispersed output light of the monochromator was imaged onto the target plate of a PARC type 1205D optical multichannel analyzer (OMA) using a relay lens. The OMA target plate consisted of a silicon intensified vidicon with an S-20 photocathode. The 12.5 mm target plate was a linear array of 500 channels each with 10-20 photon/count sensitivity. The OMA signal was digitized by a PARC type 1205A console, stored in a solid state memory and then recorded as an X-Y display on an oscilloscope. The overall monochromator-OMA dispersion and resolution were 0.04 Å per channel and 0.4 Å respectively. This resolution was quite adequate for studying the 0.5-2 Å range ion feature in the Thomson scattered spectrum. In addition, a deconvolution routine was used in cases where the spectral width of the ion feature and the instrumental resolution were comparable (Appendix E).

Measurement of the electron component of the scattered spectrum was made in two different ways: either by scanning the Perkin-Elmer monochomator at ∿ 10 Å intervals, or by using a 0.25 m Jarrel-Ash monochromator with a 1180 lines/mm grating to give a full spectral scan of ∿ 1500 Å on the OMA (∿ 3 Å per channel). It is for this latter case that a Kerr shutter was used.

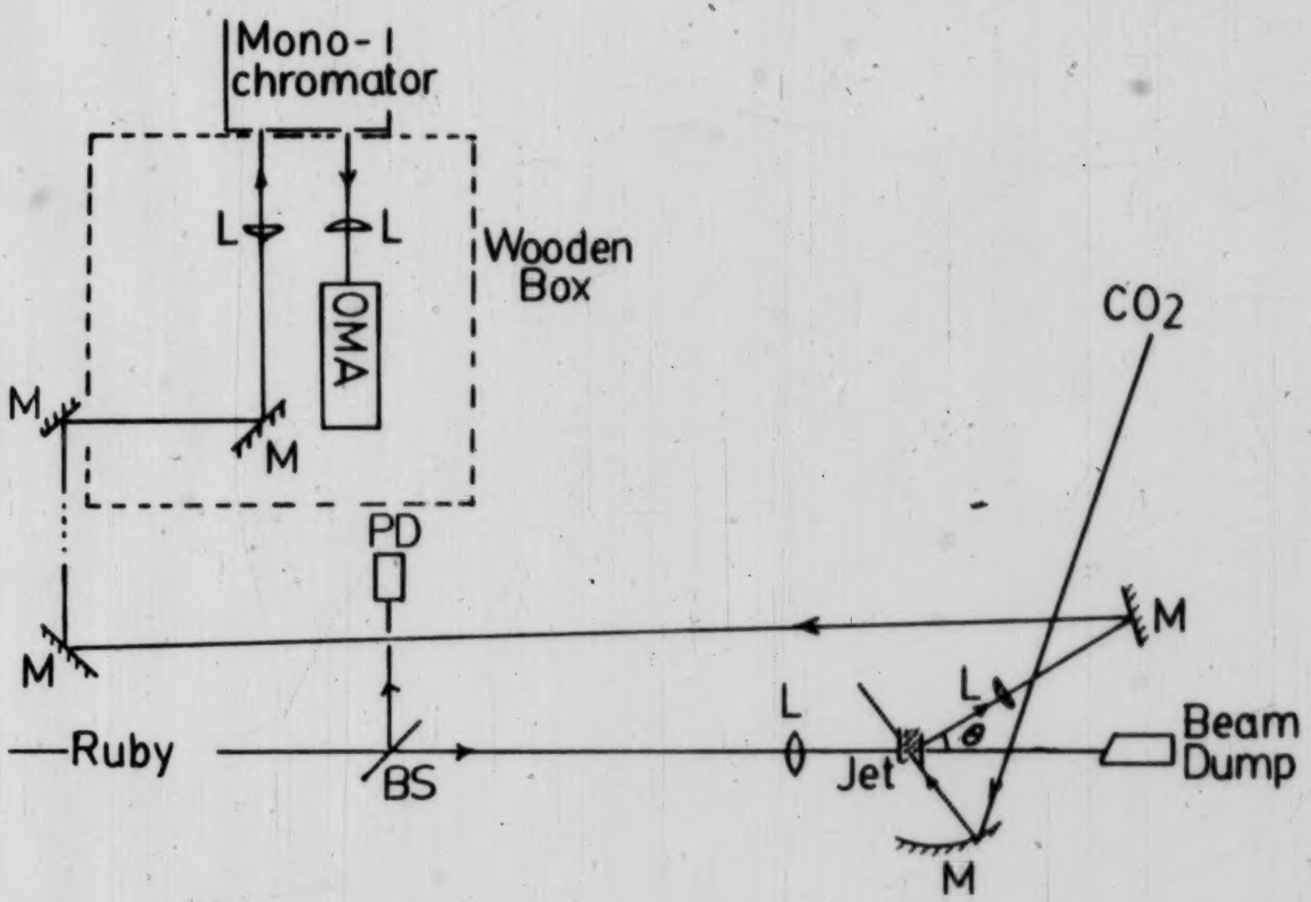
Mono-1
chromator
L
L
Wooden
Box
OMA
M
M
PD
CO2
M
M
L
L
Ruby
BS
θ
Jet
Beam
Dump
M

Fig. 3.12 Thomson scattering experiment for $S(\omega,\bar{k})$ measurements. M: mirror, L: lens, BS: beam splitter, PD: photodiode.

The $S(\overline{k})$ spectrum was measured in a vertical plane (plane of the target), i.e., probing ion fluctuations with wavevector $\overline{k}$ parallel to the electric field of the incident (unpolarized) CO_2 laser radiation, which are of particular interest for absorption. In addition, measurements were also made in a horizontal plane in order to compare turbulence levels for different directions but with the same wavenumber. Two collecting lenses were used, one fixed at a 90° angle for monitoring and normalizing purposes, and the other set at an angle $10^\circ \leq \theta \leq 90^\circ$ (Fig. 3.13). The beams collected from both lenses were imaged onto two RCA-8645 photomultipliers using two other lenses. The lens used for the main beam (scattered at angle θ) matched the collecting lens in focal length for unity magnification. An interference filter (~ 8 Å bandwidth) was used in front of the photomultiplier to discriminate the ion component from the rest of the spectrum.

For absolute measurements of $S(\overline{k})$, the scattered power (as defined by Eqn. (3.23) was calibrated by comparing the Thomson scattered signal with that due to emission from a blackbody source. Because of the high stray light levels detection of Rayleigh scattering was not possible and therefore the parameters I_0 , n, V and $\Delta\Omega$ were carefully determined: the scattering volume was determined from the intersection dimensions of the focused ruby laser, the CO_2 laser, and the collecting optics - the latter being limited by the 100 μm iris size in front of the photomultiplier; the ruby light intensity was determined by measuring the ruby laser power, energy and spatial distribution with a pinhole and long focal length lens; the solid angle was determined from the f number of the collecting lens; the electron plasma density was measured with Fresnel's bimirror

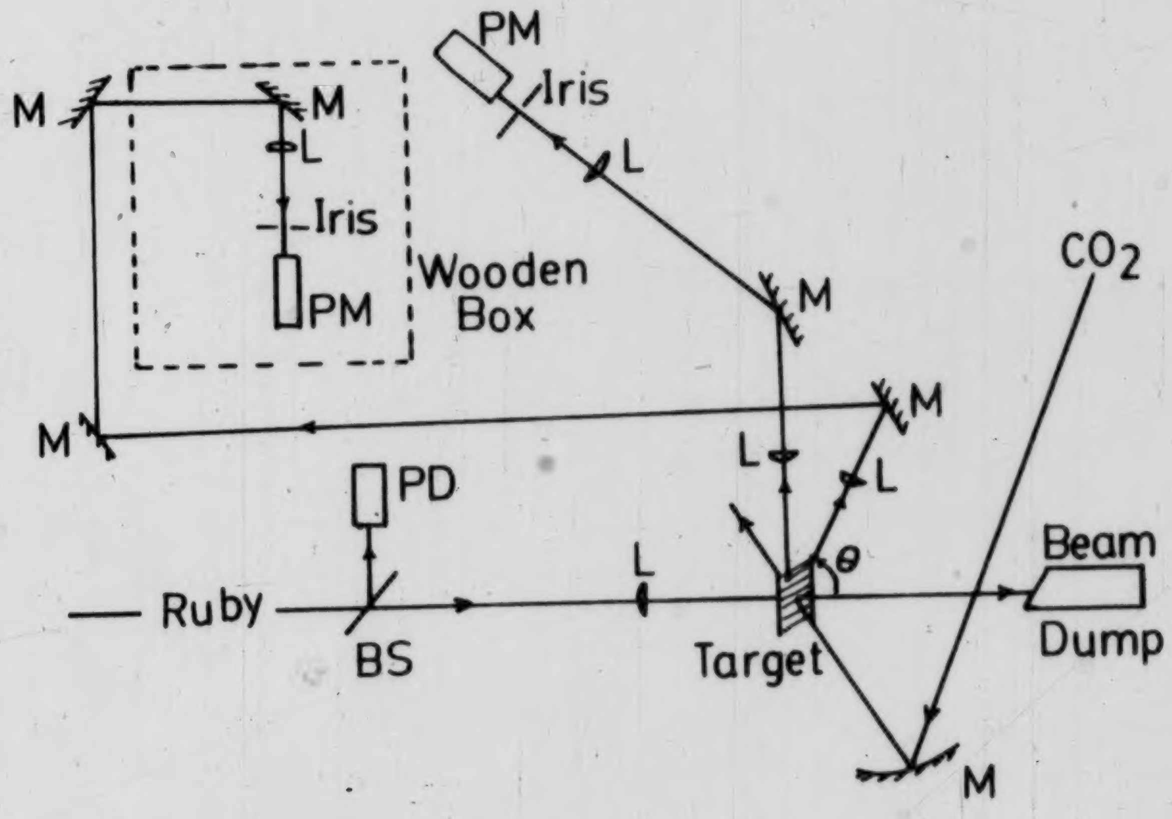
PM
Iris
L
M
L
Iris
PM
Wooden Box
M
M
M
CO2
M
L
L
PD
θ
Beam Dump
Ruby
BS
L
Target
M

Fig. 3.13 Thomson scattering experiment for streak measurements. M: mirror, L: lens, BS: beam splitter, PH: photodiode, BD: beam dump, OF: optical fiber.

interferometer as described in Section 3.3.3. The uncertainties in the parameters I_0 , n, V and $\Delta\Omega$ are approximately 5%, 15%, 5% and 1% respectively. Thus, the overall error in $S(\overline{k})$ was ∿ 26%.

The photomultipliers used for $S(\overline{k})$ measurements could only give limited information about the temporal variations of the ion fluctuations because of the relatively slow risetime (∿ 2.5 ns). Better resolution was achieved by employing a high speed Hamamatsu streak camera (Fig. 3.14). The camera system consisted of a C979 temporal disperser, C1000-18 vidicon camera and a C1330 temporal analyzer. With a 30 μm entrance slit, a resolution of up to 10 ps could be achieved. The camera information was digitized and stored in the temporal analyzer and displayed on a video monitor. The temporal analyzer also permitted the recording of the displayed information on an X-Y plotter. The viewing field had 256 time channels and 64 windows corresponding to the 3 mm long entrance slit of the camera. Approximately 10 μm per window spatial resolution was achieved when the scattered light was focused onto the camera slit with a 10 cm focal length lens.

Timing and normalizing of the Thomson scattered light with respect to the incident ruby laser beam was accomplished by illuminating one end of a 50 μm diameter optical fiber with only a fraction of the incident ruby beam while the other end was kept fixed inside the entrance slit of the camera in such a way that the incident ruby beam was simultaneously displayed in the first 12 windows of the video monitor. Then by adjusting optical paths for the reference and simulated scattering of the ruby light (after being attenuated)

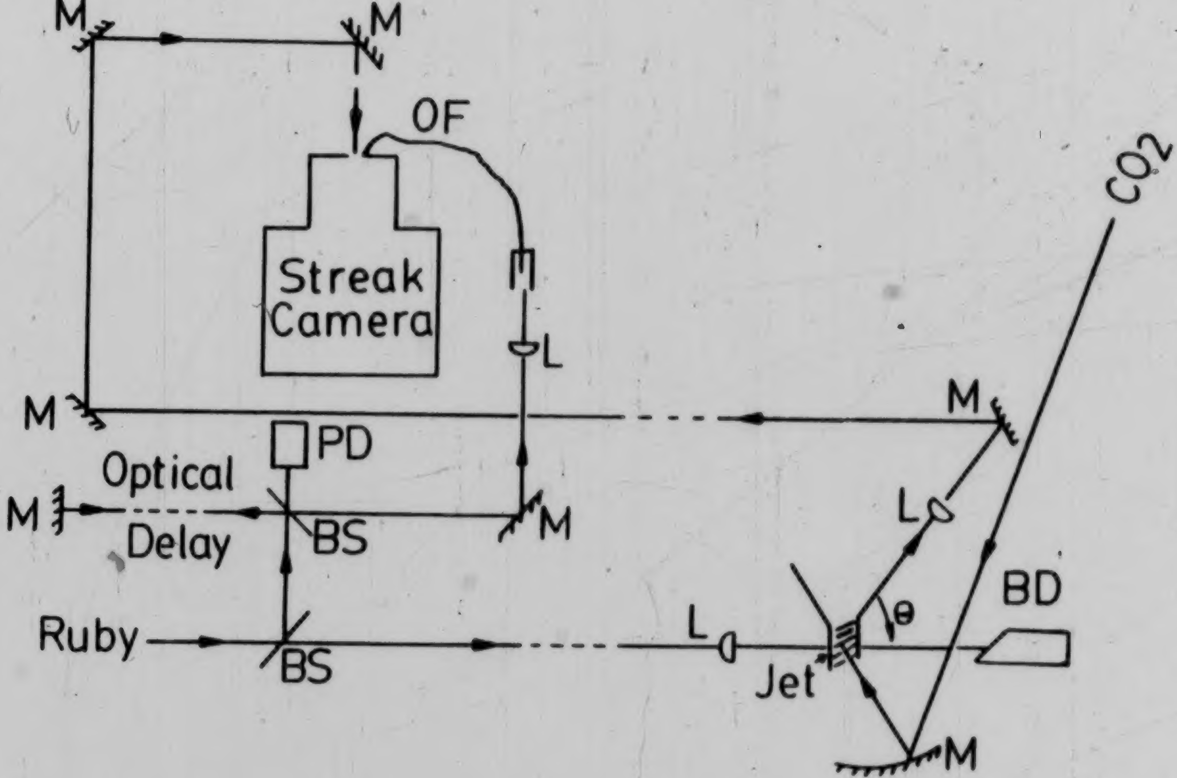
M
M
OF
Streak Camera
L
M
M
PD
Optical
Delay
M
BS
M
L
Ruby
BS
L
Jet
θ
BD
M
CO2

Fig. 3.14 Thomsson scattering experiment for $S(\overline{k})$ measurements. M: mirror, L: lens, BS: beam splitter, PD: photodiode, PM: photomultiplier.

from a microsphere positioned at the CO_2 laser beam focus, excellent timing was achieved.

CHAPTER 4

EXPERIMENTAL RESULTS AND DISCUSSION

4.1 Introduction

In this chapter the results of various laser plasma interaction experiments are presented. Plasma parameters such as electron temperature and density as well as the general behaviour of the laser plasma interaction are first discussed. In later sections the results of the Thomson scattering experiment are given.

Temporal characteristics of plasma formation are shown in Fig. 4.1. Figure 4.1a shows the CO_2 laser power transmitted (as collected with an f/2 lens and detected by a photon drag). It can be seen from the figure that gas breakdown occurs approximately 10-15 ns before the peak of incident CO_2 laser beam is reached. In the breakdown region the transmitted signal level approaches a noise level as a result of absorption and scattering. As can be seen in Fig. 4.1b the transient phase of stimulated Brillouin backscattering takes place only once in the laser plasma interaction. This happens ~ 4 ns after gas breakdown regardless of the fluctuation in the incident laser power. The measured SBS level was approximately 10% at an operating laser intensity of 5×10^{12} W/cm^2. In a time interval of ~ 10 ns following SBS, nearly complete absorption occurs. This is followed by target burn through and refraction domination (not seen in the figure because it takes place outside the focal cone of the

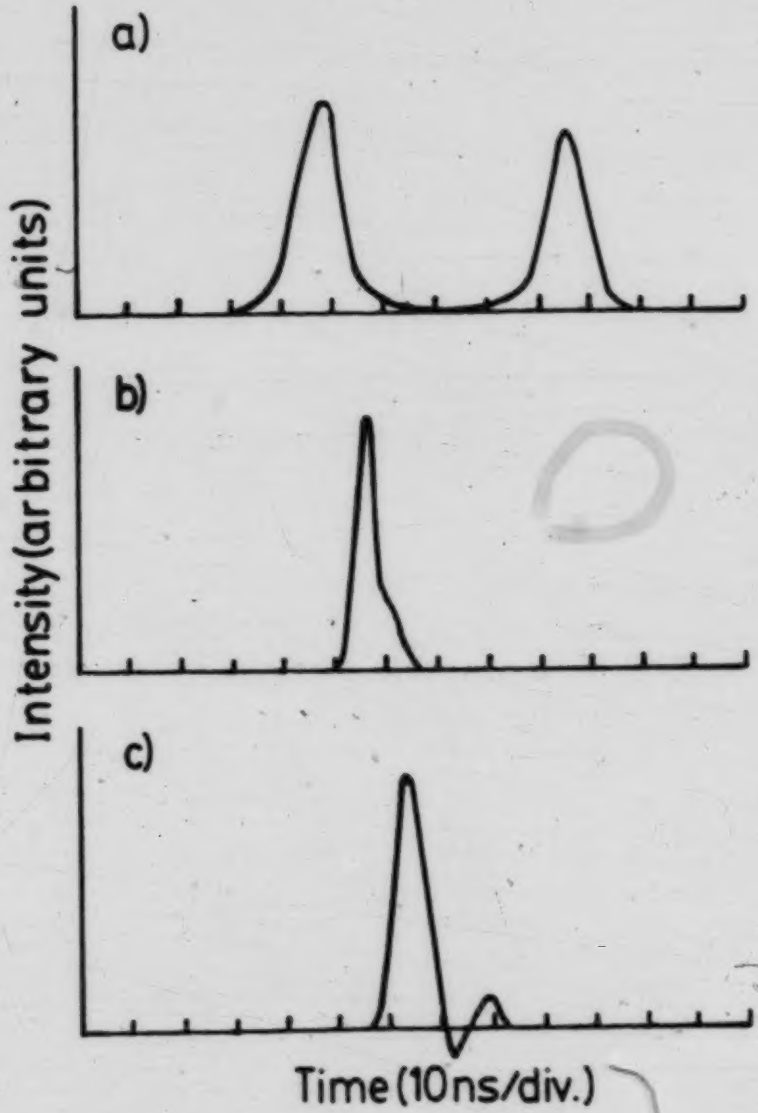

Fig. 4.1 General behaviour of the CO_2 laser plasma interaction;
a) Transmitted CO_2 laser signal, b) SBS signal,
c) Thomson scattering signal.

forward transmission). Throughout these experiments the SBS signal was used as a reference for timing purposes simply because of being strong, fast and well characterized (details of the SBS instability generated in the present experiment can be found in |1| and |2|). Finally, Fig. 4.1c shows a typical Thomson scattering signal from ion fluctuations (recorded by a photomultiplier), the characteristics of which will be discussed later in this chapter.

Results from x-ray measurements indicate a single electron temperature of 100 ± 20 eV (Fig. 3.2) at focused CO_2 laser intensity. This is quite different from those reported in |1| where two Maxwellian electron temperatures were identified at ∿ 160 eV and ∿ 1 keV. The absence of the hot electron component in the present experiment may be due to the many changes in laser plasma interaction conditions such as lower electron plasma density and reduced laser intensity level compared to the earlier work, though the precise reasons are not understood. The absence of the critical density layer (as will be seen later) eliminated the role of many mechanisms responsible for producing energetic electrons such as two stream instability and *e-i* decay instability at critical and resonance absorption.

Since the x-ray detection risetime was ∿ 3 ns, temporal evolution of the x-ray, emission could not be examined in detail. However, a pulse duration of < 20 ns was observed in all the x-ray measurements. This was much less than the CO_2 laser pulse duration and could be related to the low density plasma that results at a later time due to plasma expansion.

Direct measurement of ion temperature in this experiment was not possible. This is because Faraday cups and electrostatic ion analyzers require a low pressure environment ($< 10^{-4}$ torr) and therefore could not be used in our experiment since we were operating with a 10 torr helium background (necessary to stabilize the oxygen jet). Optical spectroscopy also was not possible since, for a high degree of ionization, most of the oxygen lines are in the x-ray region. Thomson scattering, on the other hand, would potentially be an excellent technique for measuring the ion temperature if scattering from thermal plasma fluctuations could be observed. But because the measured Thomson scattering spectra were dominated by enhanced scattering from nonthermal ion fluctations, isolation of the thermal component from the nonthermal one was again impossible. However, the ion temperature was roughly estimated from enhanced Thomson scattering of the nonthermal ion fluctuations as will be discussed later.

The other very important parameter to be determined accurately is the plasma electron density. Unfortunately, due to a number of changes in the operating conditions of the CO_2 laser plasma interaction, particularly focused laser conditions (a new focusing mirror with larger aberrations was used), different regimes were observed and therefore must be dealt with separately. Thus, according to the density regime prevailing during different periods in the thesis research, two cases will be considered for analysis (Case I and Case II).

In discussing the plasma density throughout these analyses, we will refer to Fig. 4.2 where a schematic diagram of the experiment is shown. In this figure it is assumed that the CO_2 laser light is

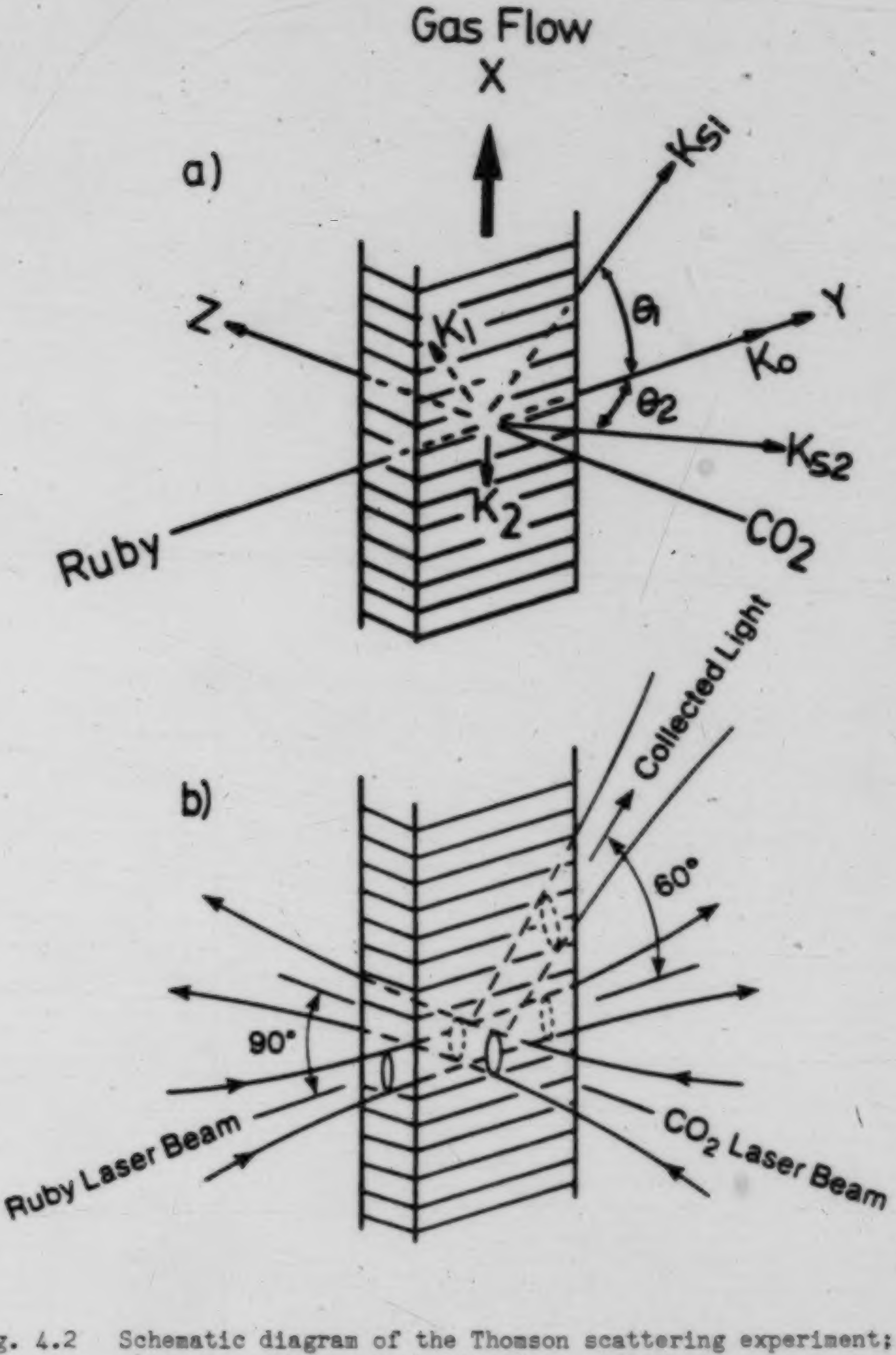
Gas Flow
X
a)
Ksl
Z
K1
θ1
Y
Ko
θ2
Ks2
K2
CO2
Ruby
b)
Collected Light
60°
90°
Ruby Laser Beam
CO2 Laser Beam

Fig. 4.2 Schematic diagram of the Thomson scattering experiment; a) Wave vectors at the incident, scattered and ion waves, b) Intersection of the CO_2 laser beam, ruby laser beam and the collected light.

propagating in the X-direction and the O_2 gas is flowing in the Y-direction. Because a symmetric CO_2 laser beam was used, the plasma density was assumed cylindrically symmetric (i.e., in the X-Y plane). The Abel transform could therefore be used to invert plasma interferograms in order to obtain the radial electron density profiles at different axial positions in the plasma. Following SBS, the highest density for both cases (I and II) is reached and maintained for a period of $\sim$ 8 ns. The density then decays due to hydrodynamic expansion.

Figures 4.3-4.5 illustrate the behaviour of the electron density in Case I. Figure 4.3 shows a typical unfolded interferogram of the plasma density $\sim$ 3 ns after the start of SBS. The radius of the plasma spot size at the leading edge is $\sim$ 100 μm. The radius then increases almost linearly with Z according to the relation $R = 100 + 0.5Z$ where both R and Z are in μm. As can be seen in the figure, the plasma density is maximum at $r = 0$ and then decays sharply towards zero at the plasma edge ($r = R$). Figure 4.4 shows the variation of the peak density ($r = 0$) with the axial distance Z. According to the figure, this variation is almost linear and the plasma density at the focal point is approximately equal to 0.8 n_c. In this early stage of the plasma formation, the plasma was found to extend $\sim$ 0.3 mm in the axial direction with a scale length $L = n\frac{dZ}{dn}$ of 200 ± 30 μm at the focal point. At a later time ($t > 8$ ns) the plasma density decreased and occupied a larger volume (Fig. 4.5) with $L \gtrsim 800$ μm and $n = 0.25$ n_c at the focal point.

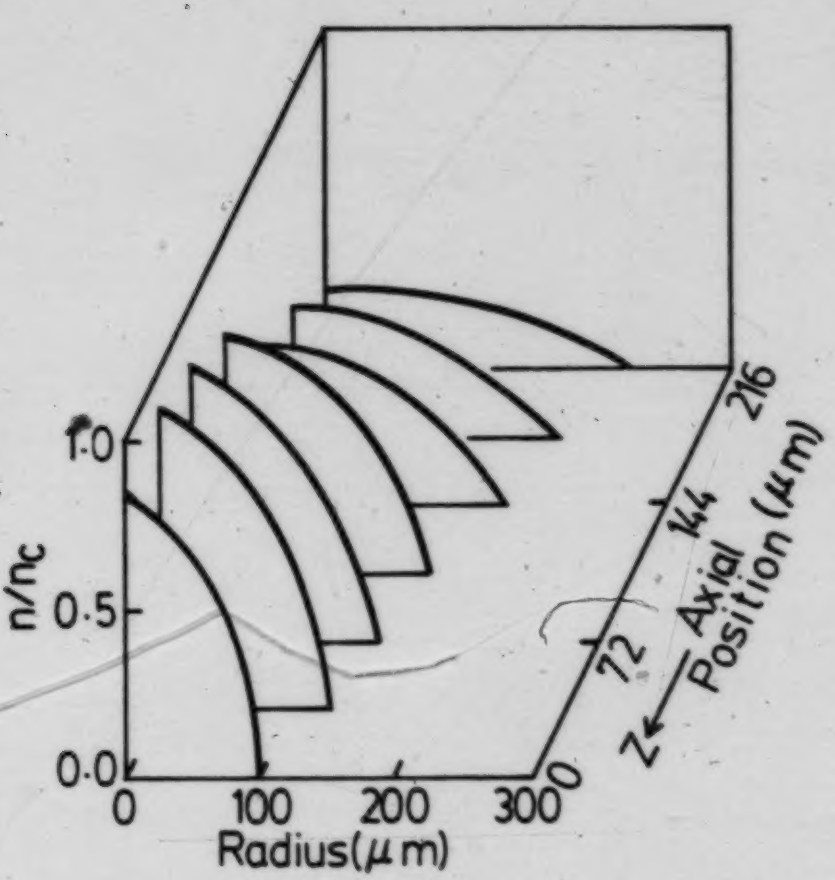

Fig. 4.3 Unfolded interferogram of the plasma density of Case I at ∿ 3 ns after the start of SBS.

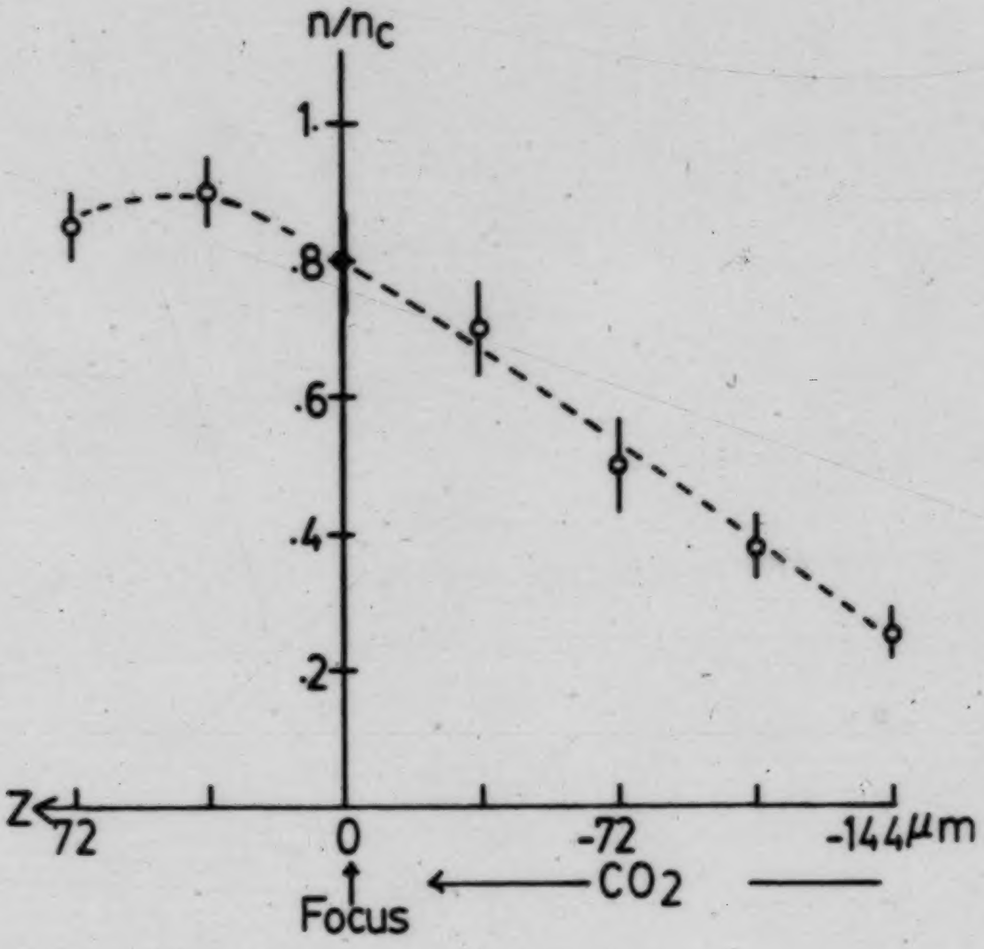

Fib. 4.4 Variation of the peak density (r=0) with the axial distance Z at ∿ 3 ns after the start of SBS for Case I.

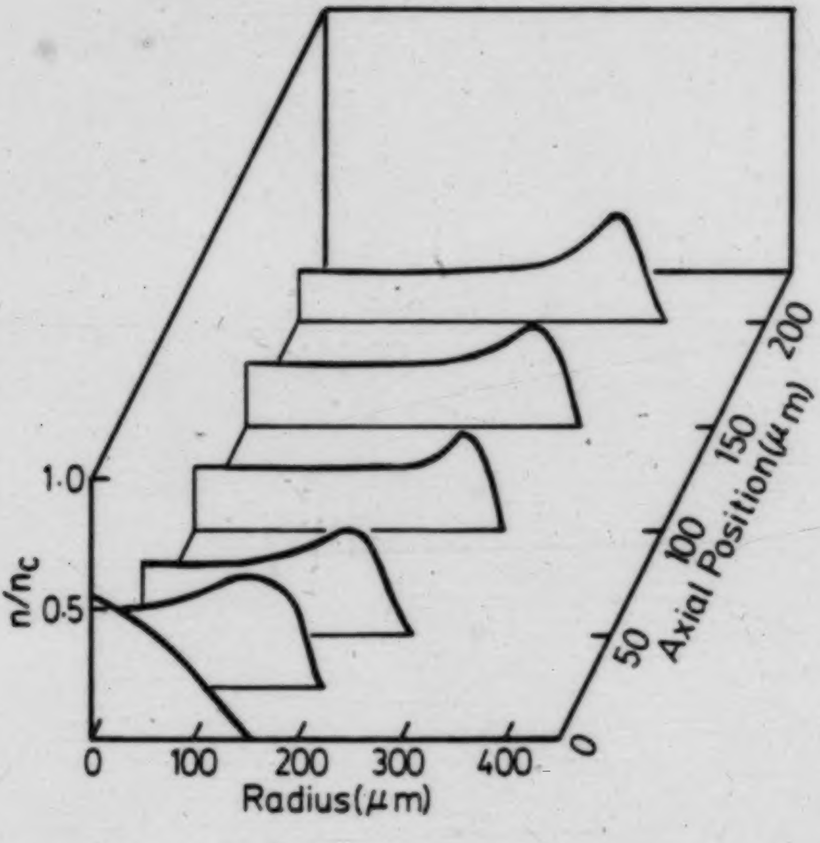

Fig. 4.5 Unfolded interferogram of the plasma density of Case I at ∿ 10 ns after the start of SBS.

Figures 4.6 and 4.7 show the measured plasma density profiles for Case II at a time 2 - 8 ns after the start of SBS. In comparison with the previous figures, it can be seen that the density is generally lower than in Case I ($\sim 0.7\ n_c$ at the focus) with larger axial extension (0.8 - 1 mm with $L = 450 \pm 50\ \mu m$). Similar behaviour to that shown in Fig. 4.5 (for Case I) was observed at a later time, $t > 8$ ns for Case II.

It should be mentioned that although the change in the focused laser conditions affected the plasma density, no significant change was seen in the electron plasma temperature (taking into account the 20% error associated with the x-ray results). The temporal evolution of the electron temperature might not have been identical for Case I and Case II, however, the time integrated x-ray measurements did not show any difference.

Thomson scattering results and ion turbulence measurements obtained in Case I will be presented in Section 4.2, while those results obtained in Case II will be discussed later in Section 4.3.

4.2 Ion Turbulence and Absorption

4.2.1 Laser light absorption in CO_2 laser plasma interaction.

It has been shown in an experiment very similar to the present one |1,3| that inverse bremsstrahlung absorption cannot fully account for the nominal 100% absorption observed. With a scale length as small as 100 μm and with the existence of a critical density layer the fraction of light which should be absorbed is only 40% (as calculated from Eqn. (2.10)), assuming a linear density profile. Similarly, we

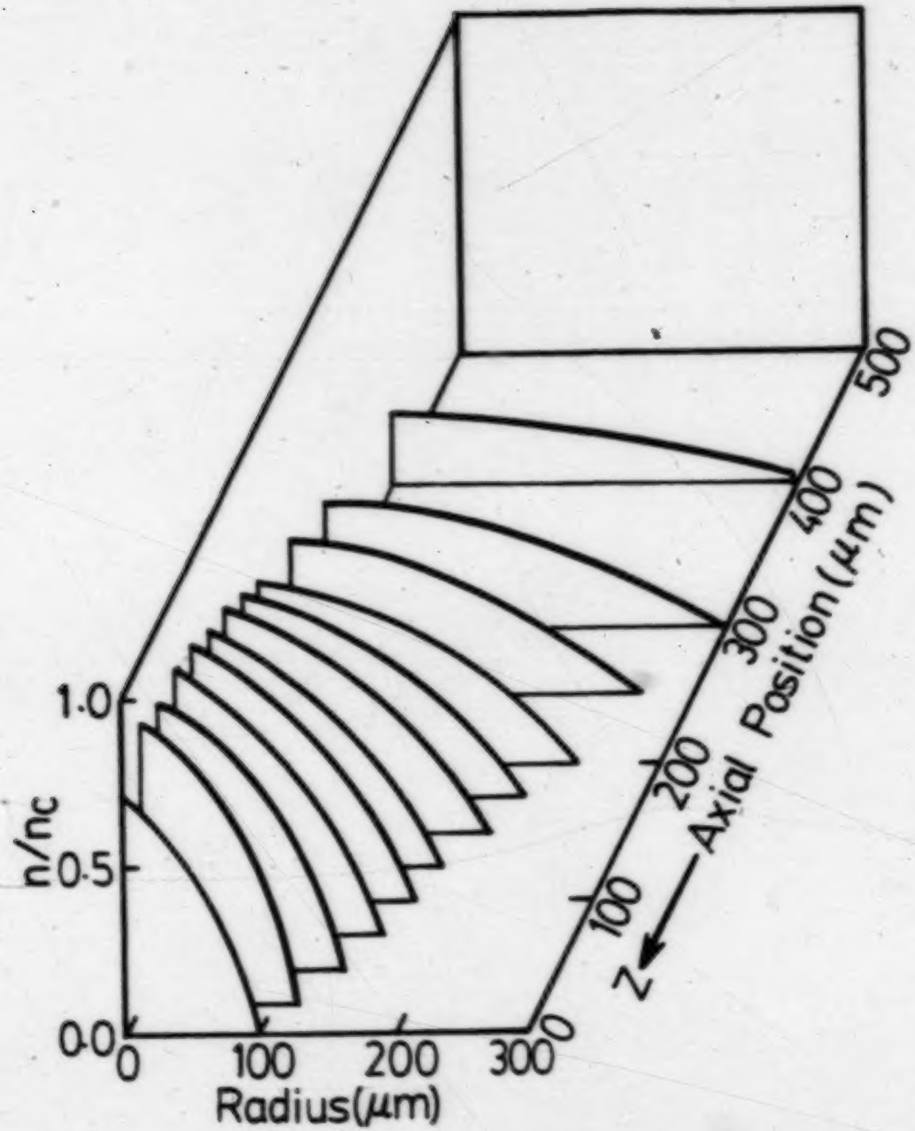

Fig. 4.6 Unfolded interferogram of the plasma density of Case II at ~ 3 ns after the start of SBS.

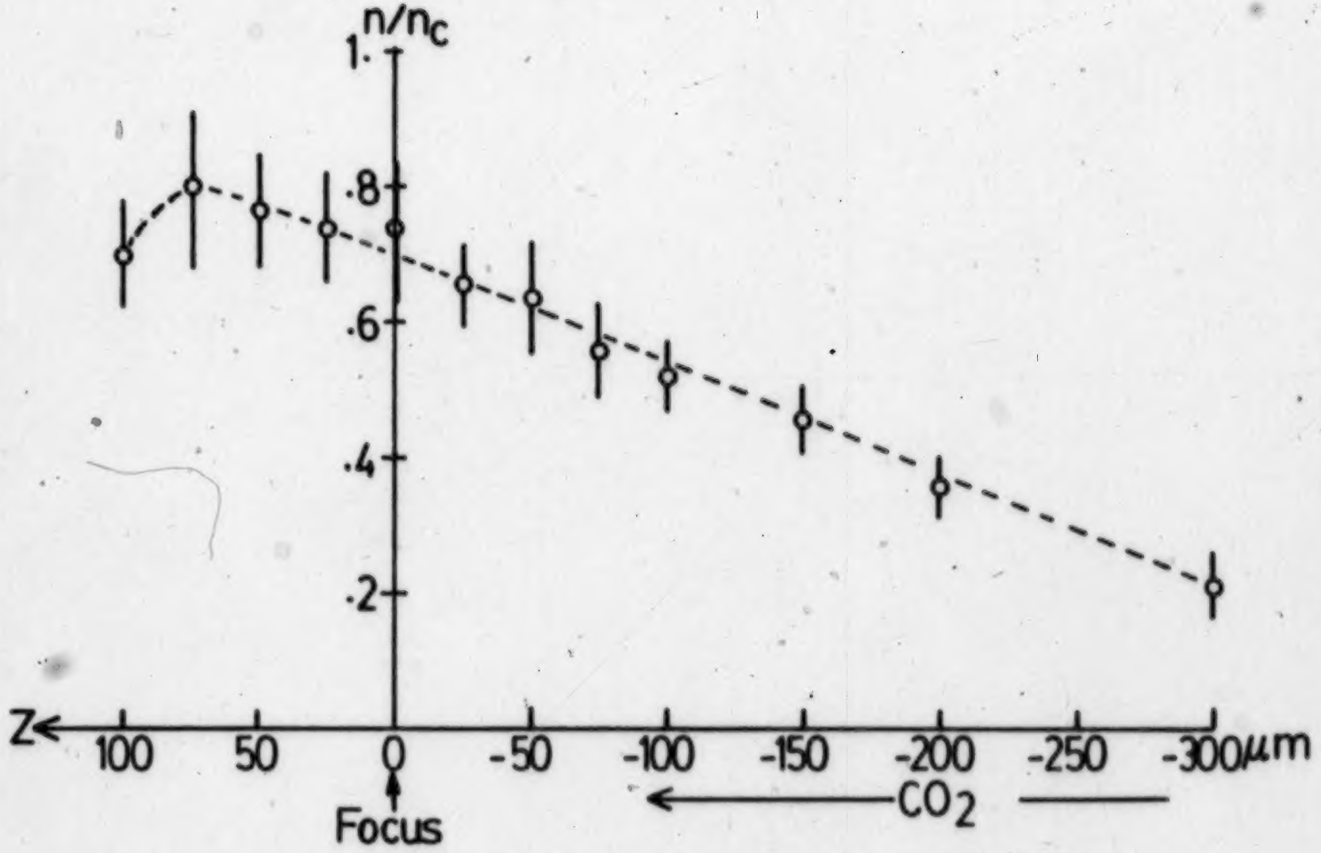

Fig. 4.7 Variation of the peak density (r=0) with the axial distance Z at ∿ 3 ns after the start of SBS for Case II.

can estimate the fraction of the incident light being absorbed by the inverse bremsstrahlung mechanism in the present experiment. Since Eqn. (2.10) is only valid for a linear density profile reaching critical density, it cannot be used to estimate the fraction of the absorbed light in the present experiment ($n < n_c$). However, the original formula of Dawson, *et al.* [4] can still be applied:

$$A = 1 - e^{-K_T}$$

$$K_T = \int_{-\infty}^{\infty} \frac{\nu_{ei}(Z)\omega_{pe}^2(Z)dZ}{c\omega_0|\omega_0^2 - \omega_{pe}^2(Z)|^{\frac{1}{2}}} \qquad (4.1)$$

By using the measured density profile (Fig. 4.4) and assuming a uniform plasma temperature over the entire region (with T_e = 100 eV), Eqn. (4.1) can then be integrated numerically to give an absorbed fraction $A \leq 0.7$. It should be noted, however, that in calculating the collision frequency ν_{ei}, the charge state was taken to be $Z = 6$ which is the maximum value estimated by comparing the neutral oxygen density and the maximum plasma density ($n = 0.9\ n_c$). This is consistent with the ionization state calculated for T_e = 100 eV [5]. Thus, the above calculated absorption fraction represents an upper limit. At a later time ($t > 8$ ns after the start of SBS) where the density is very low or for $Z < 6$ the absorption is even lower. Therefore, at least 30% of the incident light has to be absorbed by a mechanism or mechanisms other than inverse bremsstrahlung.

A variety of processes may account for the discrepancy between the observed and classical calculated absorption. Parametric processes are one possibility. Stimulated Brillouin scattering has the lowest threshold among the possible parametric instabilities. However, the SBS scattered power was not more than 10% of the incident power. Moreover, the anomalous absorption and SBS occurred at different times during the interaction (i.e., absorption follows SBS). Thus, while SBS can influence subsequent events by enhancing fluctuations, it cannot account directly for absorption.

The absence of the critical density and high energy electrons eliminate resonance absorption and absorption due to OTS and *e-i* decay instabilities (at critical density) as candidates for the observed absorption. Equally, the Raman instability cannot contribute to absorption in the present experiment because of its high threshold ($\gtrsim 10^{13}$W/cm^2). Moreover, it was sought for but was not detected experimentally.

Other parametric instabilities such as two-plasmon decay and off-resonance OTS and PD may contribute to absorption directly but in a very limited way because of relatively high thresholds (compared to SBS, e.g.). However, the OTS and PD off-resonance may contribute to absorption indirectly by generating ion turbulence which, in turn, can enhance the absorption as explained in Chapter 2. This mechanism will be discussed here in light of the experimental data.

4.2.2 Scattering parameters.

To study ion turbulence and its effect in laser light absorption, both spectral and temporal behaviour along with the turbulence level of the ion fluctuations were measured using ruby laser Thomson scattering techniques (described previously in Chapter 3). The scattered light was detected at an angle θ with respect to the incident ruby laser direction (Fig. 4.2a) either in the plane of the target ($\bar{k}_{s1}$ in the

X-Y plane) or in a plane defined by the ruby laser and CO_2 laser propagation directions ($\overline{k}_{s2}$ in the Y-Z plane). This probed the ion fluctuation wave vector $\overline{k}_1$ perpendicular to the CO_2 laser light wave vector (parallel to the unpolarized electric field of the CO_2 laser radiation, i.e., in the X-Y plane) and $\overline{k}_2$ in the Y-Z plane at an angle $90^\circ \pm \theta_2/2$ with the electric vector of the CO_2 laser light. Both $\overline{k}_1$ and $\overline{k}_2$ are related to the incident ruby laser wave vector $\overline{k}_0$ through the equation $\overline{k}_{1,2} = \overline{k}_{s1,2} - \overline{k}_0$ and the wave numbers are given by

$$k_{1,2} \simeq 2k_0 \sin \theta_{1,2}/2 = 1.81 \times 10^5 \sin \theta_{1,2}/2 \text{ cm}^{-1} . \qquad (4.2)$$

We will refer to these two cases (scattering in the X-Y and Y-Z planes) as Case a and Case b respectively.

If we realize that the plasma density varies from 0 - 0.9 n_c the range of $k\lambda_D$ will be very wide ($k\lambda_D \geq 0.224$ for $\theta = 60^\circ$, e.g.). However, the scattering volume was defined by the intersection of the focused ruby laser, the CO_2 laser, and the collecting optics (Fig. 4.2b) and was approximately $150 \times 150 \times 100\ \mu m^3$ around the laser focal point. Therefore, by referring to Figs. 4.3 to 4.5, the density of the probed plasma roughly ranged between 0.4 and 0.9 n_c. The corresponding $k\lambda_D$ and α (for $\theta = 60^\circ$) were $0.224 \leq k\lambda_D \leq 0.336$ and $3.0 \leq \alpha \leq 4.5$.

The scattered light was detected simultaneously with a photomultiplier for temporal behaviour and an optical multichannel analyzer-monochromator system for (time integrated) spectral measurements.

4.2.3 Temporal measurements of ion fluctuations.

The power of the scattering signal (recorded by the photomultiplier) was many orders of magnitude greater than that which would arise from scattering from thermal fluctuations. A simple calculation shows that refraction of a ruby laser beam caused by electron density gradients cannot account for the enhanced scattering at the observed angles. This is because the deflection angle is small compared to the scattering angles used (22°-90°). The deflection angle is given by |6|

$$\Delta\alpha = \int_0^L \left(\frac{1}{\mu}\right) \bar{\nabla}\mu \times d\bar{Z} \,, \qquad (4.3)$$

where the refractive index $\mu \simeq 1 - 2\pi n e^2/m\omega_0^2$ and ω_0 is the ruby laser light frequency. By approximating the density n by $0.9\, n_c\left(1 - \frac{Z}{0.3}\right)$, where Z is in mm, Eqn. (4.3) gives $\Delta\alpha \sim 10^{-3}$ rad ($= 0.057^\circ$). This indicates that simple refraction is not expected to be important and that the observed scattering is due to enhanced fluctuations. In addition, the fact that no electron features were observed (at large ω shifts such as the scattering theory predicts for $\alpha > 1$) demonstrates that the enhancement is most likely due to ion fluctuations. This will be discussed in more detail when spectral results are analyzed.

Temporal characteristics of the enhanced Thomson scattering in relation to the transmitted CO_2 laser radiation and strong stimulated Brillouin backscattering are shown in Fig. 4.1c. This time behaviour (although limited by the 3 ns photomultiplier risetime) is important in identifying (a) that the ion turbulence follows rather than occurs simultaneously with strong parametric interaction such as SBS, (b) that the duration of enhanced ion fluctuations ($\lesssim 10$ ns) is consistent with the observed period of anomalous absorption. The first observation clearly shows that while subsequent mode coupling or other plasma transport mechanisms may be responsible for ion turbulence, the fluctuations associated with the prompt SBS could not be directly responsible. Likewise, two-plasmon decay is coincident with SBS. Ruby laser scattering from ion fluctuations induced by SBS, however, did not show any time delay between the SBS signal and the Thomson scattering signal. These observations, together with the density measurements discussed before, indicate that enhanced ion fluctuations were generated in a relatively high density plasma. This is supported by the fact that, on average, the strongest scattering signal was observed only when the peak of the incident ruby laser took place within 10 ns of the start of SBS.

Scattering in the X-Y plane (Case a) and in the Y-Z plane (Case b) showed similar behaviour for a 60° scattering angle. The same characteristics were also observed for other angles, e.g. 22° in Case a and 90° in Case b. Details of the temporal structure of the ion fluctuations could not be obtained because of the limited resolution of the photomultiplier. Better information of the fine structure of the ion turbulence was obtained by employing a streak camera; the results will be discussed in Section 4.3.

4.2.4 Spectral measurements.

The main goal of the spectral measurements was to identify the source of the enhanced scattering. In the case of thermal plasma the spectra (theoretical) of the scattered light $S(k,\omega)$ for $\theta = 60^{\circ}$ are shown in Figs. 4.8 and 4.9 for $n = 0.8\ n_c$ and $n = 0.4\ n_c$ respectively (for $T_i = T_e = 100$ eV). As can be seen, the central region of each spectrum consists of an ion feature (solid) and an electron feature (dashed), the intensity of the ion component being approximately an order of magnitude higher than that of the electron. In addition, the electron component has two side components located at wavelengths $\Delta\lambda$, where $\Delta\lambda$ is given by

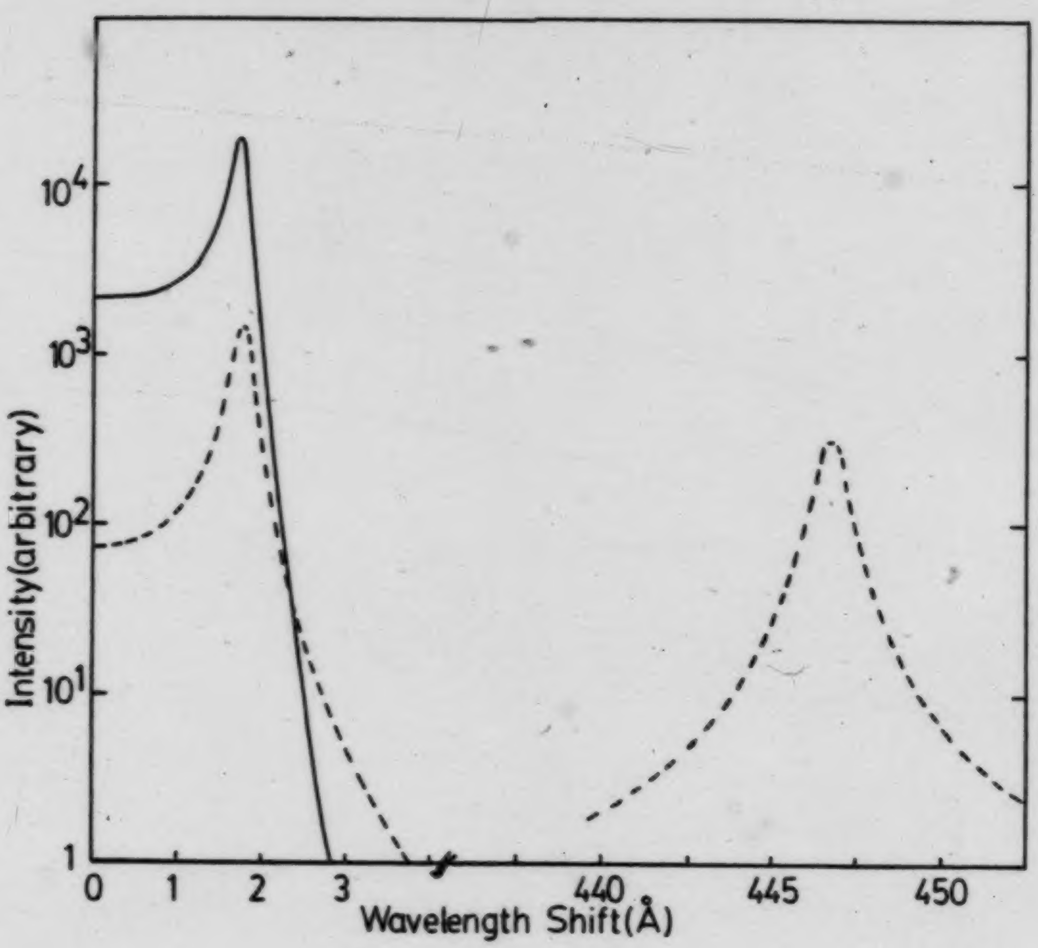

Fig. 4.8 Calculated ruby Thomson scattering spectrum for a thermal oxygen plasma with $T_i = T_e = 100$ eV, $n = 0.8\ n_c$, $z = 6$ and $\theta = 60^{\circ}$ showing the ion component (solid) and the electron component (dashed).

2.

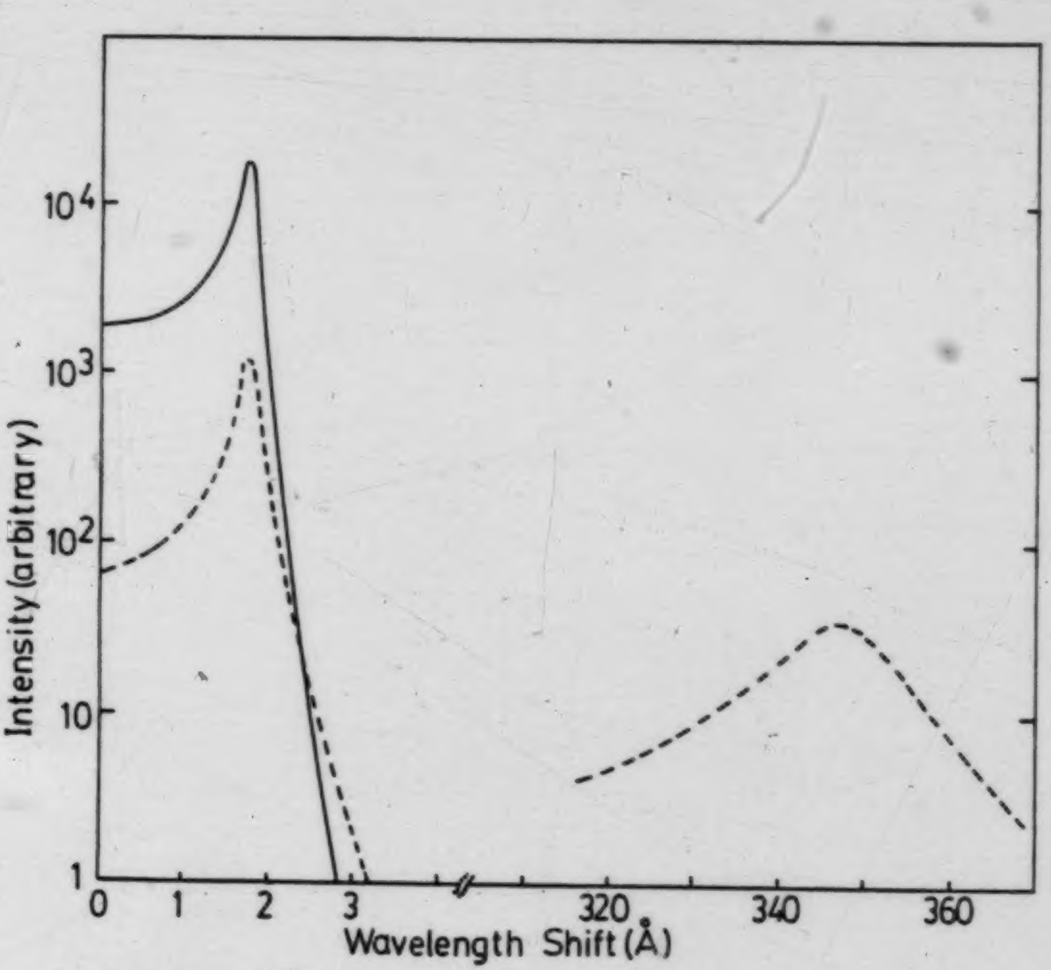

Fig. 4.9 Calculated ruby Thomson scattering spectrum for a thermal oxygen plasma with $T_i = T_e = 100$ eV, $n = 0.4\ n_c$, $z = 6$ and $\theta = 60^\circ$ showing the ion component (solid) and the electron component (dashed).

$$\Delta\lambda = \lambda_0 \pm \frac{\lambda_0}{\omega_0} \Delta\omega \ , \tag{4.4}$$

in which λ_0 and ω_0 are the ruby laser wavelength and frequency respectively and $\Delta\omega$ is the frequency of the electron plasma waves determined approximately from the Bohm-Gross dispersion relation

$$\Delta\omega^2 \simeq \omega_{pe}^2 (1 + 3k^2 \lambda_D^2) \ . \tag{4.5}$$

Experimentally, only the central parts of the scattered spectra were observed. Attempts were made to observe any electron plasma wave components by scanning over ±600 Å around λ_0 (corresponding to $n \leq 1.5\ n_c$) but were not successful. This indicated that there was no significant enhancement in the electron feature and that the observed scattering was mainly due to strong ion fluctuations. For nearly thermal plasma the electron wave feature, of course, is very weak for the values of $k\lambda_D$ experimentally probed and will therefore be buried in the bremsstrahlung radiation.

Comparison of Figs. 4.8 and 4.9 shows that due to the relatively small change in the plasma density, only the side components of the electron feature change materially (location and shape). The shape of the ion component, on the other hand, varies significantly with ion temperature and degree of ionization z as shown in Fig. 4.10 (for $n = 0.8\ n_c$ and $T_e = 100$ eV oxygen plasma).

Since the measured spectra correspond to time-integrated scattering, precise structure is lacking because of frequency smearing effects associated with time varying plasma conditions. Nevertheless, considerable information can be obtained from these spectra. Spectral measurements of the scattered ruby light are summarized in Fig. 4.11

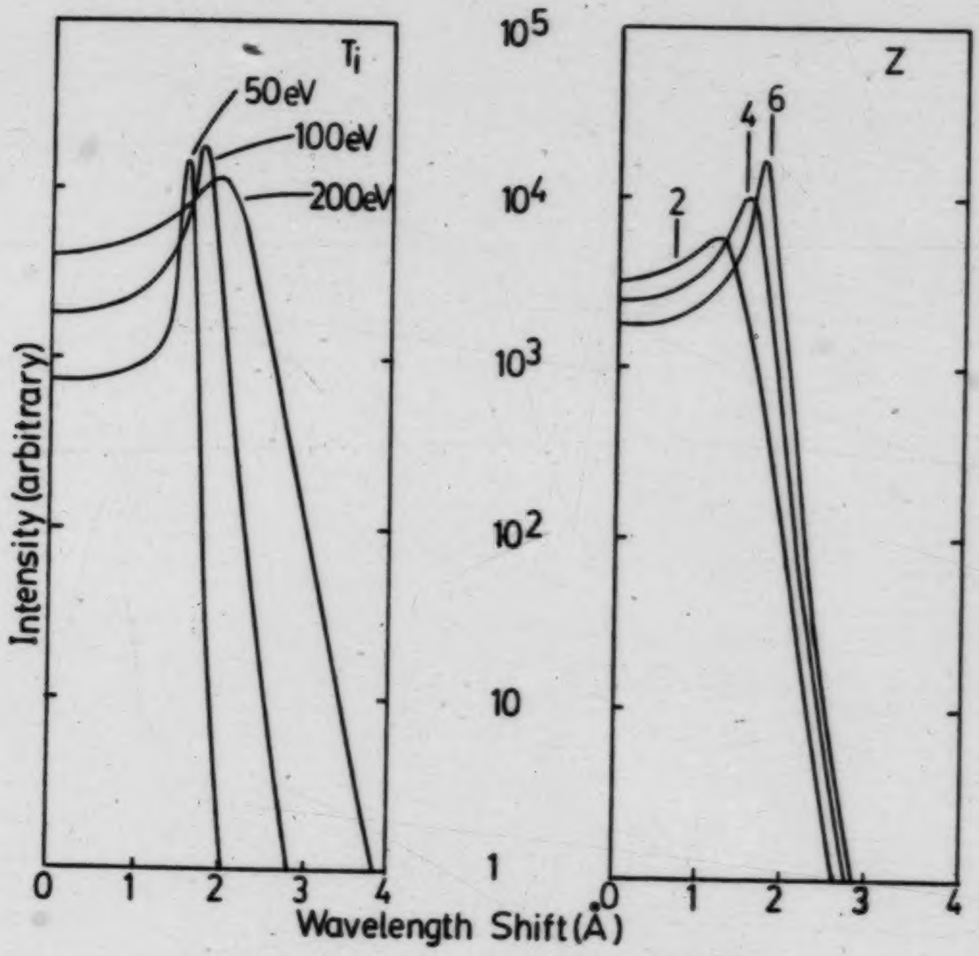

Fig. 4.10 Variation of the ion component (of the ruby Thomson scattering spectrum) with ion temperature and degree of ionization for a thermal oxygen plasma with T_e = 100 eV, $n = 0.8\ n_c$ and $\theta = 60^{\circ}$.

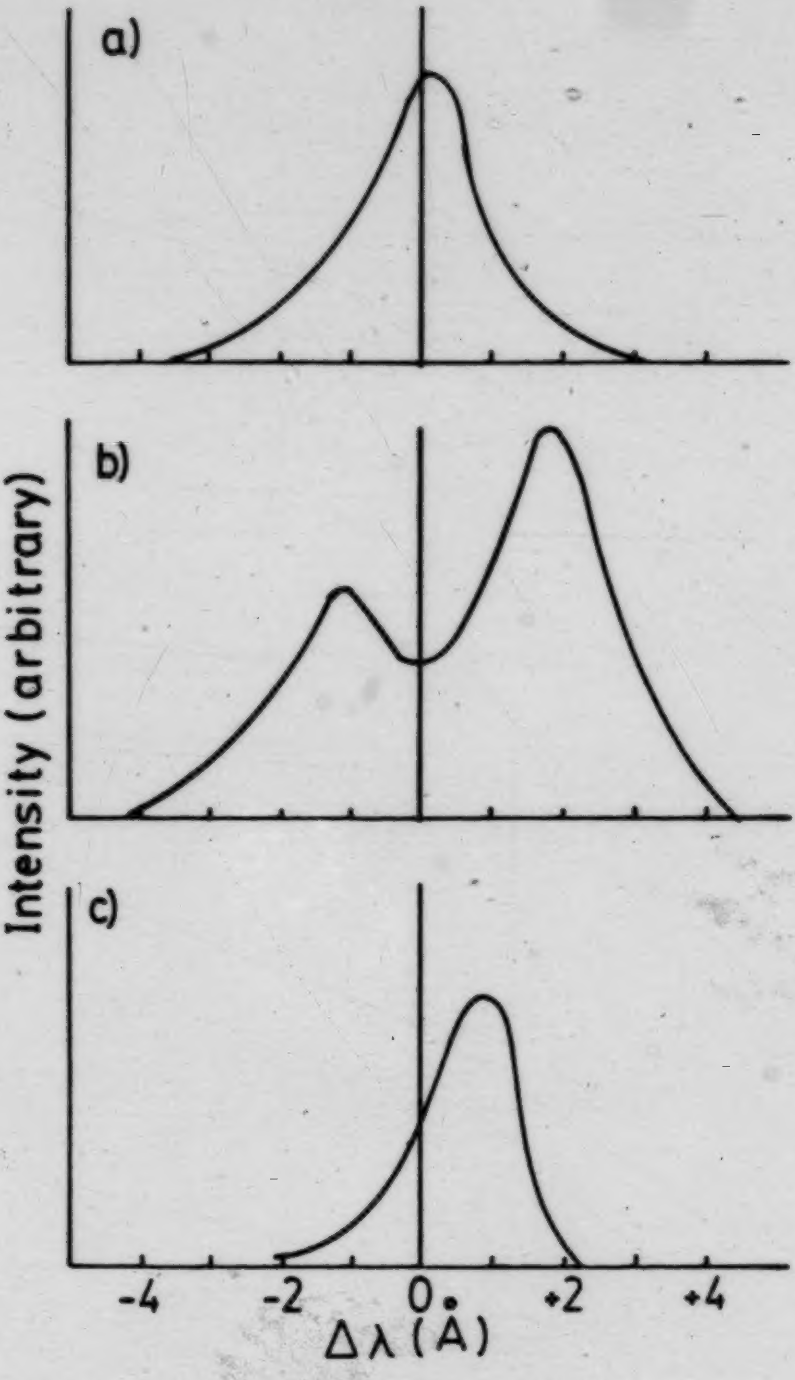

Fig. 4.11 Spectra of scattered ruby laser light for $\theta = 60^\circ$ showing a) and b) unshifted typical spectra (for scattering in the X-Y plane), c) shifted spectrum for scattering in the Z-Y plane.

for $\theta = 60^\circ$. The upper two spectra (Case a) show a symmetric behaviour with respect to λ_0 , i.e., no discernable Doppler shift due to a superimposed plasma drift. This is most likely expected for ion waves $(\overline{k}_1,\omega)$ propagating perpendicular to the CO_2 laser beam. Moreover, the lower spectrum (Case b) shows a distinct red shift for the case of $\overline{k}_2$ lying in the plane containing the incident CO_2 and the ruby laser beams (Fig. 4.2a). The magnitude and direction of this shift $\Delta\lambda/\lambda_0 = -\Delta\omega/\omega_0 = -(\overline{k}_2,\overline{u})/\omega_0$ implies a motion $\overline{u}$ in the direction of propagation of the incident CO_2 laser beam of magnitude $u \simeq 5 \times 10^6$ cm/sec. It should be pointed out that Fig. 4.11c shows an extreme case for the maximum shift observed. Results such as those seen in Fig. 4.11a and 4.11b were observed frequently for Case b as well as Case a. The detailed behaviour depended on the statistical variation of the plasma conditions and on the timing between the CO_2 and ruby laser beams.

If we assume that the peak of the enhanced ion spectrum is unchanged from that of a thermal plasma, then we may calculate T_i from the following equation |7|,

$$T_i = \left\{77.63\left(\frac{\Delta\lambda}{\sin\theta/2}\right)^2 - zT_e\right\}/3 \; . \qquad (4.6)$$

In this case, the peak of the scattered spectrum for Fig. 4.11b at $\Delta\lambda \simeq 1.7$ Å corresponds to an ion temperature $T_i \simeq 100$ eV (for T_e = 100 eV, $\theta = 60^\circ$ and $z = 6$). Similar results were obtained for other angles, e.g., $\theta = 22^\circ$ and are shown in Fig. 4.12 (in which $\Delta\lambda \simeq 0.7$ Å). The average temperature obtained from different spectra was $T_i = 100 \pm 50$ eV. This temperature, as indicated before, has been inferred for ions that are a small percentage of the total ions; i.e., those which

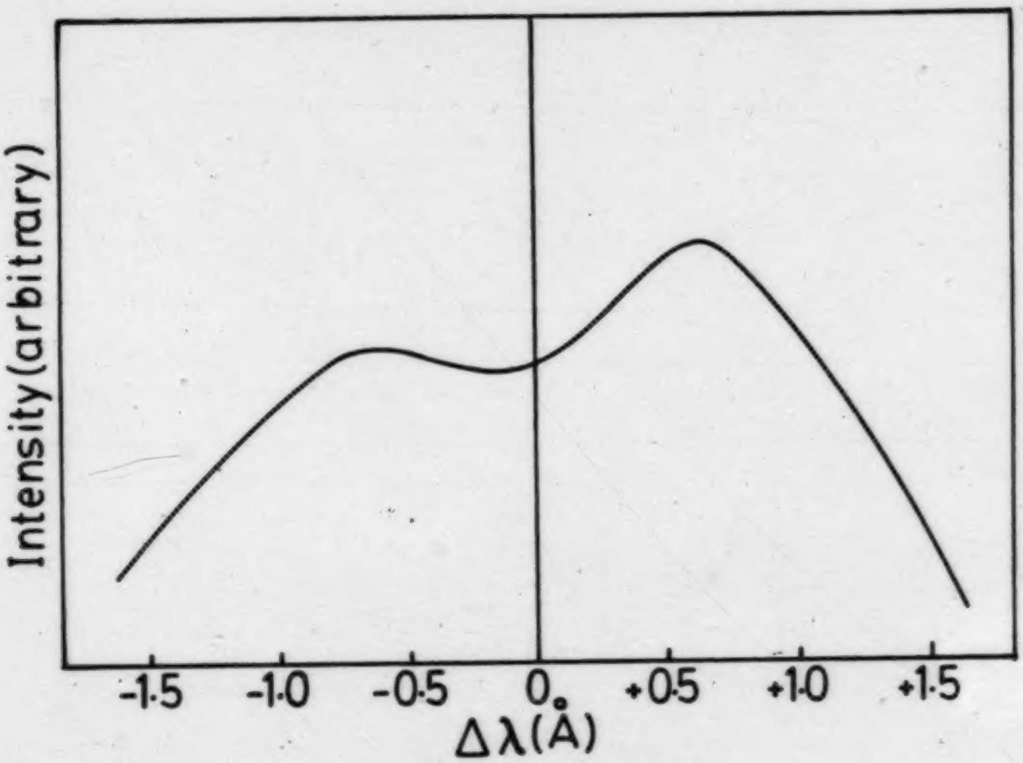

Fig. 4.12 Spectrum of the scattered ruby laser light for $\theta = 22^\circ$ in the X-Y plane.

cause the enhanced scattering. It should be noted, however, that it is reasonable to assume that the background (bulk) ions have ∿ 100 eV temperature as well for two reasons: 1) Even without taking into consideration the heating effect due to parametric instabilities, hydrodynamic calculations of the laser heated gas target experiment give an average ion temperature of not less than 50% of electron temperature, |8| ($T_i \gtrsim 50$ eV in this experiment) and 2) The time required for the ions (nonthermal) to relax to a Maxwellian distribution of thermal temperature $T_i = 100$ eV using the formula given in |9| is ∿ 0.4 ns which is very short compared to the total enhanced fluctuation time observed, at least in this part of the experiment (Case I).

The other information which can be deduced from the shift in wavelength of the ion feature is the ion wave frequency. Simple calculations from Figs. 4.11b and 4.12 give $\omega = 5.6 \times 10^{11}$ and $2.4 \times 10^{11}\,\text{sec}^{-1}$ for $\theta = 60^\circ$ and 22° respectively. These same calculations, when made using the ion wave dispersion relation

$$\omega = \frac{\omega_{pi} \cdot k\lambda_D}{(1 + k^2\lambda_D^2)^{\frac{1}{2}}}\,, \tag{4.7}$$

give $\omega = 5.3 \times 10^{11}$ and $2.1 \times 10^{11}\,\text{sec}^{-1}$ (where $\omega_{pi} \sim 2.3 \times 10^{12}\,\text{sec}^{-1}$ for $n = 0.8\,n_c$). These values agree well with the experimental calculations.

In addition, from the spectral width ($\Delta\lambda = 1.5$ Å) of Figs. 4.11a and 4.11c one can estimate an ion wave damping rate of $\sim 3 \times 10^{11}\,\text{sec}^{-1}$ which implies a mode lifetime of ∿ 8 ps. Numerical simulations of current driven ion turbulence |10| show that enhanced ion fluctuations rapidly build up and decay, accompanied by electron heating, ion tail formation, and Landau damping of the instability.

Thus, if quasilinear effects (rather than nonlinear effects) are important in stabilizing the ion instability (regardless of how the instability is produced) in this experiment, many periods of growth and decay of ion fluctuations are occurring, as is indeed inferred from the short mode lifetime.

4.2.5 Ion fluctuation level.

The study of ion fluctuations produced by a laser beam is important because such fluctuations can affect energy absorption (discussed in Chapter 3) and transport processes |11,12| in the plasma. The presence of large amplitude ion fluctuations near critical density has often been invoked as a source of anomalous resistivity in order to explain the strongly reduced thermal conductivity seen in laser heated plasma experiments |13|. Therefore, many experiments have been made to measure the ion fluctuation levels. The first Thomson scattering measurements of ion turbulence in a high intensity laser heated hydrogen plasma target were reported by Offenberger *et al.* |14| where enhancement of $\sim 10^4$ over the thermal level was observed for $k\lambda_D \simeq 0.5$. Similar measurements have been carried out on oxygen |3| and carbon |15| plasmas in the presence of a critical density layer. In both experiments substantial enhancement over the thermal level was observed.

In the present experiment the main goal was to study the effect of ion turbulence on absorption of laser radiation in underdense plasma ($n < n_c$). Because it has already been established that the observed enhanced scattering is due to enhanced ion fluctuations, the turbulence level has to be determined in order to estimate the amount of absorption that enhanced ion fluctuations can contribute.

The density fluctuation level was determined from the absolute measurements of $S(k)$ which is related to the scattered power, P_s, through Eqn. (3-25). The absolute value of P_s was obtained by calibrating the photomultiplier detection system with a tungsten filament blackbody source positioned at the point where the CO_2 laser beam is focused. Light from the filament was collected through the same optics used for collecting the scattered light from the plasma. The blackbody light power P reaching the photomultiplier is given by |16|

$$P = \frac{2hc^2}{\lambda^5} \frac{\varepsilon A}{\exp(hc/kT\lambda)-1} d\lambda d\Omega \,, \tag{4.8}$$

where A is the emitting area, ε is the emissivity of the filament (= 0.43 for tungsten at 6943 Å and ∿ 1700° K), $d\Omega$ is the collection solid angle and $d\lambda$ is the detection bandwidth (defined by the bandwidth of the interference filter in front of the photomultiplier). The absolute value of both P_s and $S(k)$ were determined by comparing the scattered signal with the signal generated by the tungsten filament. The error associated with $S(k)$, due to the uncertainty in determining parameters relating P_s to $S(k)$, as discussed in Chapter 3, was ∿ 26% (uncertainty in I_0, n, v and $\Delta\Omega$ were ∿ 5%, 15%, 5% and 1% respectively).

The scattering form factor $S(k)$ calculated for a measured CO_2 laser intensity $I \sim 5 \times 10^{12}$ W/cm^2 and assumed $T_e = 100$ eV and $n = 0.8\, n_c$ (taking the density at the focal point as the average density), is shown in Fig. 4.13 as a function of k for $\theta = 22^\circ$, 60° and 90°. The scattering at $\theta = 60^\circ$ shows almost equal $S(k)$ values for both the X-Y and the Z-Y planes (Case a and Case b). The $S(k)$ value for $\theta = 60^\circ$ is $\sim 6.8 \times 10^2$ which is approximately 10^3 times the thermal scattering form factor $S_{Th}(k)$. The $S(k)$ measurements for $\theta = 22^\circ$ and $\theta = 90^\circ$ were made in the Z-Y and X-Y planes respectively for convenience. It should be pointed out that the observed $S(k)$ spectrum is not a Kadomtsev like spectrum (shown **dashed** in Fig. 4.13 as normalized to $S(k)$ at $\theta = 60^{\circ}$) which is theoretically predicted for current driven ion turbulence |17|.

The corresponding average spatial ion fluctuation level was calculated from a numerical integration of Eqn. (3.25) over k space using a second degree polynomial of the form

$$\ln S_i(k\lambda_D) = 10.89 - 22.14(k\lambda_D) + 15.9(k\lambda_D)$$

to represent the $S_i(k)$ spectrum given in Fig. 4.13. The result of this integration gave a value of $(\frac{\delta n}{n}) \simeq 0.036$. Although this fluctuation level is lower than the one reported previously in a similar experiment |3| it is still very high. This may be due to the changes in focused laser conditions and plasma parameters such as T_e, n (lower in this experiment), L and/or the absence of the critical density layer. If the reduction in $(\delta n/n)$ is due to a change in plasma density then this would indicate that the instability (responsible for generating the ion turbulence) favours high plasma densities. This is expected for the off-resonance OTS and PD instabilities discussed in Chapter 3.

To calculate the effective collision frequency ν_{eff} required to determine the enhanced absorption, we assume a broad isotropic turbulence spectrum (as indicated experimentally). The calculation then gives $\sum_{ki} \left(\frac{\delta n_{ki}}{n_c}\right)^2 \simeq 0.05$ where from Eqn. (2.19) we get

$$\nu_{eff} \simeq \frac{\omega_0}{4} < \mathrm{Im}\frac{1}{\varepsilon(k,\omega)} > \sum_{ki} \left(\frac{\delta n_{ki}}{n_c}\right)^2 , \qquad (4.9)$$

gives $\nu_{eff} \simeq 4.7 \times 10^{12} \sec^{-1}$, using Fig. 2.16 for the value of

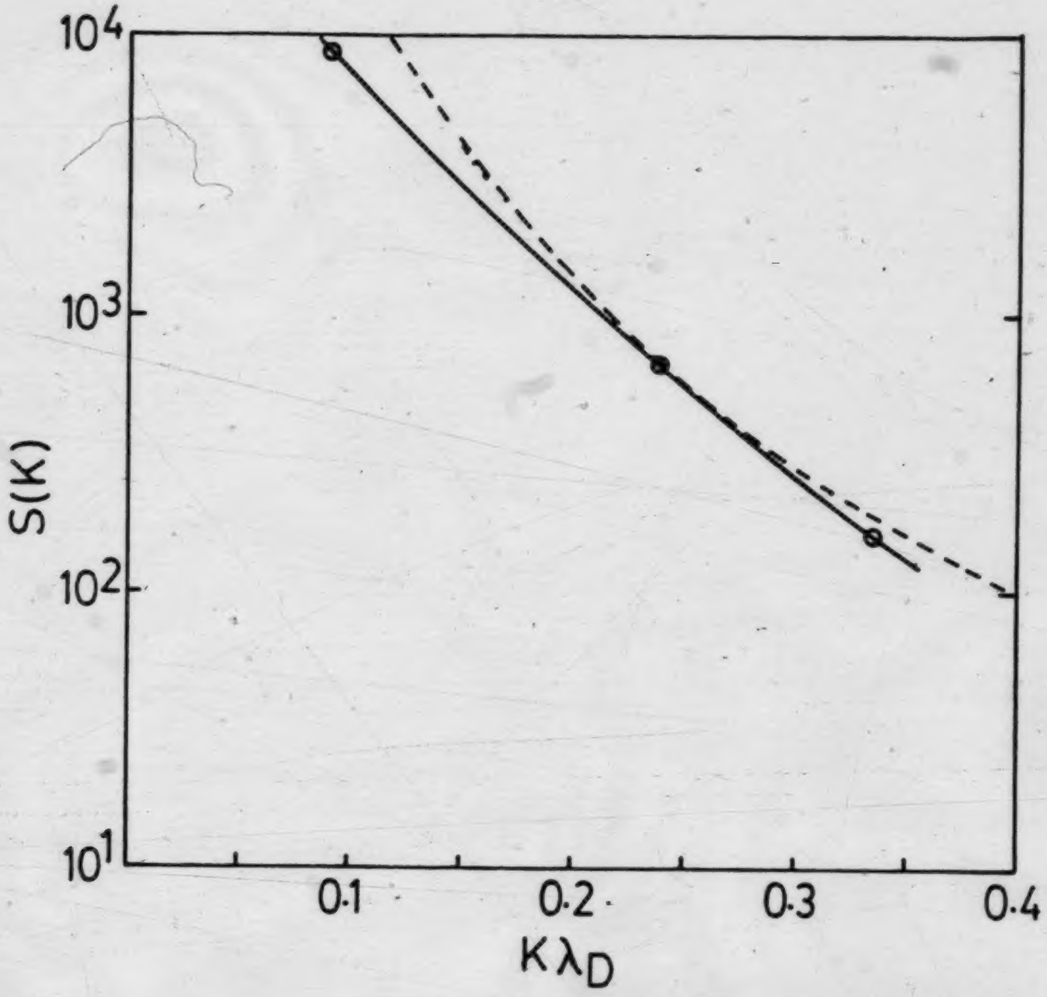

Fig. 4.13 Ion turbulence spectrum $S(k)$ as a function of $k\lambda_D$ assuming an average density $n = 0.8\ n_c$ and $T_e = 100$ eV (Case I). The Kadomtsev type spectrum is also shown (dashed).

$\langle \mathrm{Im}\frac{1}{\varepsilon(k,\omega)}\rangle$. In comparison, this frequency is approximately 3.6 times the classical collision frequency and it is more than enough to account for the remaining 30% absorption factor.

In summary, the ruby laser Thomson scattering measurements which probed directly the ion fluctuations for $k\lambda_D = 0.091$, 0.238 and 0.336, corresponding to scattering angles $\theta = 22^\circ$, 60° and 90° respectively (assuming $n = 0.8\, n_c$), confirmed three important turbulence related points; (a) spectrally resolved measurements showed the enhanced ion feature, (b) temporally resolved measurements showed enhanced fluctuations for $t \lesssim 10$ ns, consistent with the period of strong absorption, and (c) measurements of the scattering form factor $S(k)$ showed that the enhancement in ion density fluctuations could account for the anomalous absorption observed. In addition, it was shown that the turbulence levels for $k\lambda_D = 0.238$ ($\theta=60^\circ$) in and out of the plane of the target are almost equal, indicating an isotropic turbulence.

Discussion of the source of the ion turbulence is delayed to the next section where further experimental information will be provided.

4.3 Results of Case II

4.3.1 Introductory remarks.

The results presented here belong to the second regime of the experiment in which the plasma density is lower and the density scale length ($\sim 450 \pm 50$ μm at the focal point) is larger than that observed in Case I. Spectral analysis of the ruby laser Thomson scattering measurements showed unequivocal enhanced ion features. Some of the characteristics of the plasma in Case I were also seen here, particularly those shown in Fig. 4.1. The fraction of light which should be absorbed, as given by Eqn. (4.1), is ∿ 85% assuming the density profile of Fig. 4.7. Thus, ion turbulence need only to contribute 15% of the total to account for full laser absorption in this case.

More importantly, **ion turbulence generated in laser plasma experiments has not been systematically investigated. It** was, therefore, the aim of this experiment to study comprehensively the characteristics of the ion fluctuations, particularly those propagating in the direction of the electric field of the CO_2 laser radiation (in the *X-Y* plane). These fluctuations are potentially important for laser light absorption by plasmas ($\cos\theta = 1$ in Eqn. (2.17)). Section 4.3.2 will present the results of the $S(k)$ measurements. Section 4.3.3 will discuss the results of the streak camera measurements. Finally, the possible mechanism or mechanisms for generating ion turbulence in this experiment will be discussed in Section 4.3.4.

It should be noticed that the average plasma density throughout this part of the experiment will be taken as being equal to the density at the point where the CO_2 beam is focused, which prevails for $t \simeq 2 - 8$ ns after the start of the SBS (i.e., $n = 0.7\, n_c$). The electron temperature and the ionization state will be taken as 100 eV and 6 respectively.

4.3.2 $S(k)$ measurements.

The principal experimental result in this section is the determination of the $S(k)$ spectrum. The time integrated $S(k)$ was measured by a photomultiplier for six scattering angles ($\theta = 10^\circ, 16^\circ, 30^\circ, 45^\circ, 60^\circ$ and 90°) in the *X-Y* plane (Fig. 4.2). Thus, the wave number of the scanned ion fluctuations was in the range $1.6 \times 10^4 \text{cm}^{-1} \leq k \leq 1.3 \times$

$10^5 \mathrm{cm}^{-1}$ or $0.045 \leq k\lambda_D \leq 0.36$ $(2.8 \leq \alpha \leq 22.2)$ assuming $n = 0.7\, n_c$.

Figure 4.14 shows the experimentally derived $S(k)$ as a function of $k\lambda_D$ for ion fluctuations in the *X-Y* plane. As will be seen in the following section, there is considerable modulation in the structure of the scattered light; consequently, peak fluctuation levels can be substantially higher than the average values shown. In the region $k\lambda_D < 0.2$, $S(k)$ is strongly dependent on k (almost exponentially); however, for larger values of $k\lambda_D$ it varies more slowly. Over the experimental range of $k\lambda_D$, the time-integrated turbulence level varies from as little as 2 to $\approx 10^4$ times the thermal fluctuation level. It should be pointed out that, in general, this level is almost an order of magnitude below the previously reported value (Case I), probably due to a number of changes in the operating conditions of the CO_2 laser plasma interaction, particularly, focused laser conditions and the resultant change in the plasma density. This again illustrates the plasma density dependence of the ion wave instability generating the ion turbulence. It is apparent that no cutoff in the small $k\lambda_D$ region - such as that predicted for current driven ion instability and seen experimentally |18| - is found (at least for $0.045 \leq k\lambda_D \leq 0.36$).

We were unable to measure $S(k)$ in the *X-Y* plane for $\theta > 90^\circ$ because of geometrical limitations that resulted in overlapping of the focusing and collecting optics. However, no enhanced scattering over that expected from thermal fluctuations was seen for $\theta = 120^\circ$ $(k\lambda_D \approx 0.44)$ in the *Y-Z* plane. Furthermore, no change in the turbulence level was observed as we changed the direction of observation from the *X-Y* plane to the *Y-Z* plane for $\theta = 45^\circ$ and 60°. This suggests an approximately isotropic spectrum. Moreover, we probed the $S(k)$ of the

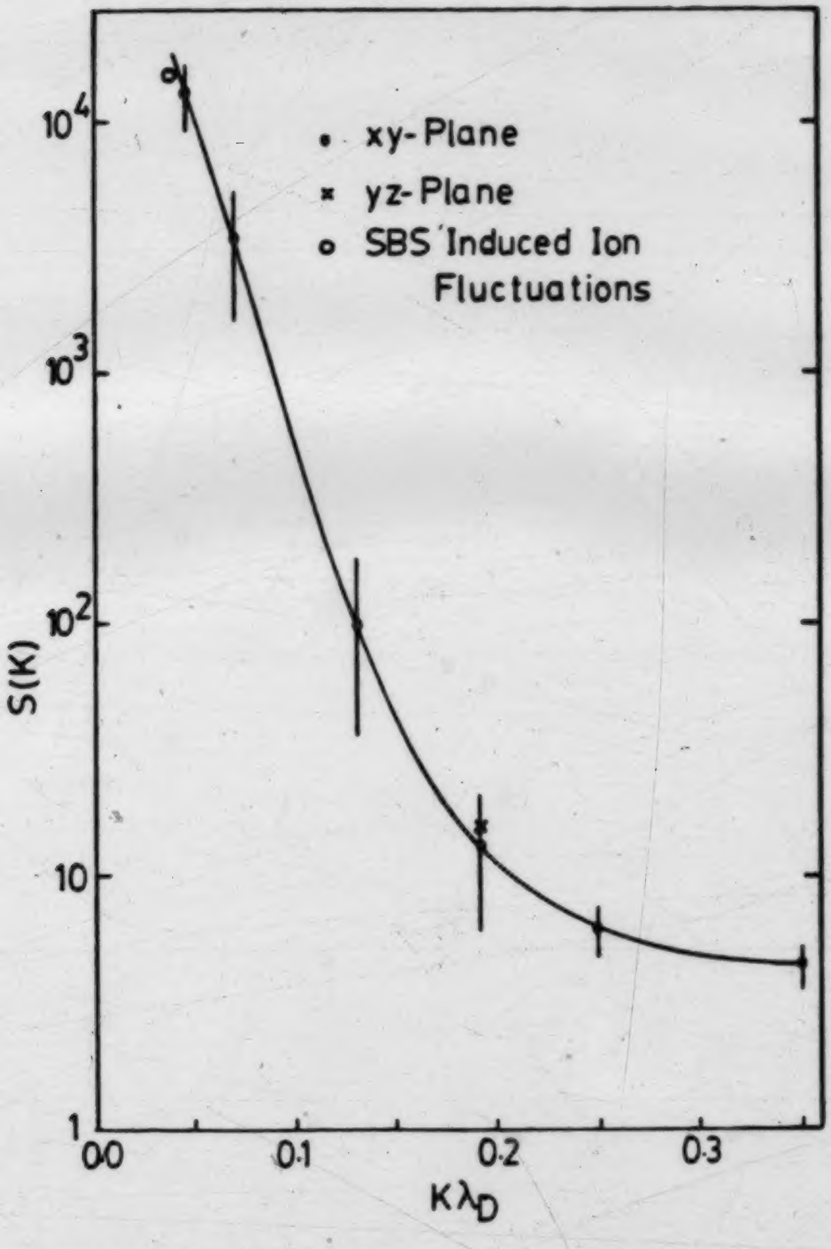

Fig. 4.14 Ion turbulence spectrum $S(k)$ as a function of $k\lambda_D$ assuming an average density $n = 0.7\ n_c$ at $T_e = 100$ eV (Case II). The error bars indicate the standard deviations for thirty shots at average focused CO_2 laser intensity of $5 \times 10^{12}\ W/cm^2$.

ion fluctuations induced by stimulated Brillouin backscattering (Fig. 4.15) and the result, shown as a circle in Fig. 4.14, fits well on the curve. It is significant that, although the SBS induced ion fluctuations (along the Z axis) and the ion turbulence in the X-Y plane are undoubtedly generated by different instability mechanisms, they are of comparable levels.

In order to estimate the absorption fraction due to ion turbulence in this experiment the $S(k)$ spectrum of Fig. 4.14 was approximated by a polynomial of the form

$$\ln S(k\lambda_D) \simeq 12.25 - 69.03(k\lambda_D) + 1.07.89(k\lambda_D)^2 \ . \qquad (4.10)$$

Integrating Eqn. (3.25) numerically (using Eqn. (4.10)) leads to a fluctuation level $(\delta n/n) \sim 0.008$ which, in turn, gives $\sum_{ki} \left(\frac{\delta n_{ki}}{n_c}\right)^2 \simeq 0.013$ and $\nu_{eff} \simeq 0.9\ \nu_{cl}$. This value is 1/4 of the ν_{eff} calculated in Case I. The lower value may be related to the longer density scale-length and greater classical absorption prior to focus. However, it is still adequate to account for the remaining 15% absorption. It should be pointed out that the density fluctuation levels, observed in Cases I and II, are much lower than the maximum level predicted by the ion trapping saturation mechanism discussed in Chapter 2.

4.3.3 Streak measurements.

In order to follow the rapid temporal variations of the enhanced ion fluctuations, a streak camera was employed to record the Thomson scattered ruby laser light. While the timing between SBS and the Thomson scattering signal was the same as in Case I (Fig. 4.1), the duration of the Thomson scattering signal for this interaction regime (Case II), when recorded by a photomultiplier, was found to be shorter than that

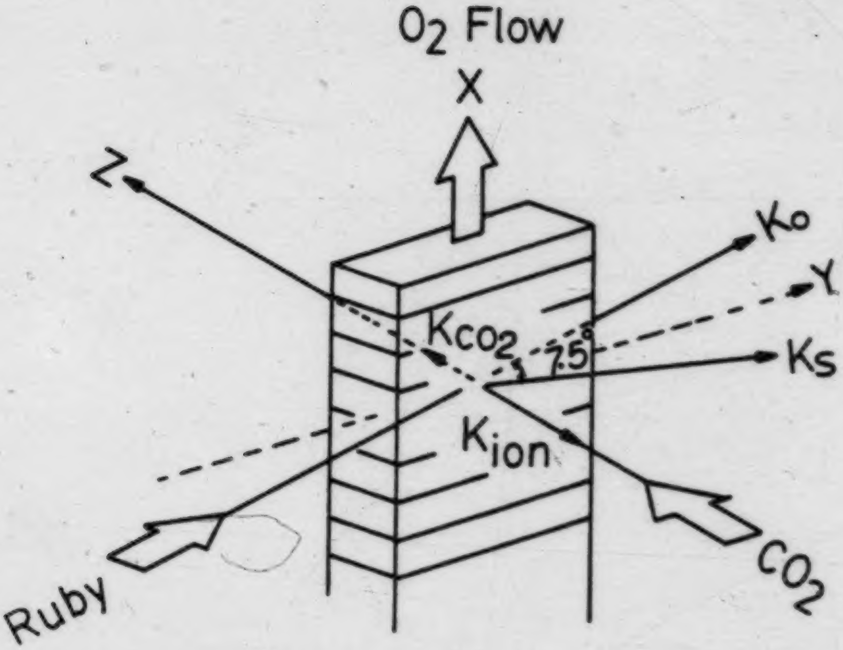
O_2 Flow
X
Z
K_o
Y
K_{CO_2}
7.5°
K_s
K_{ion}
Ruby
CO_2

Fig. 4.15 Schematic diagram of the Thomson scattering experiment to probe ion fluctuations induced by stimulated Brillouin backscattering.

observed in Case I (∿ 6 ns FWHM). But, since this was approaching the limit of the detector resolution, it is possible that the pulse duration could be much shorter than the observed one.

This was confirmed when a high speed streak camera was used. The results are summarized in Fig. 4.16 for varying observations with three different streak speeds. In general, the duration of the ion turbulence varied from approximately 3 ns (Fig. 4.16a) to as short as 250 ps (Fig. 4.16b). The risetime also varied from ∿ 1 ns to 50 ps. Highly modulated pulse structures (∿ 50 ps duration) were observed in 50% of the shots using the very high speed mode (Fig. 4.16c). This fine structure in the scattered light could not be fully accounted for by the fine structure of the incident ruby laser (monitored simultaneously with the scattered light and shown at the top of Figs. 4.16), nor to the modulations of the incident CO_2 laser beam which has a structure of $\gtrsim 3$ ns duration. Similar behaviour was observed in the scattered light of the ion fluctuations driven by SBS. In addition, changing the scattering direction form the X-Y plane to the Y-Z plane showed no systematic changes in the temporal behaviour of the scattered light. Indeed, the observed temporal changes were merely statistical and not related to the probing of CO_2 lasers. If the parametric instabilities discussed in Chapter 2 were responsible for generating the ion turbulence, then the observed variation in risetime could be explained by the wide range of the growth rate ($\gamma > 1$ ps) predicted for these instabilities when the density values accessible and the variation in v_0/v_e are taken into account. The ion trapping mechanism also predicts that saturation takes place in as short as 15 ps for $n = 0.7\, n_c$ |19|.

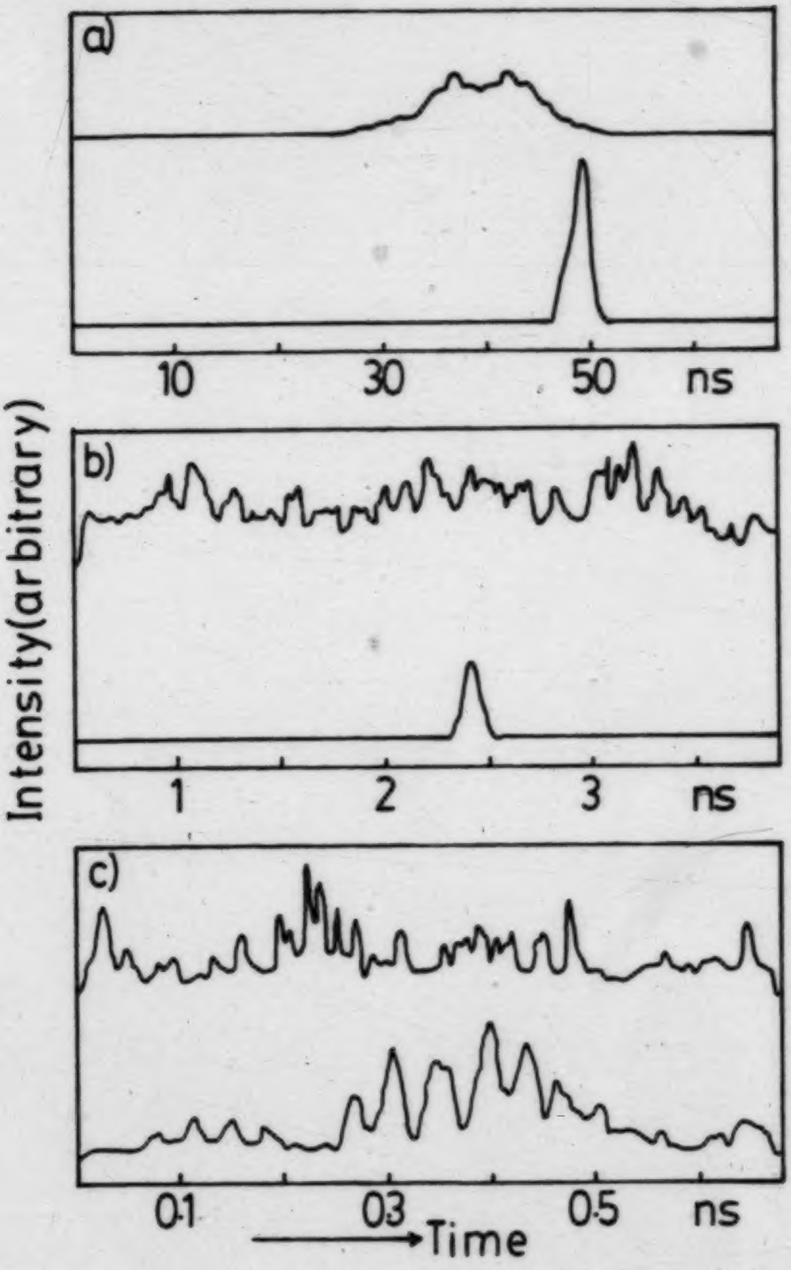

Fig. 4.16 Temporal behaviour of the Thomson scattered light (bottom) and the incident ruby light (top) in each plate showing different features; a) long lived fluctuations (∿ 3 ns), b) short lived fluctuations (250 ps) with no structure, c) ∿ 0.7 ns long fluctuations with fine structure.

The nanosecond duration of the enhanced fluctuations is significantly shorter than the value reported in Case I (FWHM $\lesssim$ 10 ns). The very real difference is not attributable to the difference between the temporal resolution of the camera and the photomultiplier. For the photomultiplier (risetime $\simeq$ 3 ns), the true duration Δ_t, the measured one, Δ_m, and the instrumental width Δ_s (= 3 ns) are governed by the relation $\Delta_t^2 = \Delta_m^2 - \Delta_s^2$. This gives, for Δ_m = 8 - 10 ns, a true duration of at least 7.4 - 9.5 ns.

Thus, the difference between turbulence duration of Case I and Case II is obvious. This again is probably due to changes in the laser plasma interaction conditions (including n and L) which might affect the growth rate and damping of the ion wave instability responsible for the observed ion fluctuations.

The streak camera also proved to be a useful tool for measureing the size of the turbulence region and for following the temporal evolution of the ion fluctuation spatial distribution. This was realized by relaying the scattering region onto the 3 mm wide slit of the camera. The measurements were done with an effective spatial resolution of as high as 33 μm (depending on the magnification of the relay lens). Figure 4.17 shows a streak photograph of a 1.2 ns duration enhanced scattering event from ion turbulence. The observed turbulence region is only 170 μm in size. The variation in the spatial extent of the measured ion turbulence was found to lie between 100 to 250 μm. The 250 μm length plasma near the CO_2 beam focus corresponds to a density which varies, for early time near breakdown, between 0.43 n_c and 0.8 n_c (Fig. 4.7). This indicates that the instability responsible for generating ion turbulence takes

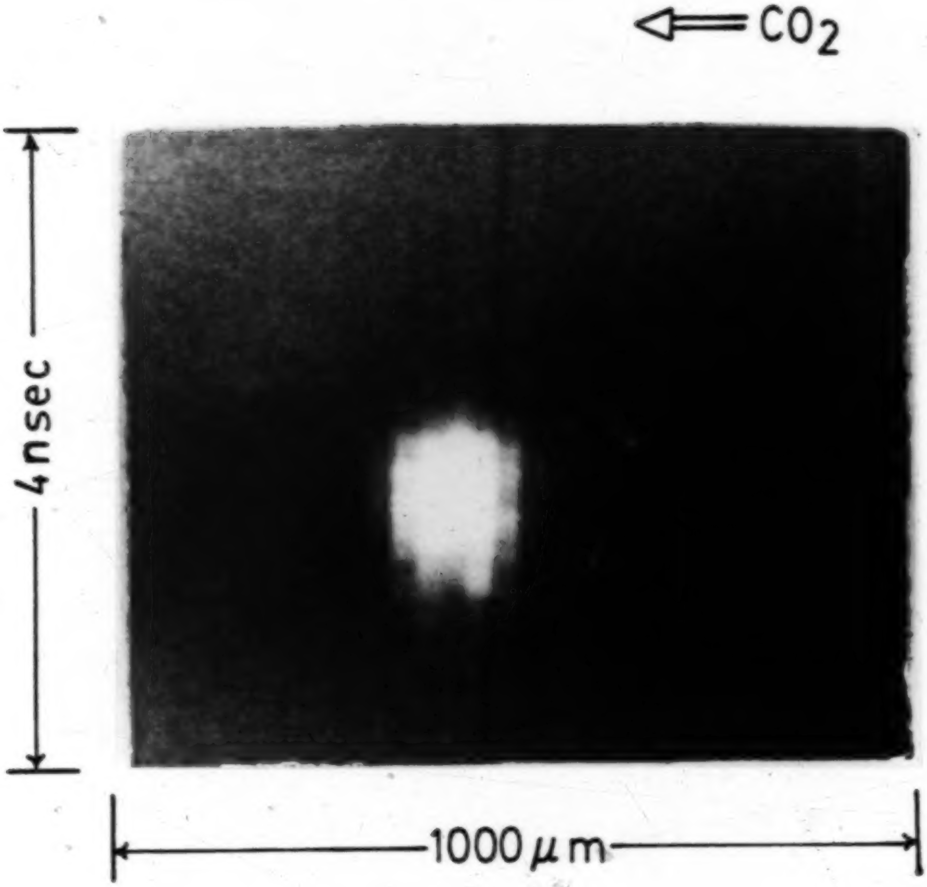
CO_2
4nsec
1000 μm

Fig. 4.17 Streak photograph of $\sim$ 1.2 ns duration enhanced scattering event from ion turbulence occupying $\sim$ 170 μm region.

place in relatively high density regions. This is consistent with the density region required to induce off-resonance OTS and PD ($n \gtrsim 0.5\, n_c$).

The time evolution of the spatial distribution of turbulence is shown (for $\theta = 16^\circ$ in the X-Y plane) for 3 ns duration (Fig. 4.18) and 0.8 ns duration (Fig. 4.19) cases. Both figures show a build-up of turbulence in two regions. This could be due to spatial inhomogeneity of the original incident CO_2 or ruby laser beams or due to filaments occurring in the plasma that make the CO_2 laser beam intensity distribution irregular. Such filaments have been observed previously in a CO_2 laser heated hydrogen plasma |20|. Figure 4.20 shows, for the same scattering angle, a rare case of turbulence in which the peak fluctuation region moves with a speed of $\sim 2 \times 10^7$ cm/sec in the direction of propagation of the CO_2 laser beam. This behaviour is similar to that observed spectrally in Case I although the speed here is 4 times higher. The measured speed is very high compared to the ion thermal speed ($\sim 2.4 \times 10^6$ cm/sec assuming $T_i = 100$ eV) and ion acoustic speed ($\sim 7.3 \times 10^6$ cm/sec for $T_e = T_i = 100$ eV and $z = 6$) and could be due to cases when higher intensity CO_2 radiation ionizes the gas ahead and then propagates towards the focus. This is characteristic of ionization (propagation) speeds observed in laser induced breakdown experiments |20|.

4.3.4 Sources of ion turbulence.

Three mechanisms for generating ion turbulence in laser produced plasma experiments were suggested in Chapter 2. These mechanisms are heat flow driven ion acoustic instability, ion-ion streaming instability and ion waves induced by parametric instabilities. The first instability is expected to take place when $zT_e > T_i$ and $u > c_s$ where u is the

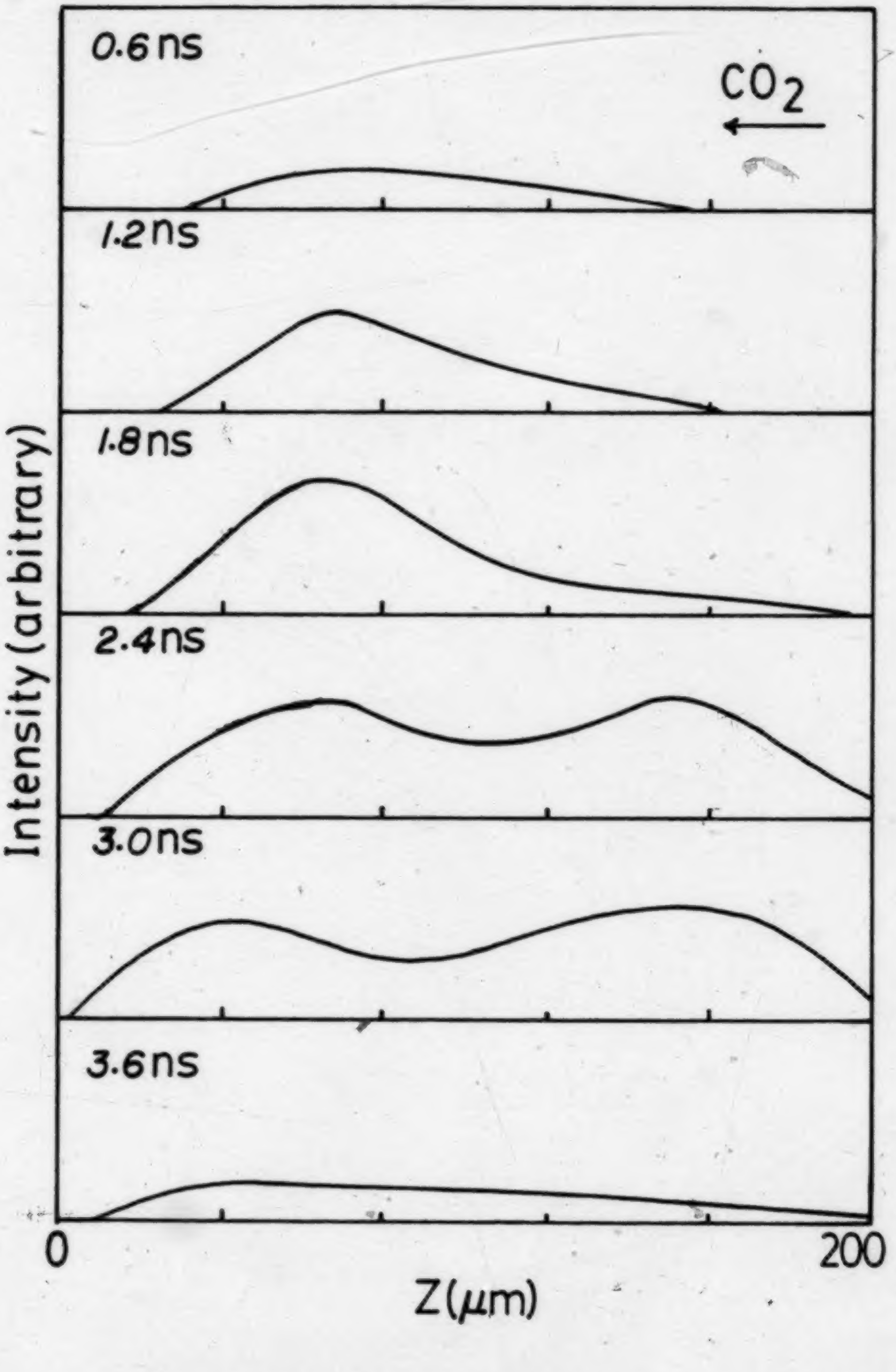

Fig. 4.18 Time evolution of the spatial distribution of turbulence for a 3 ns duration ($\theta = 16^\circ$ in the X-Y plane).

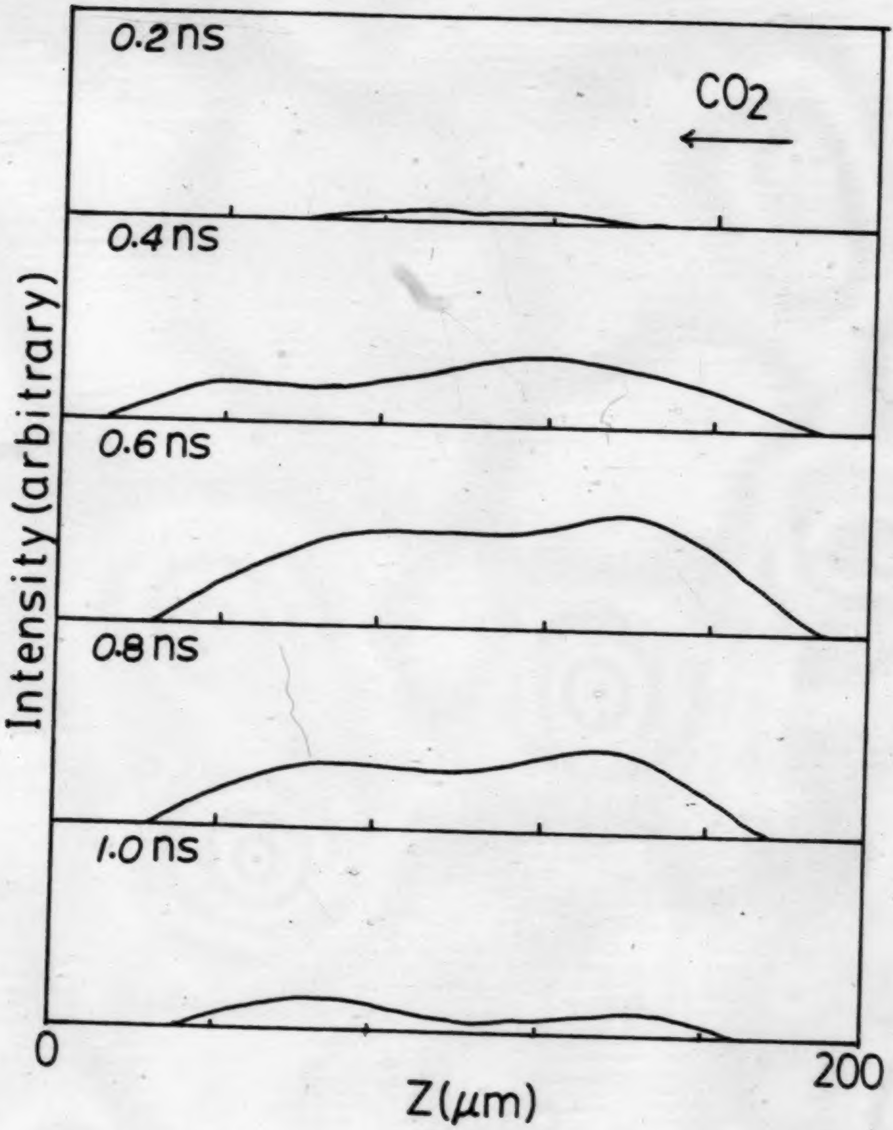

Fig. 4.19 Time evolution of the spatial distribution of turbulence for a 0.8 ns duration ($\theta = 16^{\circ}$ in the X-Y plane).

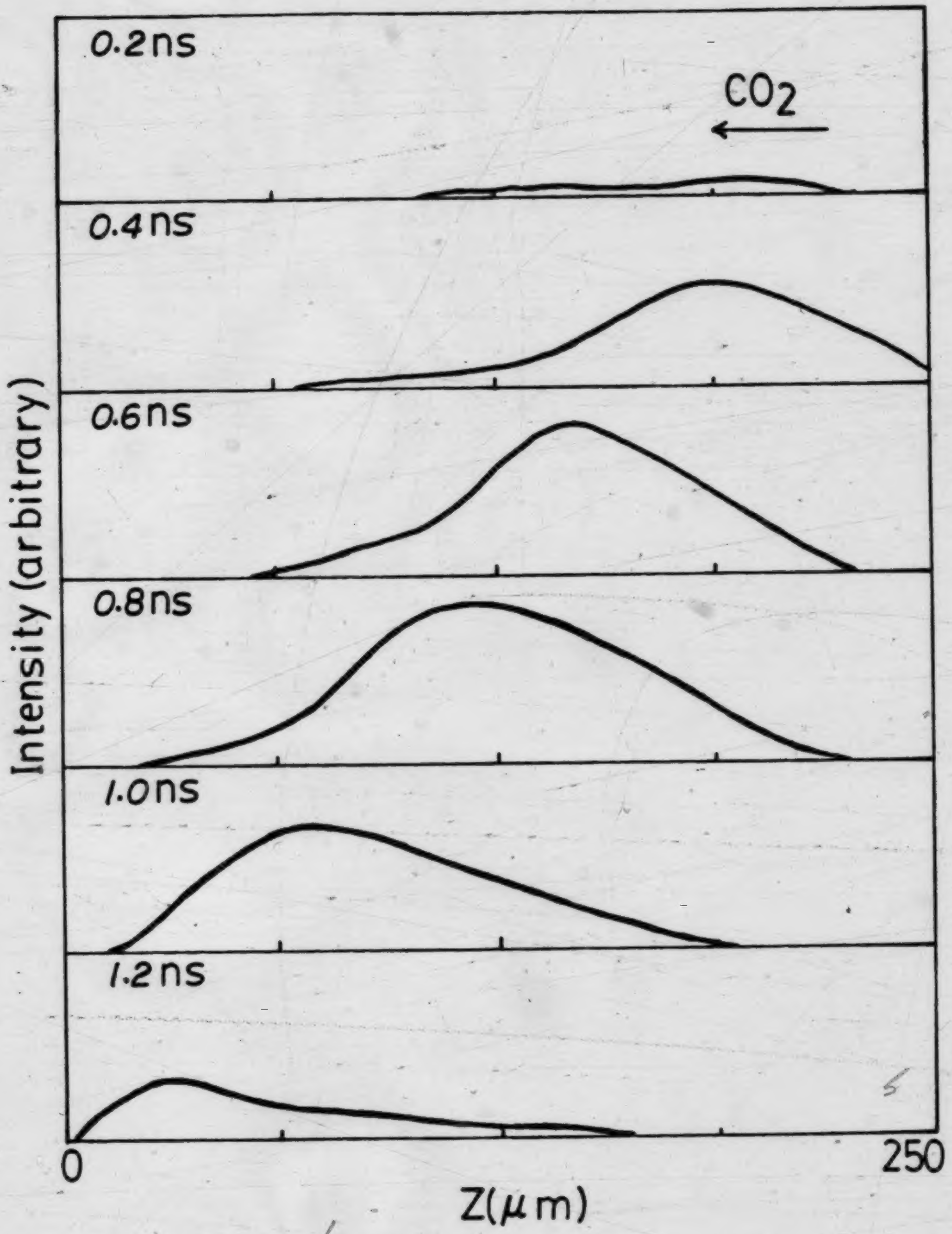

Fig. 4.20 Time evolution of the spatial distribution of turbulence showing a motion of the fluctuation region in the direction of the propagation of the CO_2 laser beam ($\theta = 16^{\circ}$ in the *X-Y* plane).

electron drift speed and c_s is the ion acoustic speed. In the current experiment the first condition was satisfied, while the second one was not always fulfilled. The spectral measurements of Case I, for example, occasionally showed a drift speed of $\leq 5 \times 10^6$ cm/sec which is close to the ion acoustic speed ($\sim 7.3 \times 10^6$ cm/sec for $T_i = T_e =$ 100 eV and $z = 6$). On other occasions no drift was observed although enhanced scattering was substantial.

Now, even if the above conditions were satisfied, the current driven ion instability is not likely to be the source of the observed ion fluctuations for three reasons: (a) the observed $S(k)$ spectrum, particularly that shown in Fig. 4.14, is not a Kadomtsev type spectrum |17| nor is it similar to any of the modified spectra that the current driven instability suggests |21|; (b) no hot electrons were observed in the present experiment which could provide a return current source for a current driven instability; (c) the ion fluctuations driven by this instability are mainly distributed within a cone (of angle $\theta \sim 50 - 60^\circ$) around the direction of the return current (CO_2 laser beam) |22|; therefore the observed fluctuations in the X-Y plane cannot be explained by this instability.

The second possible candidate, the ion-ion streaming instability, suggested by Faehl and Kruer |23| only occurs when different ion species are available (different masses or z). For species of different masses only helium ions are potentially available in the background. However, in the oxygen target where the interactions take place, their number is insignificant. It may be possible to have oxygen ions with different z but again, near the focus of the CO_2 laser beam ($\lesssim 250$ μm diameter sphere) most of the oxygen atoms will be ionized to $z = 6$. Moreover, the condition $\nu_{ii} < v_i/L$, required for this instability (Chapter 2), must be satisfied. If we assume in the best conditions that $T_e = T_i \simeq 100$ eV, $L \simeq 100$ μm and v_i is equal to the thermal ion speed, a value of $v_i/L \simeq 2.4 \times 10^9 \sec^{-1}$ will be obtained. For the same plasma parameters, one can also calculate that

$$\nu_{ii} = \nu_{ei}\left(\frac{m_e}{m_i}\right)^{\frac{1}{2}} \simeq 9 \times 10^9 \sec^{-1}.$$

Thus, the above instability condition is not satisfied and it will be even worse if $T_i < T_e$. In addition, it should be pointed out that high level ion turbulence was also observed in a pure hydrogen plasma target where species of different masses and z are negligible [14]. In conclusion, it is unlikely that the ion-ion streaming instability is a significant mechanism for generating the observed enhanced ion fluctuations in this experiment.

Before discussing the last suggested mechanism (ion waves produced by parametric instabilities) we should first mention that under the conditions of the present experiment, particularly with $v_0/v_e \leq 1.4$ (corresponding to CO_2 laser intensity $I \lesssim 5 \times 10^{12}$ W/cm^2 and $T_e \simeq 100$ eV), many nonlinear processes are expected to take place. Indeed, among the processes that have been detected previously are stimulated Brillouin and Compton scattering, filamentation, two-plasmon decay, and harmonic generation [24].

Although much emphasis has been given by many investigators to ion waves produced by parametric instabilities of importance to scattering (stimulated Brillouin) or direct absorption (PD and OTS near critical density) processes, not much attantion has been given to other instabilities such as off-resonance PD and OTS which may play an important role in underdense plasmas. Our analysis in Chapter 2 showed clearly that PD and OTS off-resonance and filamentation can easily be excited for our experimental conditions (Figs. 2.2 - 2.11).

The correlations between experimental results and the theory of ion waves generated by parametric instabilities (discussed in Chapter 2) can be summarized as follows: (a) The off-resonance PD and OTS and filamentation have higher growth rates for higher densities that may explain the existence of ion turbulence in the high density region and the reduction in the turbulence level when moving from a high density regime to a low density one; (b) The wave number of the observed turbulence could be explained by PD and OTS off-resonance in the high $k\lambda_D$ range and by filamentation and mode coupling in the low $k\lambda_D$ range; (c) Both PD and OTS off-resonance and filamentation can produce ion waves in the direction of the electric field of the incident CO_2 laser beam (indeed, the growth rate γ is maximum in this direction) which are of interest for absorption; (d) Calculated values of γ for these instabilities agree qualitatively with the observed risetime range of the ion turbulence when the density values accessible and the variations in v_0/v_e, due to temporal modulation in CO_2 laser power, are taken into account; (e) The narrow spectral features of ion turbulence, observed in some shots, could also be explained by the purely growing modes of these instabilities (i.e., $\omega_R = 0$).

In addition, recent theoretical studies of PD and OTS off-resonance |25| have shown that $S(k)$ can be enhanced in the presence of a strong pump, even for stationary stable plasmas. The results are summarized in Fig. 4.21 for oxygen plasma with $z = 6$, $T_i = T_e = 100$ eV and $n = 0.6\, n_c$ and $0.8 n_c$ for (a) and (b) respectively. The values of

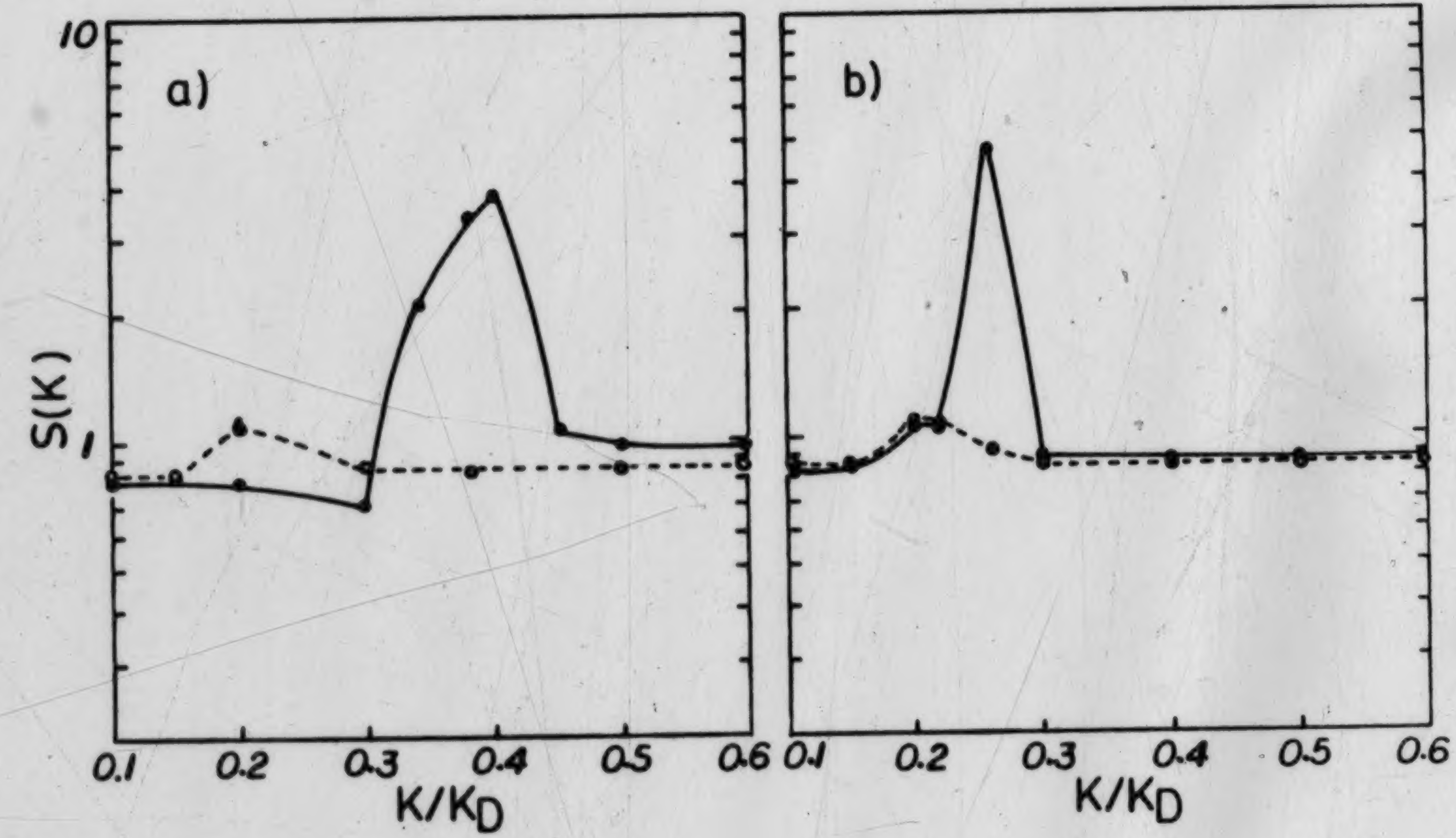

Fig. 4.21 Numerical values of $S(k)$ versus k/k_D for oxygen plasma with $z = 6$ and $T_i = T_e = 100$ eV. Dashed curves correspond to $v_0/v_e = 0$. a) $v_0/v_e = 0.6$, $n/n_c = 0.6$, b) $v_0/v_e = 0.05$, $n/n_c = 0.8$.

v_0/v_e were taken just below the threshold values of PD and OTS off-resonance. Considerable enhancement over thermal fluctuation levels (shown dashed) can be seen. Moreover, these calculations set a lower bound for enhancement. With higher values of v_0/v_e (above threshold) the enhancement is naturally expected to be substantially higher (ultimately limited by some nonlinear saturation processes).

Before coming to any final conclusions, three observational facts must be recalled: first, the shape of $S(k)$ observed in Case I and Case II; second, the isotropy of the ion turbulence; third, the absence of electron features in Thomson scattering when electron waves can be generated by PD and OTS off-resonance. Regarding the first point, although no theoretical knowledge is available concerning $S(k)$ for ion turbulence generated by off-resonance PD and OTS and filamentation above the instability threshold, if the observed $S(k)$ spectrum is related to the above instabilities, then it should be a function of density and pump strength. This may be the reason for observing different $S(k)$ spectra in Case I and Case II. In addition, because of the considerable variation in plasma density available in the scattering volume, the observed spectrum is an integration of the form factor over that density range.

With respect to the second point, the low $k\lambda_D$ part of the spectrum can be explained by filamentation and mode coupling (Brillouin) instabilities, which cover a wide angle $\overline{E}$ between the electric field of the CO_2 laser beam and the $\overline{k}$ vector of the ion waves (Fig. 2.2 - 2.5). For the other instabilities (off-resonance PD and OTS), although they are functions of θ, the reduction in the growth rate at $\theta = 60^\circ$, compared to $\theta = 0$, is $\sim$ 60-70% (Fig. 2.13). This reduction is even lower if we take into account the angle subtended by the CO_2 laser beam (∿ 29°) when focused by an f/2 mirror. Finally, the electron waves generated by off-resonance instability are heavily damped. A simple calculation for $T_e = 100$ eV, $k\lambda_D = 0.3$ and $n = 0.7\ n_c$, shows that Landau damping is $\sim 8 \times 10^{12}$ sec^{-1}. This is somewhat greater than the growth rate of the instabilities mentioned above. Therefore, the instability is a heavily damped driven mode.

In conclusion, it appears more likely that our observations may be related to strong pump induced ion instabilities generated by off-resonance PD and OTS, filamentation and mode coupling processes. However, in order to convincingly demonstrate this, considerable additional experimental and theoretical study is required. This will be discussed in the next chapter.

Importantly, the experimental work presented here is a beginning towards understanding complicated non-equilibrium phenomena which can be induced in plasma under the influence of a strong external electromagnetic wave.

CHAPTER 5

SUMMARY AND CONCLUSION

A successful attempt has been made to study ion turbulence in high intensity CO_2 laser produced plasmas both theoretically and experimentally. In the theoretical aspect of the study, emphasis has been given to ion waves generated by parametric instabilities in an underdense plasma $(n < n_c)$. The Drake dispersion equation for $k\lambda_D \ll 1$ and the Silin dispersion equation for $k\lambda_D = 0(1)$ have been solved numerically for a homogeneous oxygen plasma in the presence of a high intensity CO_2 laser beam. The results have shown that ion waves can be easily induced by stimulated Brillouin scattering, filamentation and off-resonance electron-ion decay and oscillating two stream instabilities. The latter instabilities are believed to be possible candidates for generating the enhanced ion fluctuations associated with the anomalous absorption reported previously.

On the experimental side the Thomson scattering technique was applied to study ion turbulence in the CO_2 laser heated oxygen gas target plasma. Measurements were made for two density regimes, short scale length and long scale length. Both regimes showed strong enhancement of the ion fluctuations over thermal levels. The turbulence level along with temporal and spectral analysis of the ion fluctuations indicates that the measured ion turbulence could account for the anomalous absorption observed in this experiment.

In the long scale length regime the $S(k)$ spectrum was measured for ion turbulence in and out of the plane of the target. The approximately isotropic spectrum that was observed suggests that the enhancement in the plane of the target could be as strong as that induced by low threshold parametric instabilities such as SBS (for the same wave number). High speed streak camera measurements of the scattered light show short lived and fast rising ion fluctuations. These measurements also indicate that ion turbulence is generated in a high density region in the vicinity of the focal point of the laser beam. This is consistent with the density regime at which OTS and PD off-resonance can be excited.

The possible mechanisms for generating ion fluctuations were discussed in the light of the experimental results. It is believed that the observed ion fluctuations are likely related to strong pump induced parametric instabilities (particularly off-resonance PD and OTS instabilities and filamentation) rather than the current driven ion instability or ion-ion streaming instability.

Since the analyses performed in this thesis were carried out only for thermal homogeneous plasma, the effect of the inhomogeneity in a plasma on off-resonance PD and OTS instabilities, together with the different $S(k)$ spectra produced by these instabilities in a non-thermal plasma, are worth further analysis.

Experimental verification of the existence of both PD and OTS off-resonance instabilities is needed. This could be achieved by two different methods; first by varying the intensity of the incident laser beam in order to determine the thresholds of these instabilities, and second by the proper selection of a plasma density region, it might be possible to simultaneously observe features of both electrons and ions in a Thomson scattering experiment.

The effect of ion fluctuations on energy transport in laser/plasma interactions is another interesting topic for investigation. A possible way of doing it is through the measurement of the particle energy distribution and determining the corresponding energy flux limit.

REFERENCES

CHAPTER 1

1. J. Dawson, P. Kaw, and B. Green, Phys. Fluids, 12, 875 (1969).

2. C.E. Max, "Laser-Plasma Interaction", eds., R. Baliam,and J. Adam, North-Holland, N.Y., (1982).

3. A.B. Langdon, Phys. Rev. Lett., 44, 575 (1980).

4. W.L. Kruer, and J.M. Dawson, Phys. Fluids, 15, 446 (1972).

5. J.M. Dawson and C. Oberman, Phys. Fluids, 5, 517 (1962) and 6, 394 (1963).

6. R. Faehl and W.L. Kruer, Phys. Fluids, 20, 55 (1977).

7. W. Manheimer, Phys. Fluids, 20, 265 (1977).

8. W. Manheimer, *et al.*, Phys. Rev. Lett., 38, 1135 (1977).

9. W.M. Manheimer, and D.G. Colombant, Phys. Fluids, 21, 1818 (1978).

10. D.G. Colombant, and W.M. Manheimer, Phys. Fluids, 23, 2512 (1980).

11. D.W. Forslund, *et al.*, Bull. Am. Phys. Soc., 20, 1377 (1975).

12. D.R. Gray and J.D. Kilkenny, Plasma Phys., 22, 81 (1980).

13. C.J. Walsh and H.A. Baldis, Phys. Rev. Lett., 48, 1483 (1982).

14. R. Giles and A.A. Offenberger, Phys. Rev. Lett., 50, 421 (1983).

CHAPTER 2

1. W.M. Manheimer, *et al.*, Phys. Rev. Lett., 38, 1135 (1977).

2. W.M. Manheimer and D.G. Colombant, Phys. Fluids, 21, 1818 (1978).

3. R.J. Faehl and W.L. Kruer, Phys. Fluids, 20, 55 (1977).

4. W.M. Manheimer, Phys. Fluids, 20, 265 (1977).

5. D.G. Colombant and W.M. Manheimer, Phys. Fluids, 23, 2512 (1980).

6. K. Estabrook, Phys. Rev. Lett., 47, 1396 (1981).

7. A.A. Offenberger, *et al.*, Phys. Rev. Lett., 40, 873 (1978).

8. A.A. Ofenberger and A. Ng, Phys. Rev. Lett., 45, 1189 (1980).

9. Y.S. Al-Shiraida, *et al.*, Phys. Rev. A25, 2857 (1982).

10. R. Giles and A.A. Offenberger, Phys. Rev. Lett., 50, 421 (1983).

11. C.J. Walsh and H.A. Baldis, Phys. Rev. Lett., 48, 1483 (1982).

12. D.R. Gray and J.D. Kilkenny, Plasma Phys., 22, 81 (1980).

13. B.B. Kadomtsev, "Plasma Turbulence", Academic Press, N.Y., Chap. 4 (1965).

14. D.W. Forslund, *et al.*, Bull. Am. Phys. Soc., 20, 1377 (1975).

15. J.F. Drake, *et al.*, Phys. Fluids, 17, 778 (1974).

16. C.S. Liu and P.K. Kaw, "Advances in Plasma Physics", eds. A. Simon and W.B. Thompson, Wiley, N.Y., Vol. 6, Pt. 1, (1976).

17. V.P. Silin, Sov. Phys., JETP, 24, 1242 (1967).

18. J.R. Sanmartin, Phys. Fluids, 13, 1533 (1970).

19. P.K. Kaw and J.M. Dawson, Phys. Fluids, 14, 792 (1971).

20. D. Biskamp and R. Chodura, Phys. Rev. Lett., 27, 1553 (1971).

21. M. Lampe, *et al.*, Phys. Fluids, 15, 662 (1972).

22. W. Manheimer and R. Flynn, Phys. Fluids, 17, 409 (1974).

23. J.M. Dawson, *et al.*, "Dynamics of Ionized Gases", eds., M. Lighthill, *et al.*, Univ. of Tokyo, Tokyo, p. 47 (1973).

24. W. Rozmus, *et al.*, Phys. Fluids, 28, 920 (1985).

25. J.M. Dawson, P. Kaw, and B. Green, Phys. Fluids, 12, 875 (1969).

26. J.M. Dawson and C. Oberman, Phys. Fluids, 5, 517 (1962) and 6, 394 (1963).

27. W. Rozmus, *et al.*, Phys. Fluids, 27, 589 (1983).

CHAPTER 3

1. N.H. Burnett and A.A. Offenberger, J. Appl. Physics, 44, 3617 (1973).

2. R. Giles, Ph.D. Thesis, Dept. of Electrical Eng., U. of A. (1983).

3. B.W. Arnold and A.A. Offenberger, Rev. Sci. Inst., 47, 762 (1976).

4. F.C. Jahoda, *et al.*, Phys. Rev., 119, 843 (1960).

5. D. Salzmann, Elect. Eng. Dept., U. [illegible] A. (1978) (unpublished).

6. R.C. Elton and A.D. Anderson, NRL Report #6541, March (1967).

7. F.C. Jahoda and G.A. Sawyer, "Methods of Experimental Physics", eds. H.R. Griem and R.H. Lovberg, Academic Press, N.Y., Vol. 9, Part B, p. 1 (1971).

8. S. Tolansky, "An Introduction to Interferometry", Longmans, Green and Co., London, Ch. 4 (1955).

9. D.E. Evans and J. Katzenstein, Rep. Prog. Phys. 207, 32 (1969).

10. A.W. DeSilva and G.C. Goldenbaum, "Methods of Experimental Physics", eds. H.R. Griem and R.H. Lovberg, Academic Press, N.Y., Vol. 9, Part A, p. 61 (1970).

11. E.E. Salpeter, J. Geophys. Res., 1321, 68 (1963).

12. J. Sheffield, "Plasma Scattering of Electromagnetic Radiation", Academic Press, N.Y. (1975).

13. D.R. Gray and J.D. Kilkenny, Plasma Physics, 81, 22 (1980).

14. B.B. Kadomtsev, "Plasma Turbulence", Academic Press, N.Y. (1965).

CHAPTER 4

1. A.A. Offenberger and A. Ng, Plasma Phys. and Contr. Nucl. Fus. Res., VII, 735 (1980).

2. R. Giles, Ph.D. Thesis, Dept. of Elect. Eng., U. of A. (1983).

3. A.A. Offenberger and A. Ng, Phys. Rev. Lett., 45, 1189 (1980).

4. J. Dawson, P. Kaw and B. Green, Phys. Fluids, 12, 875 (1969).

5. D. Salzmann, Elect. Eng. Dept., Univ. of Alberta (1978) (unpublished).

6. S.L. Leonard, "Plasma Diagnostic Techniques", eds. R.H. Huddlestone and S.L. Leonard, Academic Press, N.Y., Ch. 2 (1965).

7. J. Sheffield, "Plasma Scattering of Electromagnetic Radiation", Academic Press, N.Y., p. 149 (1975).

8. R.D. Milroy, *et al.*, Can. J. Phys., 57, 514 (1979).

9. J.J. Sanderson, "Plasma Physics and Nuclear Fusion Research", ed. Richard D. Gill, Academic Press, London, p. 139 (1981).

10. D.R. Dum, *et al.*, Phys. Rev. Lett., 32, 1231 (1974).

11. Y. Kawai and M. Guyot, Phys. Rev. Lett., 39, 1141 (1977).

12. R.C. Malone, *et al.*, Phys. Rev. Lett., 34, 721 (1975).

13. D.R. Gray and J.D. Kilkenny, Plasma Physics, 22, 81 (1980).

14. A.A. Offenberger, *et al.*, Phys. Rev. Lett., 40, 873 (1978).

15. C.J. Walsh, *et al.*, Phys. Fluids, 25, 2326 (1982).

16. E.B. Turner, "Plasma Diagnostic Techniques", eds. R.H. Huddlestone and S.L. Leonard, Academic Press, N.Y., Ch. 7 (1965).

17. B.B. Kadmotsev, "Plasma Turbulence", Acad. Press N.Y.. Ch. 4 (1965).

18. R.E. Slusher, *et al.*, Phys. Rev. Lett., 36, 674 (1976).

19. W. Manheimer and R. Flynn, Phys. Fluids, 17, 409 (1974).

20. A.A. Offenberger and N.H. Burnett, Can. J. Phys., 53, 1360 (1975).

21. W. Horton, *et al.*, Phys. Rev., A14, 424 (1978).

22. W.M. Manheimer, *et al.*, Phys. Rev. Lett., 38, 1135 (1977).

23. R.J. Faehl and W.L. Kruer, Phys. Fluids, 20, 55 (1977).

24. A.A. Offenberger, Lab. Report (1981).

25. W. Rozmus, *et al.*, Phys. Fluids, 27, 589 (1983).

APPENDIX A

1. B. Carnahan, H.A. Luther and J.O. Wilkes, "Applied Numerical Methods", John Wiley, N.Y., (1969).

2. B.D. Fried and S.D. Conte, "The Plasma Dispersion Function", Academic Press, N.Y., (1961).

APPENDIX B

1. K.R. Manes and H.J. Seguin, J. Appl. Phys., 43, 5073 (1972).
2. J. Gilbert, *et al.*, Can. J. Phys., 50, 2523 (1972).
3. K.J. Andrews, P.E. Dyer and D.J. James, J. Phys., E8, 493 (1975).
4. A.R. Davies, *et al.*, J. Appl. Phys., 47, 2037 (1976).
5. N.H. Burnett and A.A. Offenberger, J. Appl. Phys., 44, 3617 (1973).
6. P. Henrici, "Essentials of Numerical Analysis", John Wiley and Sons, N.Y., p. 311 (1982).

APPENDIX C

1. C.J. Cremers and R.C. Birkebak, Appl. Optics, 1057, 5 (1966).
2. O.H. Nestor and H.N. Olsen, SIAM Rev., 200, 2 (1960).

APPENDIX E

1. R.N. Jones, *et al.*, Spectrochimica Acta, 23A, 925 (1967).
2. A.L. Khidir and J.D. Declus, Spectrochimica Acta, 18, 1629 (1962).

APPENDIX A

SOLUTION OF THE DISPERSION EQUATION

The reduced form of the Drake dispersion function, Eqn. (2.5), and the general dispersion function of Sanmartin, Eqn. (2.6), were solved graphically by finding the values of $z = \omega + i\gamma$ which satisfy the conditions

$$\mathrm{Re}\, F(z) = 0 \qquad (A.1)$$

and

$$\mathrm{Im}\, F(z) = 0 \qquad (A.2)$$

separately, where $F(z)$ is the dispersion function. The intersection (or intersections) of the curves of z that satisfy (A.1) and (A.2), in the $\omega\gamma$ diagram, is the solution to the function $F(z) = 0$. Separation of the real and imaginary parts of $F(z)$ was not practical analytically without a proper approximation, and therefore the procedure was done numerically. Neither Newton's method nor its modifications were successful in finding the roots of Eqns. (A.1) and (A.2) because the roots are so close to each other and convergence could not be achieved. Instead, a simple technique called the bisection or half-interval method |1| was used. Suppose, as an example, that the roots of $S(z) = \mathrm{Re}\, F(z) = 0$ are required. We first keep one variable fixed, say ω, and evaluate $S(z)$ at equal intervals in a certain range of γ (Fig. A.1). The bisection method gives a root if $S(\omega_0,\gamma_a)$ and $S(\omega_0,\gamma_b)$ are opposite in sign. Next we evaluate $S(z)$ at (ω_0,γ_c) where $\gamma_c = (\gamma_a+\gamma_b)/2$. $S(\omega_0,\gamma_c)$ will be either zero or have the sign of $S(\omega_0,\gamma_a)$ or the sign

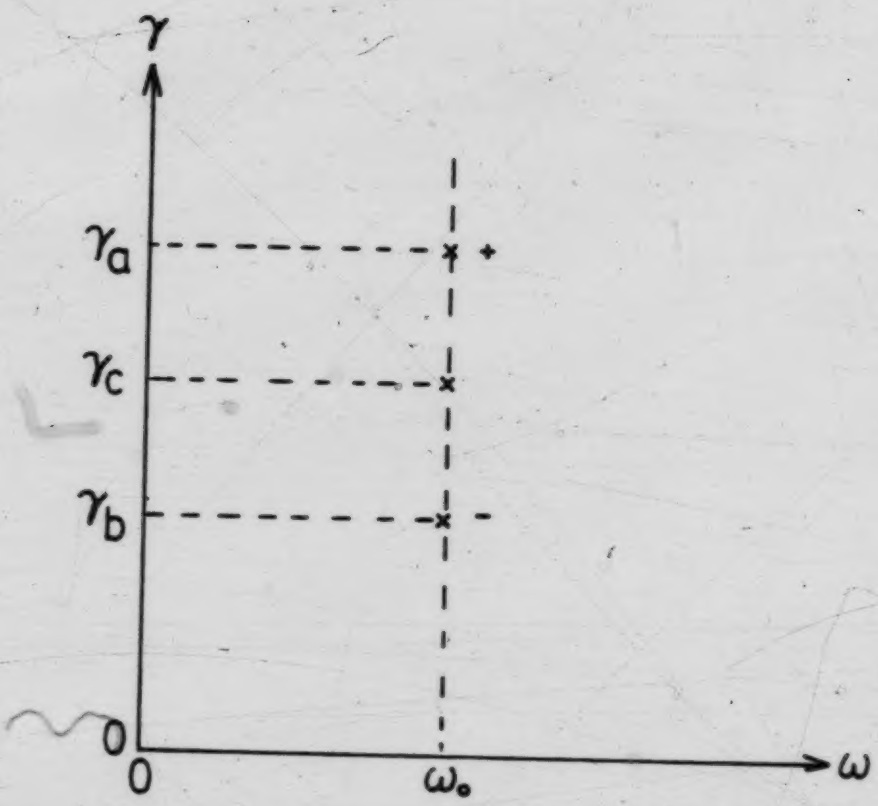
γ
γ_a
γ_c
γ_b
+
-
0
0
ω_o
ω

Fig. A.1 Roots found using the bisection method.

of $S(\omega_0, \gamma_b)$. If $S(\omega_0, \gamma_c)$ is not zero $S(z)$ will be evaluated at point (ω_0, γ_d), where $\gamma_d = (\gamma_c + \gamma_a)/2$ or $= (\gamma_c + \gamma_b)/2$, whichever point, γ_a or γ_b has an opposite sign to γ_c. Continuing in this manner, there is always a point in the interval for which $F(z) = 0$. Ten to fifteen operations were found to be adequate enough to find fairly accurate roots in any pair of points that have opposite signs.

Next, we vary ω and look at other roots. The same procedure was applied to the imaginary part of the function $F(z)$.

Programs FILAM and DISP1 were written in FORTRAN to solve Eqns. (2.5) and (2.6) respectively. It is more convenient for understanding the programs to write the variables of these equations in terms of parameters which are of interest to us. We define first the following normalized complex frequencies

$$z = \frac{\omega}{k(T_i/m_i)^{\frac{1}{2}}\sqrt{2}} \tag{A.3}$$

and

$$z_1 = \frac{\omega}{k(T_e/m_e)^{\frac{1}{2}}\sqrt{2}} = z\left(\frac{T_i}{T_e}\right)^{\frac{1}{2}}\left(\frac{m_e}{m_i}\right)^{\frac{1}{2}} , \tag{A.4}$$

where ω $(= \omega_R + i\gamma)$ is the complex frequency which appeared in the general susceptibility of Eqn. (2.7). With Maxwellian distribution it is easy to show that χ_α^n can be written in the forms

$$\chi_i = \left(\frac{k_D}{k}\right)^2 z_i\left(\frac{T_e}{T_i}\right)|1 + zZ(z)| , \tag{A.5}$$

$$\chi_e^j = \left(\frac{k_D}{k}\right)^2 |1 + (z_1 + j\Omega)Z(z_1 + j\Omega)| , \tag{A.6}$$

where z_i is the ionization degree,

$$\Omega = \frac{\omega_0}{\sqrt{2}\, k(T_e/m_e)^{\frac{1}{2}}} = \frac{1}{\sqrt{2}} \frac{\omega_0}{\omega_{pe}} \frac{k}{k_D}$$

and the function Z is called the plasma dispersion function and is defined by the integral

$$Z(z) = \pi^{-\frac{1}{2}} \int_{-\infty}^{\infty} dx \exp(-x^2)/(x-z) \; . \qquad (A.7)$$

The function $Z(z)$ was solved by series expansion in the subroutine ZP1 following the method of |2|. The argument of the Bessel function in Eqn. (2.6), $k \dfrac{eE_0}{m_e\omega_0^2} \cos(\theta)$, which will be called α, can be written as follows:

$$\alpha = \frac{k}{\omega_0} \frac{eE_0}{m_e\omega_0} \cos(\theta) = \frac{v_0}{\omega_0} k \cos(\theta) = \left(\frac{v_0}{v_e}\right)\left(\frac{k}{k_D}\right)\left(\frac{k_D v_e}{\omega_0}\right)\cos(\theta) =$$

$$\left(\frac{v_0}{v_e}\right)\left(\frac{k}{k_D}\right)\left(\frac{\omega_{pe}}{\omega_0}\right) \cos(\theta) = \left(\frac{v_0}{v_e}\right)\left(\frac{k}{k_D}\right)\left(\frac{n}{n_c}\right)^{\frac{1}{2}}\cos(\theta) \; . \qquad (A.8)$$

Thus, the important parameters in Eqn. (2.6) are $\dfrac{v_0}{v_e}$, $\dfrac{k}{k_D}$, $\dfrac{n}{n_c}$, $\dfrac{T_e}{T_i}$, z_i and θ.

Similarly the functions $D_\pm$ of Eqn. (2.5) can be written in the form

$$D_\pm = \omega_{pe}^2 \left| \left(\frac{k}{k_D}\right)^2 \left(\frac{c}{v_e}\right)^2 \pm 2\left(\frac{k}{k_D}\right)\left(\frac{k_0}{k_D}\right)\left(\frac{c}{v_e}\right)^2 \cos(\theta) \pm \right.$$

$$\left. 2\sqrt{2}\left(\frac{k}{k_D}\right)\left(\frac{n_c}{n}\right)^{\frac{1}{2}} z_1 - 2\left(\frac{k}{k_D}\right)^2 z_1^2 \right| , \qquad (A.9)$$

with $\varepsilon = 1 + \chi_e + \chi_i$ while χ_e and χ_i are given by Eqns. (A.5) and (A.6) with $n = 0$.

The list of the computer programs and their subroutines are given below. The searched roots are given in the normalized form

$z = x + i_y$ where $x = \dfrac{\omega_R}{\sqrt{2}\, k(T_i/m_i)^{\frac{1}{2}}}$ and $y = \dfrac{\gamma}{\sqrt{2}\, k(T_i/m_i)^{\frac{1}{2}}}$.

```
C     ***********************************************************
C     * PROGRAM DISP1 FOR SOLVING THE GENERAL DISPERSION EQUA-*
C     * TION OF SILIN & SANMARTIN. THE FIRST INPUT TO THIS    *
C     * PROGRAM CONTAINS TE & TI (ELECT. & ION TEMP.. MI (ION *
C     * MASS NUMBER) & ZI (IONIZATION DEGREE). THE SECOND     *
C     * INPUT CONTAINS K (IN UNITS OF KD). N (IN UNITS OF NC) *
C     * VE (IN UNITS OF VO) & CTH (COS OF THE ANGLE BETWEEN E *
C     * & K. THE PROGRAM REQUIRES ONE SUBROUTINE (BESJ) & TWO *
C     * EXTERNAL FUNCTIONS (F & ZP1).                         *
C     ***********************************************************
      COMPLEX Z,ZO,Z1,Z2,F,S(200)
      REAL K,N,MI
      DIMENSION Y(200),S1(200),Y1(25),Y2(25),Y3(25),Y4(25),S2(200)
      COMMON K,A,ZI,T,OM,BJ(20)
      READ(5,1)TE,TI,MI,ZI
    1 FORMAT(4F6.2)
      T=TI/TE
      WRITE(3,20)TE,T,MI,ZI
      READ(5,2)K,N,V,CTH
    2 FORMAT(4F6.3)
      WRITE(3,21)K,N,V,CTH
      OM=O.7071/(K*SQRT(N))
      ALPHA=K*V*CTH*SQRT(N)
C     CALCULATION OF 20 TERMS OF BESSLE FUNCTION
      DO 3 I=1,20
      J=I-1
      CALL BESJ(ALPHA,J,H,IRE)
      BJ(I)=H*H
    3 CONTINUE
      A=T/(1836.2*MI)
      A=SQRT(A)
C     THIS INPUT DETERMINES THE RANGE OF THE NORMALIZED REAL (X)
C     & THE IMAGINARY (Y) PARTS OF THE FREQUENCY. N1 & N2 ARE
C     THE NUMBER OF STEPS IN X & Y. DX & DY ARE STEPS AND DXO &
C     DYO ARE THE STARTING POINTS.
      READ(5,22)N1,N2,DX,DY,DXO,DYO
      K=K*K
C     SEARCHING FOR POSSIBLE ROOTS OF THE REAL & IMAG. PARTS OF
C     THE DISPERSION EQUATION.
      DO 16 I=1,N1
      X=DX*I+DXO
      WRITE(3,23)X
      DO 4 J=1,N2
      Y(J)=DY*J+DYO
      Z=CMPLX(X,Y(J))
      S(J)=F(Z)
      S1(J)=REAL(S(J))
    4 S2(J)=AIMAG(S(J))
      IR=O
      II=O
      DO 6 J=2,N2
      F1=S1(J)/S1(J-1)
      IF(F1.GT.O.O)GO TO 5
      IR=IR+1
      Y1(IR)=Y(J-1)
      Y2(IR)=Y(J)
    5 F2=S2(J)/S2(J-1)
      IF(F2.GT.O.O)GO TO 6
      II=II+1
      Y3(II)=Y(J-1)
      Y4(II)=Y(J)
    6 CONTINUE
C     USING BISECTION METHOD TO DETERMINE THE REAL ROOTS OF THE
C     DISPERSION EQUATION.
      IF(IR.EQ.O)GO TO 11
      DO 10 K1=1,IR
      Y11=Y1(K1)
      Y22=Y2(K1)
      Z1=CMPLX(X,Y11)
      Z2=CMPLX(X,Y22)
      F1=REAL(F(Z1))
      F2=REAL(F(Z2))
      DO 8 KO=1,20
      YO=(Y22+Y11)/2.DO
      ZO=CMPLX(X,YO)
      FO=REAL(F(ZO))
      FF=FO/F1
      IF(FF.GT.0.0)GO TO 7
      F2=FO
      Y22=YO
      GO TO 8
    7 F1=FO
      Y11=YO
    8 CONTINUE
      WRITE(3,9)YO,FO
    9 FORMAT(10X,'Y=',E12.5,5X,'RE(D)=',E12.5)
   10 CONTINUE
C     USING BISECTION METHOD TO DETERMINE THE IMAG. ROOTS
   11 IF(II.EQ.0)GO TO 16
      DO 15 K1=1,II
      Y33=Y3(K1)
      Y44=Y4(K1)
      Z1=CMPLX(X,Y33)
      Z2=CMPLX(X,Y44)
      F1=AIMAG(F(Z1))
      F2=AIMAG(F(Z2))
      DO 13 KO=1,20
      YO=(Y44+Y33)/2.DO
      ZO=CMPLX(X,YO)
      FO=AIMAG(F(ZO))
      FF=FO/F1
      IF(FF.GT.0.0)GO TO 12
      F2=FO
      Y44=YO
      GO TO 13
   12 F1=FO
      Y33=YO
   13 CONTINUE
      WRITE(3,14)YO,FO
   14 FORMAT(10X,'Y=',E12.5,5X,'IM(D)=',E12.5)
   15 CONTINUE
   16 CONTINUE
   20 FORMAT(5X,'TE=',F6.1,5X,'TI/TE=',F6.3,5X,'MI=',F5.2,5X,
     1'Z=',F5.2)
   21 FORMAT(5X,'K/KD=',F5.3,5X,'N/NC=',F5.3,5X,'VO/VT=',
     1F5.2,5X,'COS( )=',F6.2)
   22 FORMAT(2I3,4F6.3)
   23 FORMAT(15X,'***X=',F7.4,'***')
      STOP
      END
C     ********************************************************
C     * FUNCTION F IS THE GENERAL DISPERSION EQUATION. THE   *
C     * COMPLEX ARGUMENT Z IS DETERMINED FROM X & Y IN THE   *
C     * MAIN PROGRAM.                                        *
C     ********************************************************
      COMPLEX FUNCTION F(Z)
      COMPLEX Z,Z1,ZP1,XO,DO,G,O1,O2,DP,DN,G1
      REAL K
      COMMON K,A,ZI,T,OM,BJ(20)
      Z1=A*Z
      XO=ZI*(1.0+Z*ZP1(Z))/(K*T)
      DO=1.0+(1.0+Z1*ZP1(Z1))/K
      G=CMPLX(0.0,0.0)
      DO 10 I=2,20
      J=I-1
      O1=J*OM+Z1
      O2=-J*OM+Z1
      DP=1.0+(1.0+O1*ZP1(O1))/K
      DN=1.0+(1.0+O2*ZP1(O2))/K
      G1=G+BJ(I)*(1.0/DP+1.0/DN)
      IF(REAL(G1).EQ.0.0.AND.AIMAG(G1).EQ.0.0)GO TO 20
      X1=(REAL(G1)-REAL(G))/REAL(G1)
    1 X2=(AIMAG(G1)-AIMAG(G))/AIMAG(G1)
    2  IF(ABS(X1).GT.0.001.OR.ABS(X2).GT.0.001)GO TO 5
       GO TO 20
    5  G=G1
   10  CONTINUE
   20  F=1.0+X0*(BJ(1)/D0+G1)
       RETURN
       END
C      ****************************************************************
C      * SUBROUTINE BESJ IS REQUIRED IN PROGRAM DISP1 TO DETER-*
C      * MINE THE BESSLE FUNCTION TERMS BJ.                            *
C      ****************************************************************
       SUBROUTINE BESJ(X,N,BJ,IER)
       IER=0
       BJ=0.
       IF(N)10,20,25
   10  IER=1
       RETURN
   20  IF(X)30,21,31
   21  BJ=1
       RETURN
   25  IF(X)30,27,31
   27  BJ=0.
       RETURN
   30  IER=2
       RETURN
   31  IF(X-15.)32,32,34
   32  NTEST=20.+10.*X-X**2/3.
       GO TO 36
   34  NTEST=90.+X/2.
   36  IF(N-NTEST)40,38,38
   38  IER=4
       RETURN
   40  IER=0
       N1=N+1
       BPREV=0.
C
C      COMPUTE STARTING VALUE OF M
C
       IF(X-5.)50,60,60
   50  MA=X+6.
       GO TO 70
   60  MA=1.4*X+60./X
   70  MB=N+IFIX(X)/4+2
       MZERO=MAX0(MA,MB)
C
C      SET UPPER LIMIT OF M
C
       MMAX=NTEST
  100  DO 190 M=MZERO,MMAX,3
C
C      SET F(M),F(M-1)
C
       FM1=1.0E-28
       FM=0.
       ALPHA=0.0
       IF(M-(M/2)*2)120,110,120
  110  JT=-1
       GO TO 130
  120  JT=1
  130  M2=M-2
       DO 160 K=1,M2
       MK=M-K
       BMK=2.*FLOAT(MK)*FM1/X-FM
       FM=FM1
       FM1=BMK
       IF(MK-N-1)150,140,150
  140  BJ=BMK
  150  JT=-JT
       S=1+JT
  160  ALPHA=ALPHA+BMK*S
       BMK=2.*FM1/X-FM
       IF(N)180,170,180
  170 BJ=BMK
  180 ALPHA=ALPHA+BMK
      BJ=BJ/ALPHA
      IF(ABS(BJ-BPREV)-ABS(0.0001*BJ))200,200,190
  190 BPREV=BJ
      IER=3
  200 RETURN
      END
C     *******************************************************
C     * FILAM IS A PROGRAM TO SOLVE DRAKE DISPERSION EQUATION *
C     * FOR BRILOUIN & FILAMENTATION. IT USES TWO EXTERNAL    *
C     * FUNCTIONS ZP1 & F. THE INPUTS TO THIS PROGRAM ARE THE *
C     * SAME AS IN DISP1. THE SAME BISECTION METHOD IS ALSO   *
C     * USED HERE. NO BESSLE FUNCTION IS USED & THE FUNCTION F*
C     * HERE IS NOT THE SAME F BEEN USED IN DISP1 BUT ZP1 IS  *
C     * THE SAME.                                             *
C     *******************************************************
      COMPLEX Z,Z0,Z1,Z2,F,S(200)
      REAL K,N,MI,KD,K0,KN
      DIMENSION Y(200),S1(200),Y1(25),Y2(25),Y3(25),Y4(25),S2(200)
      COMMON K,R,A,Q1,Q2,Q3,Q4,Q5,QP,QM
      READ(5,1)TE,TI,MI,ZI
    1 FORMAT(4F6.2)
      T=TI/TE
      R=ZI/T
      WRITE(3,19)TE,T,MI,ZI
      READ(5,2)K,N,V,CTH
    2 FORMAT(4F6.4)
      A=T/(1836.2*MI)
      A=SQRT(A)
      VT=4.191E7*SQRT(TE)
      VC=3.0E10/VT
      KD=4.256E6*SQRT(N/TE)
      K0=1.0-N
      K0=5.9426E3*SQRT(K0)/KD
      KN=K/(2.0*K0)
      WRITE(3,20)N,CTH,K
      WRITE(3,21)V,VC,KN
      VC=VC*VC
      V=V*V
      Q2=2.0*K*K0*VC*CTH
      Q3=2.82843*K/SQRT(N)
      K=K*K
      R=R/K
      Q1=K*VC
      Q4=0.5*K*V
      Q5=2.0*K
      QP=Q1+Q2
      QM=Q1-Q2
      READ(5,22)N1,N2,DX,DY,DX0,DY0
      DO 16 I=1,N1
      X=DX*I+DX0
      WRITE(3,23)X
      DO 4 J=1,N2
      Y(J)=DY*J+DY0
      Z=CMPLX(X,Y(J))
      S(J)=F(Z)
      S1(J)=REAL(S(J))
    4 S2(J)=AIMAG(S(J))
      IR=0
      II=0
      DO 6 J=2,N2
      F1=S1(J)/S1(J-1)
      IF(F1.GT.0.0)GO TO 5
      IR=IR+1
      Y1(IR)=Y(J-1)
      Y2(IR)=Y(J)
    5 F2=S2(J)/S2(J-1)
      IF(F2.GT.0.0)GO TO 6
      II=II+1
      Y3(II)=Y(J-1)
      Y4(II)=Y(J)
    6 CONTINUE
      IF(IR.EQ.0)GO TO 11
      DO 10 K1=1,IR
      Y11=Y1(K1)
      Y22=Y2(K1)
      Z1=CMPLX(X,Y11)
      Z2=CMPLX(X,Y22)
      F1=REAL(F(Z1))
      F2=REAL(F(Z2))
      DO 8 KO=1,20
      YO=(Y22+Y11)/2.DO
      ZO=CMPLX(X,YO)
      FO=REAL(F(ZO))
      FF=FO/F1
      IF(FF.GT.0.0)GO TO 7
      F2=FO
      Y22=YO
      GO TO 8
    7 F1=FO
      Y11=YO
    8 CONTINUE
      WRITE(3,9)YO,FO
    9 FORMAT(10X,'Y=',E12.5,5X,'RE(D)=',E12.5)
   10 CONTINUE
   11 IF(II.EQ.0)GO TO 16
      DO 15 K1=1,II
      Y33=Y3(K1)
      Y44=Y4(K1)
      Z1=CMPLX(X,Y33)
      Z2=CMPLX(X,Y44)
      F1=AIMAG(F(Z1))
      F2=AIMAG(F(Z2))
      DO 13 KO=1,20
      YO=(Y44+Y33)/2.DO
      ZO=CMPLX(X,YO)
      FO=AIMAG(F(ZO))
      FF=FO/F1
      IF(FF.GT.0.0)GO TO 12
      F2=FO
      Y44=YO
      GO TO 13
   12 F1=FO
      Y33=YO
   13 CONTINUE
      WRITE(3,14)YO,FO
   14 FORMAT(10X,'Y=',E12.5,5X,'IM(D)=',E12.5)
   15 CONTINUE
   16 CONTINUE
   19 FORMAT(5X,'TE=',F6.1,5X,'TI/TE=',F6.3,5X,'MI=',F5.2,5X,
     1'Z=',F5.2)
   20 FORMAT(5X,'N/NC=',F5.3,5X,'COS( )=',F6.2,5X,'K/KD=',F5.3)
   21 FORMAT(5X,'VO/VT=',F5.2,5X,'C/VT=',E12.5,5X,'K/2KO=',E12.5)
   22 FORMAT(2I3,4F6.3)
   23 FORMAT(15X,'***X=',F7.4,'***')
      STOP
      END
      COMPLEX FUNCTION F(Z)
C     *********************************************************
C     * THIS FUNCTION IS REQUIRED BY FILAM PROGRAM TO DETER-  *
C     * MINE THE DRAKE DISPERSION FUNCTION FOR A GIVEN COMPLEX*
C     * VARIABLE Z.                                           *
C     *********************************************************
      COMPLEX Z,Z1,ZP1,XI,XE,ZS,DP,DM
      REAL K
      COMMON K,R,A,Q1,Q2,Q3,Q4,Q5,QP,QM
      Z1=A*Z
      XE=(1.0+Z1*ZP1(Z1))/K
      XI=R*(1.0+Z*ZP1(Z))
      ZS=Z1*Z1*Q5
      DP=QP-Q3*Z1-ZS
      DM=QM+Q3*Z1-ZS
      F=(1.0+XE+XI)*DP*DM-Q4*XE*(1.0+XI)*(Q1-ZS)
      RETURN
      END
C     *********************************************************
C     * THIS FUNCTION IS REQUIRED BY DISP1 & FILAM TO EVALUATE*
C     * THE PLASMA DISPERSION INTEGRAL USING POLYNOMIAL EXPAN-*
C     * SION METHOD.                                          *
C     *********************************************************
      COMPLEX FUNCTION ZP1(Y)
      COMPLEX*16 U,Z,U2,AZP,AZPOLD,USQM,ZP
      COMPLEX Y
      U=Y
      NA=10
      IF(CDABS(U).GE.4.D0)GO TO 3
      USQM=-U**2
      IF(DREAL(USQM).GT.150.D0)USQM=DCMPLX(150.D0,0.D0)
      ZP=DCMPLX(0.D0,1.D0)*1.772453850905516*CDEXP(USQM)
      U2=-2.D0*U**2
      AZP=-2.D0*U
      DO 2 N=1,100
      ZP=ZP+AZP
    2 AZP=AZP*U2/(2.D0*N+1.D0)
      ZP=ZP+AZP
      GO TO 30
    3 Z=1.D0/U
      IF(DIMAG(U).LE.0.D0)GO TO 10
      ZP=0.D0
      GO TO 20
   10 CONTINUE
      USQM=-U**2
      IF(DREAL(USQM).GT.150.D0)USQM=DCMPLX(150.D0,0.D0)
      ZP=DCMPLX(0.D0,1.D0)*1.772453850905516*CDEXP(USQM)
      IF(DIMAG(U).LT.0.D0)ZP=2.D0*ZP
   20 AZP=Z
      U2=0.5D0*Z**2
      DO 25 N=1,NA
      ZP=ZP-AZP
      AZPOLD=AZP
      AZP=(2.D0*N-1.D0)*AZP*U2
      IF(CDABS(AZP).GE.CDABS(AZPOLD))GO TO 30
   25 CONTINUE
      ZP=ZP-AZP
   30 CONTINUE
      ZP1=ZP
      RETURN
      END
```

APPENDIX B

MODELING OF THE CO_2 LASER

B.1 Gas Kinetics of the CO_2-N_2-He Mixture

The physics of the CO_2 laser is well known and can be found in most laser textbooks. Only a simple description is given here. The CO_2 molecule undergoes three vibrational modes. The energy of oscillation of a molecule in any one mode can have only discrete values which are integral multiples of some fundamental value. At any time a carbon dioxide molecule can vibrate in a linear combination of the three modes. The energy state of the molecule can be represented by three energy quantum numbers (ijk). Some of the low-lying vibrational levels of the CO_2 molecule that are responsible for the laser action are shown in Fig. B.1. In the CO_2 laser, molecules are excited from the ground state to higher energy states where they lose their energy and reach a long-lived state (001) by radiative and nonradiative processes. With sufficient pumping, a population inversion is produced between the (001) state and the (100) state. If the losses in the laser cavity surrounding the medium are sufficiently low, laser oscillation begins. To improve the laser output, nitrogen and helium are added to the CO_2 gas. The excited nitrogen molecules transfer energy to the CO_2 molecules by near-resonance collisional transfer, while the helium speeds up the transition from the (100) state to the ground level, thereby maintaining a large population inversion. In

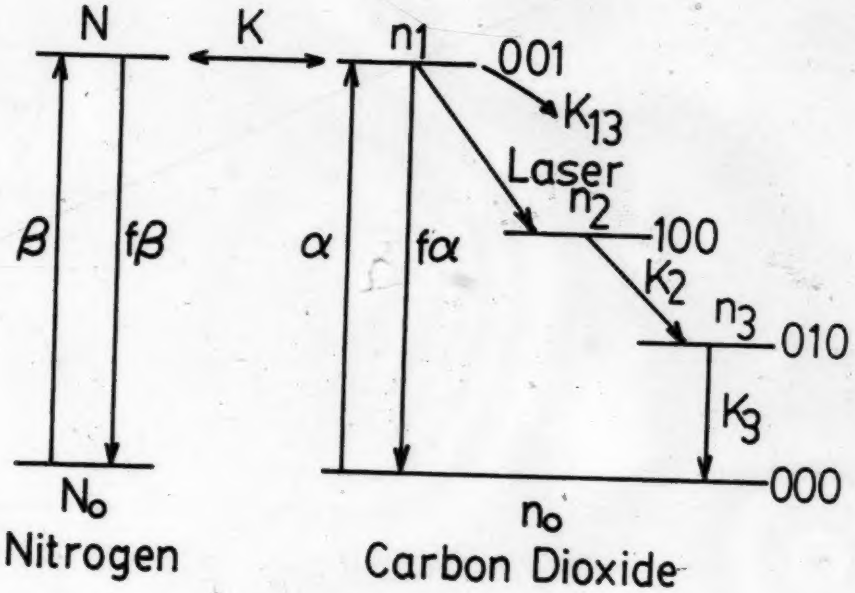
N
K
n1
001
K_{13}
Laser
n_2
100
K_2
n_3
010
K_3
000
β
fβ
α
fα
N_o
Nitrogen
n_o
Carbon Dioxide

Fig. B.1 Some of the low lying levels of the CO_2 and N_2 molecules.

addition, helium helps to eliminate arcs between the electrodes so that efficient pumping can be provided. The output power and energy as well as the time delay between the electrical discharge and the peak of the laser emission depend on gas mixture, mirror reflectivities and pumping level. Several models have been developed by various workers |1-4| to study the effect of the operating conditions on the output pulse characteristics. For the purpose of comparison between theory and experiment, the model described by Andrews *et al.* |3| was found to be simple and adequate. The following set of rate equations was used to describe the CO_2-N_2 energy level scheme adopted by them:

$$\begin{aligned}
\frac{dn_1}{dt} &= \alpha(n_0-fn_1) + k(Nn_0-n_1N_0) - k_{13}n_1 - Sq(n_1-n_2) \ , \\
\frac{dN}{dt} &= \beta(N_0-fN) - k(Nn_0-n_1N_0) \ , \\
\frac{dn_2}{dt} &= Sq(n_1-n_2) - k_2n_2 \ , \\
\frac{dn_3}{dt} &= k_2n_2 - k_3n_3 + k_{13}n_1 \ , \\
\frac{dq}{dt} &= Sq(n_1-n_2) - wq + Dn_1 \ ,
\end{aligned} \tag{B.1}$$

where n_1, N, n_2 and n_3 are the electron population densities of the levels shown in Fig. A.1, k_1 and k_2 are the effective decay rates of the (100) and (010) levels respectively, and α and β are the effective electron excitation rates to the (001) level of the CO_2 molecule and the first excited level of the N_2 molecule respectively. All other transitions of level (001) were assumed to go directly to the (010) level with the k_{13} rate since the intermediate states relax rapidly to the (010) level. The last equation in B.1 describes the growth of photon density q in the laser cavity where w is the cavity decay rate, D defines the rate of spontaneous emission into the cavity mode of interest and Sq is the rate of stimulated emission. For a laser with cavity mirror reflectivities R_1 and R_2, cavity length L, gain length l and gas partial pressures x, y and z for N_2, He and CO_2 respectively, the following parameters are obtained for our laser conditions |3|:

$$w = -c \ln R_1R_2/2L \simeq 7\times10^{7}\,\text{sec}^{-1} ,$$

$$S = cl\sigma/L \simeq 7.5\times10^{-20}\,\text{cm}^{-1}\,\text{sec}^{-1} ,$$

$$k_{13} = (85x + 110y + 265z) \simeq 1.129\times10^{5}\,\text{sec}^{-1} ,$$

$$k_2 \simeq 1.4\times10^{5}(x + 0.46y + 0.056z)\times760 = 3.14\times10^{7}\,\text{sec}^{-1} ,$$

$$k_3 \simeq (4\times10^{3}x + 40y + 200z) = 2.16\times10^{6}\,\text{sec}^{-1} ,$$

$$\alpha \simeq 6\times10^{-9}n_e\ \text{sec}^{-1} ,$$

$$\beta \simeq 2\times10^{-8}n_e\,\text{sec}^{-1} ,$$

$$D \simeq 10^{-10}\,\text{sec}^{-1} ,$$

where $\sigma(= 10^{-19}\,\text{cm}^{-2})$ is the cross section for stimulated emission and n is the time dependent discharge electron density. A good estimate of the electron density, based on the discharge current waveform measurements of Burnett and Offenberger |5|, is given by

$$n(t) \simeq 3\times10^{13}\sin\left(\frac{\pi}{500}\,t\right)\ \text{cm}^{-3} \qquad 0 \le t \le 500\ \text{ns} ,$$

$$n(t) = 0\ \text{otherwise} , \tag{B.2}$$

where t is in ns and the 500 ns shown in Eqn. (B.2) is the current duration. The power is determined from the photon density using the following relation |3|:

$$P_0 \simeq -h\nu q \frac{c \ln R_1}{2L} ,$$

where P_0 is the power per unit mode volume and $h\nu$ is the photon energy of the laser transition.

B.2 Numerical Solution of the Rate Equations

In modeling the TEA CO_2 laser the system of ordinary differential equations (B.1) had to be solved. The classical (fourth order) Runge-Kutta method was applied with a time interval of $\Delta t = 2$ ns. To simplify the method, we assume the N ordinary differential equations of N variables are:

$$\frac{\partial x_i}{\partial t} = f_i(t, x_1, x_2, \ldots, x_N) , \quad i = 1 \text{ to } N .$$

The variable $x_{i,j+1}$ at time $t_j + \Delta t$ is related to $x_{i,j}$ at time t_j by the following equation [6].

$$x_{i,j+1} = x_{i,j} + \frac{1}{6}(k_{i,1} + 2k_{i,2} + 2k_{i,3} + k_{i,4}) ,$$

where

$$k_{i,1} = \Delta t \cdot f_i(t_j, x_{1,j}, x_{2,j}, \ldots, x_{N,j}) ,$$

$$k_{i,2} = \Delta t \cdot f_i(t_j + \Delta t/2, x_{1,j} + \tfrac{1}{2}k_{1,1}, x_{2,j} + \tfrac{1}{2}k_{2,1}, \ldots, x_{N,j} + \tfrac{1}{2}k_{N,1}) ,$$

$$k_{i,3} = \Delta t \cdot f_i(t_j + \Delta t/2, x_{1,j} + \tfrac{1}{2}k_{1,2}, x_{2,j} + \tfrac{1}{2}k_{2,2}, \ldots, x_{N,j} + \tfrac{1}{2}k_{N,2}) ,$$

$$k_{i,4} = \Delta t \cdot f_i(t_j + \Delta t, x_{1,j} + k_{1,3}, x_{2,j} + k_{2,3}, \ldots, x_{N,j} + k_{N,3}) .$$

The results of the above analysis is shown in Fig. 3.2 where the output power is plotted as a function of time. As seen in the figure, lasing starts about 300 ns after the start of the discharge current and the power reaches maximum in less than 20 ns. The laser pulse is seen to consist of a high amplitude gain-switched spike of duration ∿ 50 ns (FWHM), followed by a relatively low amplitude tail extending for about 1 μs.

A program listing the above numerical technique for modeling the CO_2 laser written for the ADAM computer is given below.

```
10   REM   :SET THE INITIAL CONDITIONS
20   D1=6E-09
30   D2=2E-08
40   K=5.4E-13
50   K1=112900
60   K2=31380000
70   K3=2164000
80   S=7.5E-20
90   F=1.157
100  C=3E+10
110  W=69000000
120  D=1E-10
130  M=0
140  M1=0
150  M2=0
160  M3=0
170  Q0=0
180  T=0
190  NC=5.91E+18
200  NN=2.15E+18
210  N=M
220  N1=M1
230  N2=M2
240  N3=M3
250  Q=Q0
260  ND=NC-M1-M2-M3
270  NG=NN-M
280  IF T<500 GOTO 310
290  NE=0
300  GOTO 320
310  NE=3E+13*SIN(6.2832E-03*T)
315  REM   :EVALUATE U1,V1,W1,X1,Y1
320  F1=D1*NE*(ND-F*N1)+K*(N*ND-N1*NG)-K1*N1-S*C*Q*(N1-N2)
330  F2=D2*NE*(NG-F*N)-K*(N*ND-N1*NG)
340  F3=S*C*Q*(N1-N2)-K2*N2
350  F4=K2*N2-K3*N3+K1*N1
360  F5=S*C*Q*(N1-N2)-W*Q+D*N1
370  U1=2E-09*F1
380  V1=2E-09*F2
390  W1=2E-09*F3
400  X1=2E-09*F4
410  Y1=2E-09*F5
420  T=T+1
430  N1=M1+U1/2
440  N=M+V1/2
450  N2=M2+W1/2
460  N3=M3+X1/2
470  Q=Q0+Y1/2
480  IF T<500 GOTO 510
490  NE=0
500  GOTO 520
510  NE=3E+13*SIN(6.2832E-03*T)
520  ND=NC-N1-N2-N3
530  NG=NN-N
535  REM   :EVALUATE U2,V2,W2,X2,Y2
540  F1=D1*NE*(ND-F*N1)+K*(N*ND-N1*NG)-K1*N1-S*C*Q*(N1-N2)
550  F2=D2*NE*(NG-F*N)-K*(N*ND-N1*NG)
560  F3=S*C*Q*(N1-N2)-K2*N2
570  F4=K2*N2-K3*N3+K1*N1
580  F5=S*C*Q*(N1-N2)-W*Q+D*N1
590  U2=2E-09*F1
600  V2=2E-09*F2
610  W2=2E-09*F3
620  X2=2E-09*F4
630  Y2=2E-09*F5
640  N1=M1+U2/2
650  N=M+V2/2
660  N2=M2+W2/2
670  N3=M3+X2/2
680  Q=Q0+Y2/2
```

```
690  NO=NC-N1-N2-N3
700  NG=NN-N
710  REM  :T=T+1 NANOSECOND WILL BE USED LATER
720  T=T+1
730  REM  :EVALUATE U3.V3.W3.X3.Y3
740  F1=D1*NE*(NO-F*N1)+K*(N*NO-N1*NG)-K1*N1-S*C*Q*(M1-N2)
750  F2=D2*NE*(NG-F*N)-K*(N*NO-N1*NG)
760  F3=S*C*Q*(N1-N2)-K2*N2
770  F4=K2*N2-K3*N3+K1*N1
780  F5=S*C*Q*(N1-N2)-W*Q+D*N1
790  U3=2E-09*F1
800  V3=2E-09*F2
810  W3=2E-09*F3
820  X3=2E-09*F4
830  Y3=2E-09*F5
840  N1=M1+U3
850  N=M+V3
860  N2=M2+W3
870  N3=M3+X3
880  Q=Q0+Y3
890  IF T<500 GOTO 920
900  NE=0
910  GOTO 930
920  NE=3E+13*SIN(6.2832E-03*T)
930  NO=NC-N1-N1-N3
940  NG=NN-N
950  REM  :EVALUATE U4.V4.W4.X4.Y4
960  F1=D1*NE*(NO-F*N1)+K*(N*NO-N1*NG)-K1*N1-S*C*Q*(N1-N2)
970  F2=D2*NE*(NG-F*N)-K*(N*NO-N1*NG)
980  F3=S*C*Q*(N1-N2)-K2*N2
990  F4=K2*N2-K3*N3+K1*N1
1000 F5=S*C*Q*(N1-N2)-W*Q+D*N1
1010 U4=2E-09*F1
1020 V4=2E-09*F2
1030 W4=2E-09*F3
1040 X4=2E-09*F4
1050 Y4=2E-09*F5
1060 REM  :CALCULATE THE VARIABLE AT T=T+2.0
1070 M1=M1+(U1+2*U2+2*U3+U4)/6
1080 M=M+(V1+2*V2+2*V3+V4)/6
1090 M2=M2+(W1+2*W2+2*W3+W4)/6
1100 M3=M3+(X1+2*X2+2*X3+X4)/6
1110 Q0=Q0+(Y1+2*Y2+2*Y3+Y4)/6
1120 REM  :CALCULATE THE POWER
1130 P=1.3186E-12*Q0
1140 PRINT T,P
1150 IF T<1000 GOTO 210
1160 END
```

APPENDIX C

ABEL INVERSION

In cylindrically symmetric plasma one can determine the plasma density from the phase shift measured by an interferometer. Figure C.1 represents a cross sectional view of the plasma. The plasma density is assumed to be symmetric in any azimuthally symmetric circle of radius r. The change in fringes that an observer sees due to the variation in density along the path AA' is given by Eqn. (3.7)

$$N = 2G\int_0^{y_0} n(r)dy \ , \qquad (C.1)$$

where $G = \frac{e^2\lambda_0}{mc^2}$. Equation (C.1) can be written in a more convenient form after making the substitution, $y = (r^2 - x^2)^{\frac{1}{2}}$

$$N(x) = 2G\int_x^R \frac{n(r)rdr}{(r^2 - x^2)^{\frac{1}{2}}} \ . \qquad (C.2)$$

Abel inversion of Eqn. (C.2) yields

$$n(r) = -\frac{1}{\pi G}\int_r^R \frac{N'(x)dx}{(x^2 - r^2)^{\frac{1}{2}}} \ , \qquad (C.3)$$

where $N'(x)$ is the first derivative of $N(x)$ with respect to x.

Several numerical methods have been used to solve the integral in Eqn. (C.3). A summary of these methods is given in reference |1|. The method of Nestor and Olsen |2| was found to be simple and adequate. This method is based on linear expansion of the integral in (C.3) by assuming equal intervals along x and R. Accordingly, the plasma density

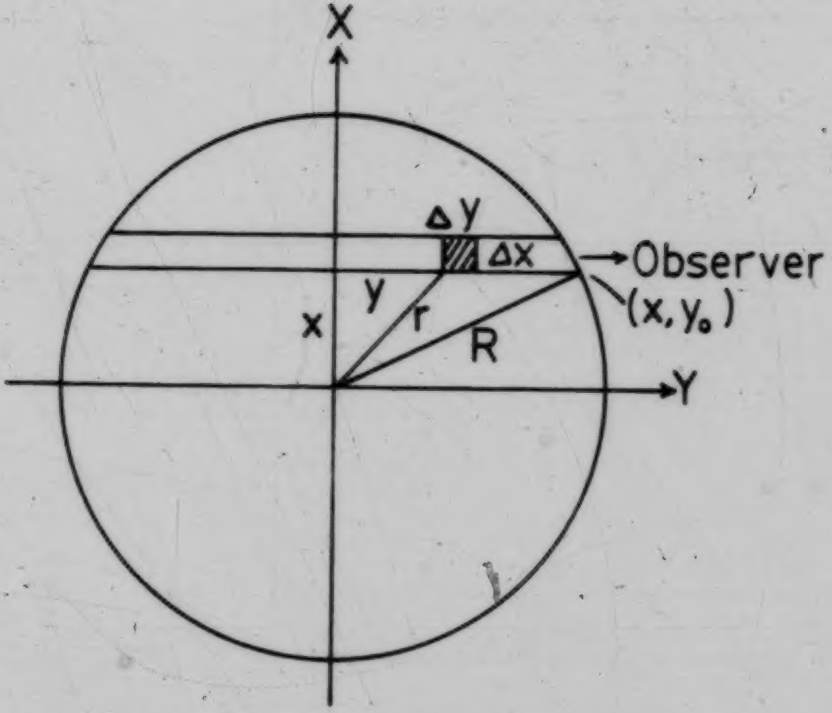
X
Δy
Δx
Observer
(x, y₀)
y
x
r
R
Y

Fig. C.1 Cross sectional view of a cylindrically symmetric plasma.

at a radius of $(k-1)\,x$ is

$$n_k(r) = -\frac{2}{\pi G \Delta x} \sum_{n=k}^{N_0} N_n(x) B_{k,n}\,, \qquad \text{(C.4)}$$

where

$$B_{k,n} = -A_{k,k} \quad \text{for } n = k$$

$$B_{k,n} = A_{k,n-1} - A_{k,n} \quad \text{for } n \geq k_{+1}$$

$$A_{k,n} = \frac{|n^2-(k-1)^2|^{\frac{1}{2}} - |(n-1)^2-(k-1)^2|^{\frac{1}{2}}}{2n-1}\,.$$

Here k and n represent the respective radial and lateral points under consideration, Δx is the interval width, and N_0 is the number of points used.

A computer program was written for the HP-85 computer to do Abel inversion. The program digitizes the fringe pattern from an enlarged photograph, calculates the density $n(r)$ and plots it as a function of r. A list of the program is given below.

```
10   PLOTTER IS 705
20   OPTION BASE 1
30   DIM A(6),B(6),X(100),Y(100)
40   DIM F(100)
50   DISP "CALCULATE THE BASE LINE"
60   DISP "DIGITIZE 3 POINTS EACH SIDE OF THE LINE"
70   BEEP
80   FOR I=1 TO 6
90   DIGITIZE B(I),A(I)
100  NEXT I
110  DISP "GIVE THE RESOLUTION IN MICRON/FRINGE"
120  BEEP
130  INPUT R
140  C1=C2=C3=C4=0
150  FOR I=1 TO 6
160  C1=C1+B(I)*A(I)
170  C2=C2+A(I)
180  C3=C3+B(I)
190  C4=C4+A(I)*A(I)
200  NEXT I
210  A2=(6*C1-C2*C3)/(6*C4-C2*C2)
220  A1=(C3-A2*C2)/6
230  DISP "DETERMINE THE CENTRE OF THE PROFILE"
240  BEEP
250  DISP "DIGITIZE TWO POINTS AT THE EDGES OF THE
     PROFILE STARTING FROM THE BOTTOM"
260  DIGITIZE X1,Y1
270  DIGITIZE X2,Y2
280  YO=(Y1+Y2)/2
290  D=(Y2-Y1)/2
300  XO=(X2+X1)/2
310  MOVE XO,YO
320  DISP "SPECIFY THE # OF DATA INPUT"
330  BEEP
340  INPUT N
350  DISP "WRITE 1 FOR MOVING UP OR 2 FOR MOVING DOWN"
360  BEEP
370  INPUT L
380  IF L=1 THEN 410
390  D=-D/(N-1)
400  GOTO 420
410  D=D/(N-1)
420  X(1)=XO
430  BEEP
440  DISP "START DIGITIZING"
450  FOR I=1 TO N
460  Y(I)=YO+(I-1)*D
470  MOVE X(I),Y(I)
480  DIGITIZE X(I),Y(I)
490  X(I+1)=X(I)
500  NEXT I
510  DISP "CALCULATE THE DATA IN UNITS OF FRINGE SHIFT"
520  DISP "DIGITIZE TWO POINTS ON TWO STRAIGHT LINES"
530  BEEP
540  DIGITIZE X1,Y1
550  DIGITIZE X2,Y2
560  DISP "WRITE # OF FRINGES BETWEEN THESE LINES"
570  INPUT M
580  Z=ABS(X2-X1)/M
590  FOR I=1 TO N
600  X(I)=(X(I)-A1-A2*Y(I))/Z
610  Y(I)=ABS(Y(I)-YO)*R/Z
620  Y(I)=ABS(Y(I))
630  DISP X(I),Y(I)
640  NEXT I
650  D=0.0001*ABS(D)*R/Z
660  FOR I=K TO N-1
670  F(K)=0
680  FOR M=K TO N-1
690  X1=(K-1)*(K-1)
700  X2=(M-1)*(M-1)
710  X3=(M-2)*(M-2)
```

```
720  IF M=K THEN 770
730  A1=(SQR(M*M-X1)-SQR(X2-X1))/(2*M-1)
740  A2=(SQR(X2-X1)-SQR(X3-X1))/(2*M-1)
750  B=A2-A1
760  GOTO 780
770  B=-1/SQR(2*K-1)
780  F(K)=F(K)+X(M)*B
790  NEXT M
800  F(K)=F(K)*2.0479E17/D
810  PRINT Y(K),F(K)
820  NEXT K
830  FOR I=1 TO N-1
840  F(I)=F(I)/1.E18
850  Y(I)=Y(I)/100
860  NEXT I
870  Y7=CEIL(Y(N-1))
880  Y6=Y7/8
890  PLOTTER IS 1
900  PEN 1 @ GCLEAR
910  SCALE -Y6,Y7,0,10
920  XAXIS 1,1,0,Y7
930  YAXIS 0,1,1,10
940  LDIR 0
950  FOR X7=0 TO 10
960  MOVE X7,0
970  LABEL VAL$(X7)
980  NEXT X7
990  FOR Y5=1 TO 10
1000 MOVE -Y6,Y5
1010 LABEL VAL$(Y5)
1020 NEXT Y5
1030 PENUP
1040 FOR I=1 TO N-1
1050 PLOT Y(I),F(I)
1060 NEXT I
1070 END
```

APPENDIX D

NUMERICAL SOLUTION OF THE $S(\omega,\overline{k})$ FUNCTION

The numerical solution of the $S(\omega,\overline{k})$ function as defined in Eqns. (3.20) and (3.21), including the complex functions $G_e(\omega)$ and $G_i(\omega)$, is straight forward except for the integral part in the definition of the function f. To solve this part, the function f may be rewritten in the following form

$$f(x) = 2x \int_0^x \exp(t^2 - x^2)dt \ , \qquad (D.1)$$

where the variable x was moved inside the integral. The $\exp(t^2 - x^2)$ function is only significant when t is close to x. Therefore, the integral in (D.1) is evaluated for the interval

$$t = 0 \text{ to } x \ , \qquad \text{when } |x| < 5$$

and

$$t = (x^2 - 4^2)^{\frac{1}{2}} \text{ to } x, \qquad \text{when } |x| \geq 5 \ .$$

The above range of t is then divided into 100 intervals where Simpson's rule is applied to evaluate the integral. The above method is proved to be fast and fairly accurate.

Below is listed a Fortran IV program for the **AMDAHL 470 computer.** The inputs for this program are T_e and T_i in eV, M_e (required to calculate λ_D), the scattering angle, the ion mass number, the spectrum range in Å and the step in Å at which $S(\omega,\overline{k})$ is to be calculated.

```
C       ************************************************************
C       * PROGRAM SCATT CALCULATES THOMSON SCATTERING SPECTRUM,     *
C       * S(K,W) FOR A GIVEN TEMPERATURES (TE & TI IN eV),          *
C       * PLASMA DENSITY (N IN CM-3), ANGLE (THETA IN DEGREES),     *
C       * ION MASS (A IN ATOMIC UNITS) AND IONIZATION DEGREE (Z)*
C       * IN A WAVELENGTH RANGE (RANGE IN ANGSTROMS) WITH A STEP*
C       * D IN ANGSTROMS).                                          *
C       ************************************************************
        REAL N,K
        COMPLEX GE,GI,GEE,GII,E
        READ(5,1)TE,TI,N,THETA,A,RANGE,D,Z
   1    FORMAT(2F5.1,E7.2,5F7.2)
        TR=TE/TI
        K=1.8099E5*SIN(0.00873*THETA)
        ALPHA=SQRT(N/TE)/(743.4*K)
        WRITE(6,5)
   5    FORMAT('1')
C       WRITING THE PLASMA & SCATTERING PARAMETERS
        WRITE(6,10)TE,TI,A,Z,N
  10    FORMAT(1X,'TE=',F6.1,5X,'TI=',F6.1,5X,'A=',F5.1,5X,'Z=',F4.1,5X,
       1'N=',E7.2)
        WRITE(6,16)TR,THETA,ALPHA
  16    FORMAT(1X,'RATIO=',F5.2,5X,'ANGLE=',F5.1,5X,'ALPHA=',E7.2)
        WRITE(6,17)
        WRITE(6,20)
  17    FORMAT(////)
  20    FORMAT(' WLENGTH',5X,'ION COMP',9X,'ELECTRON COMP',4X,'S(W,K)')
        WRITE(6,21)
  21    FORMAT(1X,'-------     ------------     ------------
       1'------------')
C       CALCULATE THE COMPLEX FUNCTIONS GE & GI
        R=A/TI
        A1=9.5126E-9/SQRT(TE)
        A2=-2.8428E-16/TE
        B1=4.076E-7*SQRT(R)
        B2=-5.2197E-13*R
        WE=5.931E7*K*SQRT(TE)
        WI=1.384E6*K/SQRT(R)
        ALP=ALPHA*ALPHA
        D1=-RANGE
  25    D1=D1+D
        IF(D1.GT.0.0)GO TO 150
        W=3.9103E11*ABS(D1)
        VE=(W/K)**2
        X=W/WE
        Y=W/WI
        GI1=1-F(Y)
        GE1=1-F(X)
        X2=X*X
        Y2=Y*Y
        IF(Y2.GT.30.0)GO TO 30
        GI2=1.7725*Y*EXP(-Y2)
        GO TO 40
  30    GI2=0.0
  40    IF(X2.GT.30.0)GO TO 50
        GE2=1.7725*X*EXP(-X2)
        GO TO 60
  50    GE2=0.0
  60    GE=CMPLX(GE1,GE2)
        GI=CMPLX(GI1,GI2)

        GE=-ALP*GE
        GI=-Z*TR*ALP*GI
        E=1-GI-GE
        GEE=(1-GI)/E
        GII=GE/E
        C1=VE*A2
        IF(C1.LT.-50.0)GO TO 70
        FE=A1*EXP(C1)*CABS(GEE)**2
        GO TO 80
  70    FE=0.0
  80    C2=VE*B2
```

```
        IF(C2.LT.-50.0)GO TO 90
        FI=Z*B1*EXP(C2)*CABS(GII)**2
        GO TO 95
  90    FI=0.0
  95    FEI=FE+FI
        WRITE(6,100)D1,FI,FE,FEI
  100   FORMAT(1X,F7.2,5X,3(E12.5,5X))
        GO TO 25
  150   STOP
        END
  C     ************************************************************
  C     * FUNCTION F IS USED TO EVALUATE THE INTEGRAL PART IN      *
  C     * S(K,W) USING THE METHOD DESCRIBED IN THIS APPENDIX.      *
  C     ************************************************************
        FUNCTION F(X)
        REAL*8 S(101),Y,Y1,T,T1,D,F1,F2,FN
        IF(X.EQ.0.0)GO TO 100
        Y=DBLE(X)
        Y1=Y*Y
        T=0.0
        F1=0.0
        F2=0.0
        IF(Y.LT.5.0)GO TO 10
        T=DSQRT(Y1-16.0)
  10    D=(Y-T)/100.0
        DO 20 I=1,101
        T1=T+(I-1)*D
  20    S(I)=DEXP(T1*T1-Y1)
        DO 50 I=2,100,2
  50    F1=F1+S(I)
        DO 60 I=3,100,2
  60    F2=F2+S(I)
        FN=2.0*(4.0*F1+2.0*F2+S(1)+S(101))*D*Y/3.0
        F=SNGL(FN)
        GO TO 200
  100   F=0.0
  200   RETURN
        END
End of file
```

2

APPENDIX E

DECONVOLUTION OF SPECTRA

Accurate measurement of the scattered spectrum is possible only if the spectral bandwidth of the instrument is negligible in comparison with the halfwidth of the spectral shape. If the spectral width and the instrumental width are of comparable magnitude, the recorded distribution $A(\lambda)$ will be a complicated function of the true spectrum $B(\lambda)$ and the instrumental function $S(\lambda)$. Mathematically the relation can be expressed by the convolution integral

$$A(\lambda) = \int_{-\infty}^{\infty} S(\lambda-\lambda')B(\lambda')d\lambda' \ . \tag{E.1}$$

In measuring the ion feature of the scattered spectra the width of the ion feature is so often small that the effect of the spectrometer slit cannot be ignored. To recover the true spectral shape $B(\lambda)$ from the recorded one, a deconvolution routine similar to the one suggested by Jones *et al.* |1| was used. This method may be explained by first writing Eqn. (E.1) in a more convenient form

$$A_i = \sum_{j=1}^{N} S_{ij}B_j \ , \quad i = 1 \text{ to } N \ , \tag{E.2}$$

or in a matrix form

$$A = SB \ , \tag{E.3}$$

where N is the number of data input. The technique used by Jones *et al.* |1| is to recover B from A and S using the following iterative method

$$\left.\begin{aligned} B^n &= SA^n \\ A_i^{n+1} &= (A_i^1/B_i^n)\cdot A_i^n \\ \delta^n &= \frac{1}{N}\sum_{j=1}^{N}(A_j^{n+1} - A_j^n) \end{aligned}\right\} , \tag{E.4}$$

where the iterations can cease when δ^n converges to within a certain limit. The elements of the slit matrix were taken to be cyclic of the form |2|

$$S = \begin{pmatrix} s_1 s_2 & \cdots & s_N \\ s_2 s_3 & & s_N s_1 \\ \cdot & & \\ \cdot & & \\ \cdot & & \\ s_N s_1 & & s_{n-1} \end{pmatrix} , \tag{E.5}$$

with rows normalized to unity,

$$\sum_{j=1}^{N} S_{ij} = 1 . \tag{E.6}$$

For our application, each row was taken as a truncated normalized Gaussian function; its center was taken at $(N+1)/2$ (where N is an odd number) and its FWHM was made equivalent to the FWHM of a monochromatic line seen by the spectrometer (usually the He-Ne laser). A five point smoothing routine

$$A_i' = |17A_i + 12(A_{i-1} + A_{i+1}) - 3(A_{i-2} + A_{i+2})|/35 \tag{E.7}$$

was used to smooth the experimental data A and the calculated date A^n after each iteration.

A FORTRAN program was written for the **AMDAHL 470** capable of handling up to 50 equally spaced data points. The program plots the deconvoluted data on the printer and convolutes the result to check the recovery of the original data. Usually three to four iterations are required to deconvolute the matrix *A* of 100-200 points. Figure E.1 shows a convoluted spectrum (a) constructed from a true spectrum, (b) and a truncated Gaussian slit function of FWHM = 13 using Eqns. (E.3) and (E.5). The deconvoluted spectrum of Fig. E(a) is shown in Fig. E(c) after three iterations. A listing of the computer program is given below.

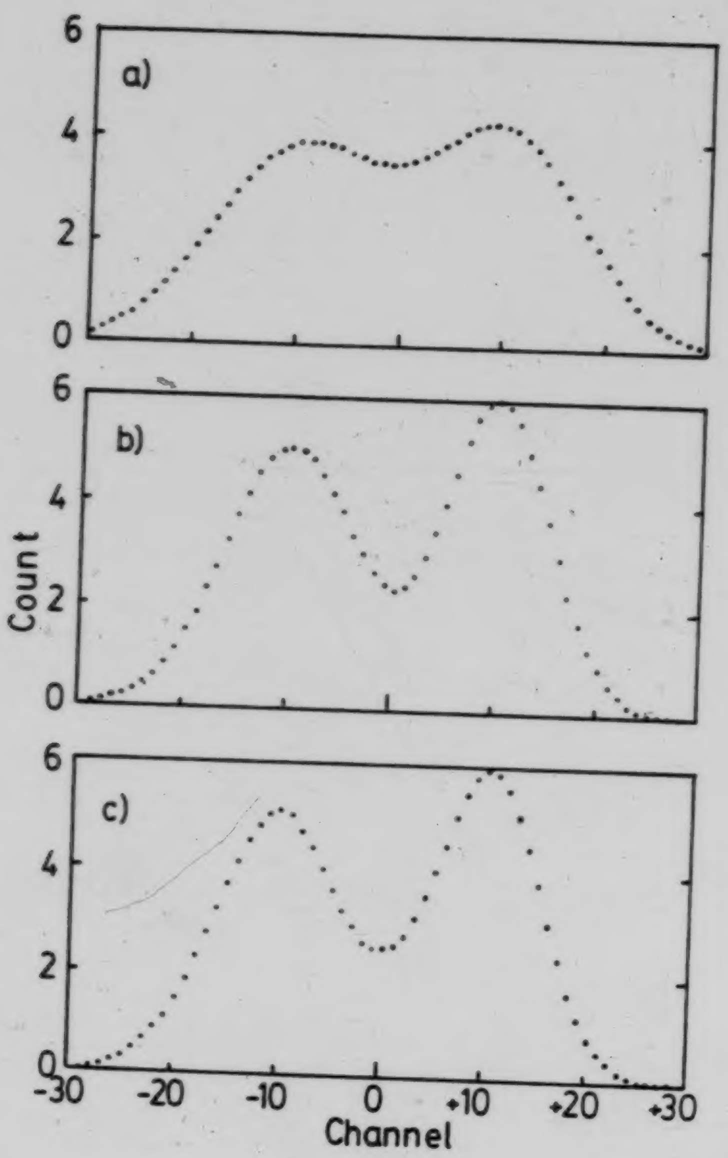

Fig. E.1 Effect of a finite slit on a spectrum.
a) The spectrum as observed through a Gaussian slit of FWHM = 13 channels. b) The true spectrum. c) The recovery of the true spectrum from the observed one using the deconvolution technique.

```
C     ***************************************************************
C     * PROGRAM DEC FOR DECONVOLVING EXPERIMENTAL DATA USING         *
C     * TRUNCATED GAUSSIAN SLIT FUNCTION AND PLOTING THE             *
C     * RESULTS ON THE PRINTER. THE INPUTS TO THIS PROGRAM ARE*
C     * FW, THE FWHM OF THE SLIT FUNCTION IN CHANNELS; N, THE *
C     * NO. OF DATA TO BE DECONVOLVED; A(N), THE MEASURED            *
C     * DATA.                                                        *
C     ***************************************************************
      DIMENSION A(500),B(500),C(500),S(500),A1(500),DELTA(16)
      DIMENSION AA(80),LL(500)
      DATA X1,X2/' ','*'/
      READ(5,1)FW,N
    1 FORMAT(F4.1,I3)
C     DETERMINING THE SLIT FUNCTION.
      S(1)=0.93944/FW
      DO 5 I=2,N
      X=I-1
      Y=2.7726*(X/FW)**2
      IF(Y.GT.100.0)GO TO 2
      S(I)=S(1)*EXP(-Y)
      GO TO 5
    2 S(I)=0.0
    5 CONTINUE
      READ(2,10)(A(I),I=1,N)
   10 FORMAT(10F5.2)
      WRITE(6,20)(A(I),I=1,N)
   20 FORMAT(5(1X,E10.3))
      DO 25 I=1,16
   25 DELTA(I)=0.0
C     ITERATIONS START TO CALCULATE THE DECONVOLUTION MATRIX
      IT=1
      CALL SMOOTH(N,A)
      WRITE(6,20)(A(I),I=1,N)
      CALL MATM(N,A,B,S)
      CALL RATIO(N,A,B,C,A)
      CALL SMOOTH(N,C)
      DO 30 I=1,N
      DELTA(IT)=DELTA(IT)+C(I)-A(I)
   30 A1(I)=C(I)
      DELTA(IT)=DELTA(IT)/N
   35 CALL MATM(N,A1,B,S)
      CALL RATIO(N,A1,B,C,A)
      DO 40 I=1,N
   40 DELTA(IT+1)=DELTA(IT+1)+C(I)-A1(I)
      DELTA(IT+1)=DELTA(IT+1)/N
      WRITE(6,42)DELTA(IT)
   42 FORMAT(5X,E12.5)
      DEL=(DELTA(IT+1)-DELTA(IT))/DELTA(IT)
      IF(ABS(DEL).LT.0.05)GO TO 60
      IF(IT.EQ.15)GO TO 50
      IT=IT+1
      CALL SMOOTH(N,C)
      DO 45 I=1,N
   45 A1(I)=C(I)
      GO TO 35
   50 WRITE(6,55)
   55 FORMAT(10X,'***CONVERGENCE COULD NOT BE REACHED***')
   60 WRITE(6,65)IT
   65 FORMAT(15X,'IT=',I2)
      WRITE(6,20)(C(I),I=1,N)
      CALL MATM(N,C,B,S)
      WRITE(6,20)(B(I),I=1,N)
      XX=C(1)
      DO 70 I=2,N
      IF(C(I).GT.XX)XX=C(I)
   70 CONTINUE
      DO 75 I=1,N
      LL(I)=80.0*C(I)/XX
   75 CONTINUE
      DO 100 I=1,N
      DO 85 J=1,80
      IF(J.EQ.LL(I))GO TO 80
      AA(J)=X1
      GO TO 85
   80 AA(J)=X2
   85 CONTINUE
      WRITE(6,90)I,(AA(K1),K1=1,80)
   90  FORMAT(1X,I3,'I',80A1)
  100 CONTINUE
      STOP
      END
C     *********************************************************
C     * SUBROUTINE SMOOTH IS USED TO SMOOTH THE INPUT DATA AND*
C     * THE DECONVOLVED DATA AFTER EACH ITERATION AS WELL.    *
C     * USING FIVE-POINT SMOOTHING TECHNIQUE.                 *
C     *********************************************************
      SUBROUTINE SMOOTH(N,A)
      DIMENSION A(500),F(500)
      M=N-2
      DO 5 I=3,M
      F(I)=(17.*A(I)+12.*(A(I-1)+A(I+1))-3.*(A(I-2)+A(I+2)))/35.0
    5 CONTINUE
      DO 10 I=3,M
   10 A(I)=F(I)
      A(1)=(17.*A(1)+12.*A(2)-3.*A(3))/35.0
      A(2)=(17.*A(2)+12.*(A(1)+A(3))-3.*A(4))/35.0
      A(N-1)=(17.*A(N-1)+12.*(A(N-2)+A(N))-3.*A(N-3))/35.0
      A(N)=(17.*A(N)+12.*A(N-1)-3.*A(N-2))/35.0
      RETURN
      END
C     *********************************************************
C     *SUBROUTINE MATH PERFORMS THE MULTIPLICATION OF THE SLIT*
C     *MATRIX AND THE DATA MATRIX.                            *
C     *********************************************************
      SUBROUTINE MATM(N,A,B,S)
      DIMENSION A(500),B(500),S(500)
      DO 10 I=1,N
      B(I)=0.0
      DO 5 J=1,I
      B(I)=B(I)+S(I-J+1)*A(J)
    5 CONTINUE
      IF(I.EQ.N)GO TO 10
      J2=N-I+1
      DO 10 J=2,J2
      B(I)=B(I)+S(J)*A(J+I-1)
   10 CONTINUE
      RETURN
      END
C     *********************************************************
C     * SUBROUTINE RATIO CALCULATES THE NEW DECONVOLVED       *
C     * MATRIX C FROM A AND B.                                *
C     *********************************************************
      SUBROUTINE RATIO(N,A1,B,C,A)
      DIMENSION A1(500),B(500),C(500),A(500)
      DO 10 I=1,N
      IF(B(I).EQ.0.0)GO TO 5
      C(I)=A1(I)*A(I)/B(I)
      GO TO 10
    5 C(I)=0.0
   10 CONTINUE
      RETURN
      END
```